A COMPUTATIONAL FLUID DYNAMICS MODEL FOR CLOSED-FRACTURE ACIDIZING USING THE TWO-SCALE CONTINUUM APPROACH

A Thesis

by

KHALED N SH A ALDHAYEE

Submitted to the Office of Graduate and Professional Studies of
Texas A&M University
in partial fulfillment of the requirements for the degree of

MASTER OF SCIENCE

Chair of Committee,	Hisham Nasr-El-Din
Committee Members,	Jerome Schubert
	Mahmoud El-Halwagi
Head of Department,	Jeff Spath

August 2019

Major Subject: Petroleum Engineering

ABSTRACT

Closed-fracture acidizing (CFA) is a well stimulation technique that can be applied to stimulate carbonate reservoirs at the end of acid fracturing treatment to enhance the connectivity between the acid-fracture and the wellbore. In CFA, acid is injected in the closed-fracture at rates lower than the fracturing pressure to dissolve the minerals that exist in the fracture; hence, it enhances the fracture conductivity. Etching of fracture surfaces and propagation of wormholes from the fracture are often associated with CFA operations. The objective of this study is to develop a robust model that can capture the dissolution process and wormholing phenomenon that occur during CFA.

In this work, CFA model is developed using computational fluid dynamics (CFD) techniques coupled with the two-scale continuum model that can predict accurately the reactive flow mechanisms of hydrochloric acid (HCl) in carbonate formations. Multiple CFA models are constructed and populated with the actual porosity distribution profiles of calcite and dolomite formations. Then, the developed model is validated using the results of the experimental work done on the API fracture-conductivity apparatus. Sensitive analysis is carried out for several parameters that affect the performance of CFA in carbonate formations.

Two-scale continuum model has successfully captured the dissolution patterns and wormholing phenomenon that occur in the CFA through the model validation study. Several parameters have been investigated to study their effects on CFA operation in calcite and dolomite formations. Acid injection rate and concentration contribute significantly to the performance of CFA in calcite formation that exhibits the diffusion-controlled reaction regime. On the other hand, high acid concentration needs to be injected in dolomite formation for an efficient stimulation job. Well geometry, formation permeability, and fracture conductivity have great effects in controlling the acid flow in the medium and the acid leakoff process that induces wormholes in the domain.

The developed CFD model was able to predict the performance of CFA in carbonate formations that exhibit degrees of heterogeneities and natural fractures. The model was upscaled to establish a qualitative relationship that can relate the acid volumes of CFA used in the model and in an actual acid-fractured well.

DEDICATION

This work is dedicated to my mother, brothers, friends and all those who continuously support me throughout my life.

ACKNOWLEDGEMENTS

I am most thankful to my advisor, Professor Hisham Nasr-El-Din for his continuous and permanent support and guidance. He provided me with the unconditional knowledge and encouragement to pursue the topics which I am most passionate about. He inspired me as a father and as a mentor that I wish to live up to one day. I am also grateful to Professor Jerome Schubert and Professor Mahmoud EL-Halwagy for their continuous support and for serving as committee members.

I would like to extend my appreciation to my friends and colleagues in the group. I am grateful to all the time spent with them and all the fruitful discussions we had. A special thanks to Dr. Mahmoud Ali for his unlimited guidance and mentoring on the fundamentals of modeling. He assisted me in tackling the issues that were encountered during this study.

Finally, I would like to thank Kuwait University and Petroleum Engineering Department for providing me the scholarship and sponsorship to pursue higher graduate studies in Texas A&M University.

CONTRIBUTORS AND FUNDING SOURCES

This work was supervised by a thesis committee consisting of Professor Hisham Nasr-El-Din who served as committee chair, Professor Jerome Schubert of the Department of Petroleum Engineering, and Professor Mahmoud El-Halwagy of the Department of Chemical Engineering.

Texas A&M University High Performance Research Computing Facility contributed for their assistance in facilitating the simulations conducted in this study. I am fully sponsored by Kuwait University.

NOMENCLATURE

$[Ca^{2+}]$	Calcium concentration, n/L^3, mol/L
$[H^+]$	Hydrogen concentration, n/L^3, mol/L
$[Mg^{2+}]$	Magnesium concentration, n/L^3, mol/L
a	Parameter in Freundlich isotherm, 1/T, K^{-1}
a_v	Interfacial area available for reaction per unit volume of the medium, 1/L, m^{-1}
a_{vo}	Initial interfacial area per unit volume of medium, 1/L, m^{-1}
C_0	Acid concentration at wormhole entrance, n/L^3, mol/L
$CaCl_{2(aq)}$	Calcium chloride in aqueous-phase
$CaCO_{3(s)}$	Calcium carbonate in solid-phase (Calcite)
$CaMg(CO_3)_{2(s)}$	Calcium-Magnesium carbonate in solid-phase (Dolomite)
C_f	Original acid concentration in fluid phase, n/L^3, mol/L
CFA	Closed-Fracture Acidizing
CFD	Computational Fluid Dynamics
CO_2	Carbon dioxide
C_s	Acid concentration at fluid-solid interface, n/L^3, mol/L
$\mathbf{D_e}$	Effective dispersion tensor, L^2/t, m^2/s
$\mathbf{D_eT}$	Transverse dispersion coefficient in the y- and z- directions, L^2/t, m^2/s
$\mathbf{D_eX}$	Longitudinal dispersion coefficient, L^2/t, m^2/s
D_m	Acid diffusivity, L^2/t, m^2/s

DREC	Dissolved rock equivalent conductivity, L^3, m^3
E	Activation energy, mL^2/nt^2, J/mol
F_c	Fracture conductivity, L^3, m^3
GPM	Gallons per minute
$H_2O_{(l)}$	Water phase
HCl	Hydrochloric Acid
HPD	High-Permeability Dolomite
$\mathbf{K}$	Permeability tensor, L^2, m^2
k_c	Local mass transfer coefficient, L/t, m/s
k_f	Fracture permeability, L^2, m^2
$\mathbf{K_o}$	Initial permeability tensor, L^2, m^2
k_s	Dissolution rate constant, L/t, m/s
k_{so}	Frequency factor, L/t, m/s
LPD	Low-Permeability Dolomite
$MgCl_{2(aq)}$	Magnesium chloride in aqueous-phase
n	Reaction exponent
N_{Da}	Damköhler Number, Dimensionless
N_{ki}	Kinetic Number, Dimensionless
N_{Pe}	Peclet Number, Dimensionless
p	pressure, $mL^{-1}t^{-2}$, Pa
PVBT	Pore volumes to breakthrough
R	Ideal gas constant, mL^2/nTt^2, J/mol/K

$R(C_s)$	Reaction rate of acid-matrix, $n/t/L^2$, $mol/s/m^2$
Re_p	Pore scale Reynold's number, dimensionless
RES	Rock embedment strength, $mL^{-1}t^{-2}$, Pa
r_p	Pore radius, L, m
r_{po}	Initial pore radius, L, m
r_w	Wormhole radius, L, m
Sc	Schmidt number, dimensionless
Sh	Sherwood number, dimensionless
Sh_∞	Asymptotic Sherwood number, dimensionless
T	Absolute temperature, T, K
$\mathbf{u}$	Superficial velocity vector, L/t, m/s
v_L	acid leakoff velocity, L/t, m/s
w_f	Fracture width, L, m
X_m	Parameter in the Freundlich isotherm, mL^2/nt^2, J/mol
α	Acid dissolving power, m/n, g/mol
α_{os}	Constant that depends on structure of porous medium (pore connectivity)
β	Pore expansion parameter
γ	Pore-connectivity parameter
ε	Porosity of the medium
λ_T	Constant in the transverse dispersion correlation
λ_X	Constant in the axial dispersion correlation
μ	Fluid viscosity, m/Lt, mPa.s

ρ	Fluid density, m/L^3, kg/m^3
ρ_s	Rock matrix density, m/L^3, kg/m^3
σ_c	Formation closure stress, $mL^{-1}t^{-2}$, Pa

TABLE OF CONTENTS

Page

LIST OF FIGURES

LIST OF TABLES

1. INTRODUCTION[1]

1.1. Overview

Acid stimulation in carbonate formations is a widely used stimulation technique to enhance the productivity in carbonate formations by either creating wormhole channels with high permeability (matrix acidizing; injection rates below formation fracture pressure) or by creating a conductive fracture with the acid differentially etching the fracture faces in a non-uniform manner (acid fracturing; injection rates above formation fracture pressure). Hydrochloric acid (HCl) reacts with carbonate formation which consists mainly of calcite and dolomite minerals according to the following reactions:

$$2\mathrm{HCl}_{(aq)} + \overbrace{\mathrm{CaCO_3}_{(s)}}^{\mathrm{Calcite}} \rightarrow \mathrm{CaCl_2}_{(aq)} + \mathrm{H_2O}_{(l)} + \mathrm{CO_2}_{(g)}$$

$$4\mathrm{HCl}_{(aq)} + \overbrace{\mathrm{CaMg(CO_3)_2}_{(s)}}^{\mathrm{Dolomite}} \rightarrow \mathrm{CaCl_2}_{(aq)} + \mathrm{MgCl_2}_{(aq)} + 2\mathrm{H_2O}_{(l)} + 2\mathrm{CO_2}_{(g)}$$

Carbonate formations exhibit unique features such as vugs (large pores) and natural fractures (high permeable channel) which interfere with the flow path and have significant effects on the production/injection. Also, carbonate formations can be tight formations which are characterized by their very low transmissibility (Permeability x Thickness) and hence, they require an advanced production stimulation technique to extract the hydrocarbon inside them. The common industry practice to deal with tight

---

[1] Partially reprinted with permission from “Acid Wormholing in Multistage Acid Fractured Wells Completed in Tight Naturally Fractured Dolomite Formation: Benefits and Impacts on Acid Fracturing Stimulation Design” by K. Aldhayee, M. Ali, and H. Nasr-El-Din, 2019. SPE-191440-18IHFT-MS, Copyright 2019 by Society of Petroleum Engineers.

carbonate reservoirs is to implement the acid fracturing technique in which a viscous pad is injected first to create a hydraulic fracture with certain geometry then followed by the acid system to dissolve part of the fracture walls, etching the faces before the fracture closure to create highly conductive channels inside the fracture. This process requires certain conditions to be satisfied for the treatment to be successful, these conditions are minimizing the leak-off rate of the acid and distributing the acid evenly across the fracture so that it will not be consumed only in the entry of the fracture and it can reach the fracture tip, this can be done by using the gelled acid or emulsified acid which are characterized by their high viscosity and their slow reaction rate with the carbonate.

Another practice in stimulating carbonate formation is closed fracture acidizing (CFA) technique in which acid is injected at matrix acidizing rates in closed fracture that was previously created by acid fracturing to further etch the fracture faces and enhance the connectivity between wellbore and hydraulic fracture. The previous works on CFA technique involve also the minimization of leak-off rate by utilizing retarded acid system (gelled acid or emulsified acid) to achieve this target, but because of the nature of fracture geometry and conductivity, fractures exhibit small flow diameter which promotes a turbulent flow in its flow path and thus, wormholes will be created in perpendicular direction to the fracture by the leak-off of the acid. Minimizing of the acid leak-off in the closed fracture was always the main concern in conducting CFA operations and preventing the creation of wormholes.

1.2. Literature Review

1.2.1. Modeling of Acid Fracturing

Acid fracturing modelling is a challenging process since there are a lot of mechanisms occurring simultaneously, these mechanisms are 1) the propagation of hydraulic fracture in the formation. 2) Acid transport from the stimulation fluid to the fracture walls and the reaction kinetics between them. 3) Induction of fracture conductivity and its decline under closure stress. Each mechanism requires essential properties and informational inputs in order to be able to model it, these inputs include reservoir rock and fluid properties, geomechanical properties of the formation and the stimulation fluid, reaction kinetics and stoichiometric properties of the acid system and the formation, and the statistical mineralogy including the distribution of permeability.

The design of acid fracturing has different approaches and methodologies including: 1) Empirical correlation from laboratory study (Nierode and Kruk, 1973). 2) Fracture propagation from hydraulic fracturing models to induce a fracture, and then utilizing acid transport and kinetics models to simulate differential etching and conductivity (Lo and Dean, 1989; Settari, 1993; Mou et al., 2010; Deng et al., 2011; Oeth et al., 2011; Zhu et al., 2013). 3) Forward Approach (Ueda et al., 2016) to diagnose and evaluate the post-stimulation treatment of acid fracturing. The previous models included the effect of acid leak-off superficially but have not investigated thoroughly the effect of acid leak-off on the performance of acid fracturing treatment.

1.2.2. Acid Fracturing Conductivity

The key factor for a successful acid fracturing treatment is the ability of the acid to etch the fracture surfaces efficiently to create asperities and rough surfaces that support the fracture during the closure and create the fracture conductivity. Fracture conductivity can be defined by **Eq. 1.1**,

$$F_c = k_f w_f \quad \text{(1.1)}$$

Where F_c is fracture conductivity, k_f is fracture permeability and w_f is fracture width. An acid fracture conductivity correlation was developed by Nierode and Kruk (1973) based on laboratory experiments on core samples that were fractured in tension to induce rough surfaces on them. The developed correlation is described by **Eq. 1.2**,

$$F_c = C_1 e^{(-C_2 \sigma_c)} \quad \text{(1.2)}$$

Where σ_c is formation closure stress. C_1 and C_2 are constants that can be described by **Eq. 1.3** and **Eq. 1.4**,

$$C_1 = 0.265(DREC)^{0.822} \quad \text{(1.3)}$$

$$C_2 = \begin{cases} [19.9 - 1.3\ln(RES)] \times 10^{-3},\ if \quad 0 < RES < 20{,}000\, psi \\ [3.8 - 0.28\ln(RES)] \times 10^{-3}, if\ 20{,}000 \le RES \le 500{,}000\, psi \end{cases} \quad \text{(1.4)}$$

Where *DREC* is dissolved rock equivalent conductivity and *RES* is rock embedment strength. The assumption made for this correlation is that fracture conductivity is directly proportional to the amount of etched rock and inversely proportional to formation closure stress in an exponential manner. The correlation is accepted broadly and commonly used in the oil industry. Many researchers conducted acid fracturing experiments to tune and calibrate the correlation to account for different mineralogies and parameters by updating the constants imposed in the correlation (Gangi, 1978; Walsh, 1981; Gong et al., 1999; Pournik et al., 2009).

1.2.3. Closed-Fracture Acidizing

Fredrickson (1986) developed the closed-fracture acidizing (CFA) technique to enhance the performance of conventional acid fracturing that could be declined by the low-conductivity development in the acid fracture or conductivity-decline caused by high closure stress circumstances (Valko, 1998). CFA is a technique in which acid is injected in a closed fracture at rates lower than formation fracture pressure to partially-dissolve the matrix existed in the fracture and enhance the connectivity between the fracture and wellbore, the closed fracture can be natural or hydraulically generated by proppant fracturing or acid fracturing (Knox and Fredrickson 1973, 1974; Broaddus and Fredrickson 1975).

Fredrickson (1986) investigated the effect of CFA under laboratory and field conditions and found that CFA can enhance the fracture conductivity by a factor of six, but it is highly dependent of formation type. Anderson and Fredrickson (1989) introduces a new laboratory methodology for dynamic acid etching test to incorporate and optimize CFA in acid fracturing treatments, and it was found that conventional acid fracturing yields very low conductivity at high closure pressure resulting in crushing the asperities on fracture faces; while CFA yields relatively high conductivities that withstand high closure pressures. Sollman et al. (1990) concluded that fracture conductivity followed by CFA increased to values more than 100,000 md-ft through well tests analysis, and it was found that the fluid flow pattern in low-conductivity fracture during CFA is characterized by linear flow of acid in the fracture associated with conductive wormholes resulted by acid etching. Several field cases demonstrate the success of CFA in enhancing the performance of acid fracturing and sustained high-productivity for a long period of time using different acid systems such as plain acid, gelled acid and emulsified acid (Sizer et al., 1991; Bartko et al., 1992; Wang et al., 2003; Garzon et al., 2008; Nasr-El-Din et al., 2009; Inda et al., 2009; Sarma et al., 2017). Pournik et al. (2011) introduces a new laboratory apparatus to conduct several CFA tests on acid fractured cores, it was demonstrated that acid system with low polymer concentration of 1.5 wt% yields very high fracture conductivity when acid leakoff was allowed as it was observed that CFA generates large wormholes in the direction of acid leakoff which enhances the permeability around the fracture face. Acid injection rates used in CFA range between 1 – 10 bpm according to several field application on acid fracturing treatment or multistage acid fracturing treatment (Itoua et al., 2015; McDuff et al. 2016; AlOtaibi et al., 2017; Mofti et al., 2018).

1.2.4. Wormholes Propagation Models

The aim of carbonate acidizing is to bypass the damaged zone around the wellbore and to create conductive channels by the dissolution of the rock matrix which is known as wormholes. Previous works on the wormholing phenomena were focused on matching the optimum injection rate and minimum pore volume to breakthrough (PVBT) with the experimental results from coreflood experiments and try to reproduce the same acid efficiency curve. Among these works are the ones conducted by several researchers including (Hoefner and Fogler 1988; Hung et al. 1989, Daccord et al. 1993; Wang et al.

1993, Buijse 2000; Liu et al. 1997; Huang et al. 1997; Fredd and Fogler 1998, 1999; Golfier et al. 2002; Panga et al. 2002, 2005; Buijse and Glasbergen 2005; Kalia and Balakotaiah 2007, 2009; Izgec et al. 2010; Maheshwari et al. 2012, 2016; Furui et al. 2012; Tansey 2014; Wu et al. 2015; Ghommem et al. 2015, 2016; Akanni et al. 2017; Schwalbert et al. 2017; Mahrous et al. 2017; Beletskaya et al. 2017). After extensive consolidation of carbonate acidizing models done by Akanni and Nasr-El-Din (2015) which summarize their applications and limitations, those models can be divided into seven categories: 1) Capillary tube approach. 2) Damköhler number approach. 3) Transition pore theory. 4) Network models. 5) Péclet number approach. 6) Semi-empirical approach. 7) Two-scale (averaged continuum) models.

The two-scale model is the most accurate model in producing different dissolution patterns between the acid system and carbonate rocks, and it can precisely match the optimum injection rate and PVBT with the experimental results. It was introduced first by Liu et al. (1997) for modelling of sandstone acidizing. Subsequent works regarding this model after that show the capabilities of the model to capture the dissolution process of carbonate and reproduce the wormholing phenomena occurring in the rock. Even though their model was able to depict the creation of wormholes in carbonates, the effect of mass transfer on the reaction rate was ignored. A three dimensional linear model for carbonates acidizing was developed by Golfier et al. (2002) but the reaction kinetics between the rock matrix and the acid system was not taken into consideration. Panga et al. (2002, 2005) developed a 2D two-scale model where both the effect of mass transfer and reaction kinetics were considered. And that model was developed even further for 2D radial flow by Kalia and Balakotaiah (2007) and 3D radial flow by Cohen et al. (2008). Maheshwari et al. (2013) extended the model to simulate and cover wide range of three-dimensional applications, their model demonstrates good matching results with Fredd and Fogler (1998) experimental data. A uniform porosity distribution was imposed in their model with the incorporation of Carman-Kozeny correlation and modifying the correlation exponents to match the experimental results. Although the model was capable of matching PVBT with the experimental results, the tortuous dissolution patterns were not captured in the model.

Liu et al. (2012) investigated the effect of normally distributed porosities versus uniformly distributed porosities on the wormholing phenomena with radial coordinates. Through this investigation, the results varied significantly on PVBT between the two cases indicating the significant effect of heterogeneity on the acidizing process. And then, Liu et al. (2016) extended the work and imposes spatial correlation for porosity distribution, the resulted wormholes were close to the uniform distribution scenario and the results depict the wormholing phenomena that occurred in the experimental results. Panga et al. (2002, 2005) model described the fluid flow by Darcy's equation, while De Oliveira et al. (2012), Wu et al. (2015), Akanni et al. (2017) and Schwalbert et al. (2017) used Navier-Stokes equations to describe the flow in the two-scale model. A comparison of wormholes simulation was made by Wu et al. (2015) between Darcy's equation and Darcy-Brinkman-Frochheimer (DBF) equation which is an extended form of Navier-Stokes equation, the results show that DBF equation depicts precisely the wormholing phenomena occurred in carbonate acidizing more than Darcy's equation. Akanni et al. (2017) demonstrated that the simulation time using Navier-Stokes equation at very high injection rates was faster than using Darcy's equation (Maheshwari and Balakotaiah 2013).

Akanni et al. (2017) and Ali and Nasr-El-Din (2019) demonstrated how robust the model is when simulating the wormholing phenomena on both limestone and dolostone respectively. According to their results and how accurate the model they used in depicting the wormholes propagation in carbonate acidizing, this computation fluid dynamic model will be used in this study to conduct the simulation of wormholes propagation during CFA operations.

1.2.5. Modeling of Acid Leakoff

Uncontrollable acid leakeoff is considered the most important factor in limiting live acid penetration distance and fracture propagation (Economides and Nolte, 2000). Acid leakoff process was investigated superficially by several researchers (Nierode and Kruk, 1973; Crowe et al., 1989; Settari, 1993; Hill et al., 1995; Zhang et al., 2014). Wormholes are created and propagate through the fracture during acid leakoff in acid fracturing. Many methods have been developed to reduce acid leakoff, such as adding leakoff control additives to the acid (Houchin et al., 1986; Al-Ismail et al., 2008; Jauregui et al., 2011).

Other proposed methods are to increase the acid viscosity and optimize the injection procedure. Until now, there is no model that can simulate the acid leakoff quantitatively to depict the wormholes propagated from the fracture faces. Mou and Zhang (2015) developed a model of acid leakoff for the multistage alternate injection of pad and acid and conducted a study for the acid leakoff behavior during alternate injection and optimized the injection stage, the model was based on the two-scale model developed by Panga et al. (2002, 2005). The effects on formation heterogeneity and fracture conductivity were not considered in the study, and the study was concentrated on the pad characteristic in terms of pad viscosity and the effect of crosslinked fluid in order to minimize the wormholes propagation and acid leakoff.

1.2.6. Impact of Natural Fractures

The presence of natural fractures promotes difficulty in designing hydraulic fracturing treatments. Tight carbonate reservoirs usually associated with significant number of natural fractures (Nnanna and Ajienka 2005; Abass et al. 2007; Jahediesfanjani and Civan 2006). It is not preferred to apply proppant fracturing in naturally fractured carbonate formations since it is always been an issue in the placement of proppants in these kinds of formations that exhibit complex fracture geometry with tortuous paths and high stress environment (Kalfayan, 2008). Modelling of fluid flow in naturally fractured formation should incorporate equations that solve simultaneously the fluid flow in porous medium and free-flow domains (Brinkman 1949; Arbogast and Brunson 2007; Popov et al. 2007; Yao et al. 2010). Dong et al. (1999) investigated the flow of acid in single fracture experimentally, and it was concluded that etching pattern is highly dependent of fracture width. Then, a mathematical model was developed based on the experimental results to predict acid propagation in the presence of natural fractures (Dong et al., 2001), and it was concluded that the presence of natural fractures yields deeper acid propagation. A 3D linear model was developed by Chen et al. (2018) to investigate the effect of fracture aperture, conductivity and orientation on acid penetration distance, and it was found that larger and transversal fractures to the direction of flow require larger acid volumes. Then, the model was extended to incorporate for the effect of temperature by Ma et al. (2018) and the same conclusion was drawn in their work that the presence of natural fractures that are normally distributed requires fewer acid volumes. Ugursal et al. (2018) developed a model for acid fracturing in the presence of intersected natural fractures perpendicular to the hydraulic fracture and studied the effect of natural fractures width, length, density and acid injection rate on the hydraulic fracture conductivity assuming a negligible acid leakoff from the hydraulic fracture through the matrix, it was found that the presence of natural fracture yielded different results depending on fracture geometry and density. Mou et al. (2019) developed a 2D statistical model to simulate wormholes propagation in naturally fractured carbonate utilizing Monte Carlo method and two-scale continuum model to distribute natural fractures in the model with different orientations and densities. Several field cases demonstrate the design of acid fracturing treatment with CFA for naturally fractured carbonate reservoirs (Perez et al., 1998; Wang et al., 2003; Xu et al., 2007; Guillot et al., 2016) as a diverting stage was always included in the design of acid fracturing using viscoelastic surfactant-based system or polymer-based system to mitigate the acid leakoff in the fracture.

1.2.7. Impact of Temperature

Well stimulation techniques depend significantly on formation temperature and the temperature of the treatment fluid. Heat transfer and cooling effect induced by the injected fracturing fluid during acid fracturing treatment can reduce the temperature of the formation exponentially which will alleviate the needs of many acid additives such as corrosion inhibitor intensifiers (Nasr-El-Din et al., 2003). Temperature affect the diffusion coefficients and the reaction rate between the acid system and the formation in which it accelerates the reaction and the dissolution process of acid treatment. Conway et al. (1999) developed a correlation shown on **Eq. 1.5** that can efficiently predict the diffusivity of hydrochloric acid as a function of temperature, acid concentration, and mineral type.

$$D_{(H^+)} = e^{\left(-\frac{A}{T}+B\sqrt{\frac{[Ca^{2+}]}{[H^+]}}+c\sqrt{\frac{[Mg^{2+}]}{[H^+]}}+D[H]+E\right)} \ldots\ldots\ldots\ldots\ldots\ldots\ldots\ldots\ldots\ldots\ldots\ldots\ldots\ldots\ldots (1.5)$$

Where D is the diffusion coefficient, T is the temperature, $[Ca^{2+}]$ is calcium concentration, $[Mg^{2+}]$ is magnesium concentration, $[H^+]$ is hydrogen concentration, A equals -2918.54, B equals -0.589, C equals -0.789, D equals 0.0452, and E equals -4.995 for HCl. **Fig. 1.1** shows the diffusion coefficient of HCl as a function of temperature and acid spending generated from **Eq. 1.5** (Conway et al., 1999).

Temperature accelerates the reaction between the acid system and the rock according to Arrhenius equation described by **Eq. 1.6**.

$$k_s = Ae^{-\frac{E_A}{RT}} \ldots\ldots\ldots\ldots\ldots\ldots\ldots\ldots\ldots\ldots\ldots\ldots\ldots\ldots\ldots\ldots\ldots\ldots\ldots\ldots\ldots\ldots 1.6)$$

Where k_s is the surface reaction rate constant, A is the frequency factor or pre-exponential constant, E_A is the activation energy, and R is the gas constant. Lund et al. (1975) measured the activation energy of HCl-calcite reaction which equals 62.8 KJ/mol. This equation can be utilized to calculate the reaction rate constant for different T values.

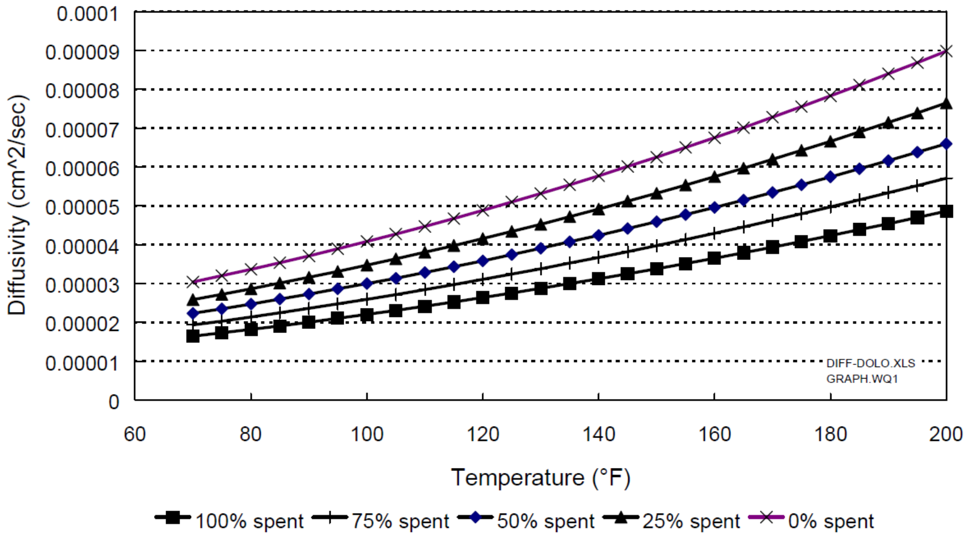

Fig. 1.1 – 15 wt% HCl diffusivity for reaction with calcite at different temperatures and acid concentrations (Conway et al., 1999). Reprinted with permission from SPE-56532-MS.

In acid fracturing, many researches developed heat transfer models in the fracture during acid fracturing treatment to account for heat flux and leakoff rate of fracturing fluid that affect the heat transfer and cooling effect from the induced fracture to the formation (Wheeler, 1969; Whitsitt and Dysart, 1970). Also, many researchers investigated the effect of heat that generated from the acid-rock reaction that takes place at the surfaces of the fracture. It was found that the heat generated from the reaction can raise the fracture temperature up to 60°F which affect the dissolution process during acid fracturing operation and the resulted acid etching pattern (Guo et al., 2014). Matrix acidizing and acid fracturing in high temperature environment imposes a great challenge in conducting successful stimulation treatment as the reaction between the acid and the formation is incontrollable and can interfere with the integrity of downhole equipment due to high corrosion rate of acid system.

1.3. Research Objectives

The objective of this study is to develop a robust CFD model for CFA operation in calcite and dolomite formations that can predict the performance of CFA in terms of the associated dissolution process and wormholing phenomenon occur in the acid-fracture utilizing the two scale continuum model (Panga et al. 2002, 2005) with formulation of Navier-Stokes equation. To study the effect of formation heterogeneity and different mineralogy, the developed CFA models were populated with the porosity distributions profiles that belong to actual core samples of calcite and dolomite formations. A fracture-conductivity model was developed to depict the API fracture-conductivity apparatus for model validation purposes in matching the results of the experimental work done by Pournik et al. (2013). The simulation runs that were used for CFA-Calcite model are conducted to study the effects of different parameters on the performance of CFA including acid injection rate, acid concentration, fracture conductivity, and formation temperature, and a parametric study is conducted accordingly. An analysis of dimensionless quantities is conducted to have a better understanding to the mechanisms governing the dissolution process and wormholing phenomenon associated with CFA operation. For the CFA-Dolomite models, three main models are developed for this study which are the high-permeability dolomite (HPD) vertical well model, the HPD horizontal well model, and the low-permeability dolomite (LPD) horizontal well model. These three models are used to conduct a parametric study on the effect of well geometry, formation permeability, fracture conductivity, presence of natural fractures, and model upscaling in addition to the previous parameters that were used to analyze the CFA-calcite model.

2. METHODOLOGY[2]

2.1. Two-Scale Continuum Model

2.1.1. Model Description

Closed-fracture acidizing was modeled using two-scale continuum model. A 3D computational fluid dynamic (CFD) model was developed using ANSYS FLUENT to cover the reactive flow of acid during CFA, where Navier-Stokes equation was utilized to describe the flow field. The reaction parameters and the evolution of porosity have been calculated using the user-defined functions that were provided to the simulator in order to model acid propagation during CFA.

2.1.2. Darcy-Scale Equations

In this section, Darcy-scale equations are demonstrated for the two-scale continuum model that describe the nature of the flow in porous medium. Navier-Stokes equation is coupled with the Darcy-scale equation to formulate the fluid flow field as described in **Eq. 2.1**,

$$\frac{\partial(\rho \boldsymbol{u})}{\partial t} + \nabla \cdot (\rho \boldsymbol{u}\boldsymbol{u}) = -\nabla p + \mu \nabla^2 \boldsymbol{u} - \frac{\mu}{\boldsymbol{K}} \boldsymbol{u} \text{ ....} \quad (2.1)$$

Where $\boldsymbol{u}$ is the superficial velocity vector, ρ is the fluid density, p is the fluid pressure, μ is the fluid viscosity, and $\boldsymbol{K}$ is the permeability tensor. **Eq. 2.1** illustrates the change in momentum through the change of momentum rate and the change in advective

---

[2] Partially reprinted with permission from “Acid Wormholing in Multistage Acid Fractured Wells Completed in Tight Naturally Fractured Dolomite Formation: Benefits and Impacts on Acid Fracturing Stimulation Design” by K. Aldhayee, M. Ali, and H. Nasr-El-Din, 2019. SPE-191440-18IHFT-MS, Copyright 2019 by Society of Petroleum Engineers.

acceleration as described in the left-hand side of the equation. It also accounts for the fluid forces described by the three terms in the right-hand side in which the first term represents the pressure drop, the second term represents the diffusive transport, and the third term represents the Darcian losses of the flow. The inertial term is included for the fluid flow in the fracture. The flow in porous medium is described by Darcy flow accounting for the permeability of the medium. The flow in the wormholes is diffusion-dominant and it follows the flow patter of Navier-Stokes formulation.

The continuity equation is described in **Eq. 2.2** as a result of mass equilibrium of fluids in the mass balance constitutive equation. It represents the local change in volume during the dissolution process of porous medium as following,

$$\frac{\partial \varepsilon}{\partial t} + \nabla \cdot \boldsymbol{u} = 0 \ldots\ldots\ldots\ldots\ldots\ldots\ldots\ldots\ldots\ldots\ldots\ldots\ldots\ldots\ldots\ldots\ldots\ldots\ldots\ldots\ldots\ldots\ldots\ldots(2.2)$$

The governing equation of acid species transport from bulk fluid to the surface is described in **Eq. 2.3** as,

$$\overbrace{\varepsilon \frac{\partial C_f}{\partial t}}^{\substack{\text{Acid} \\ \text{Accumulation}}} + \overbrace{\boldsymbol{u}.\nabla C_f}^{\substack{\text{Acid} \\ \text{Convection}}} = \overbrace{\nabla \cdot \left(\varepsilon \boldsymbol{D_e} \cdot \nabla C_f\right)}^{\substack{\text{Acid} \\ \text{Dispersion}}} - \overbrace{k_c a_v \left(C_f - C_s\right)}^{\substack{\text{Amount of} \\ \text{acid transported} \\ \text{to rock surface} \\ \text{from fluid phase}}} \ldots\ldots\ldots\ldots\ldots\ldots\ldots\ldots(2.3)$$

Where ε is medium porosity, C_f is the acid concentration in the bulk, C_s is the acid concentration at the fluid-solid interface, $\boldsymbol{D_e}$ is the effective dispersion tensor, k_c is the local mass-transfer coefficient, and a_v is the available interfacial area for reaction per unit volume of porous medium. $\boldsymbol{D_e}$ and k_c can be calculated from correlations utilizing the dimensionless Sherwood number and the longitudinal and transversal dispersion coefficients (Gupta and Balakotaiah, 2001; Balakotaiah and West, 2002) as described in **Eq. 2.4**, **Eq. 2.5**, and **Eq. 2.6**:

$$Sh = \frac{2\boldsymbol{k_c r_p}}{D_m} = Sh_\infty + 0.7Re_p^{1/2}Sc^{1/3} \qquad (2.4)$$

$$\boldsymbol{D_{eX}} = \alpha_{os}D_m + \frac{2\lambda_X\|\boldsymbol{u}\|\boldsymbol{r_p}}{\varepsilon} \qquad (2.5)$$

$$\boldsymbol{D_{eT}} = \alpha_{os}D_m + \frac{2\lambda_T\|\boldsymbol{u}\|\boldsymbol{r_p}}{\varepsilon} \qquad (2.6)$$

$$Re_p = \frac{2\|u\|r_p}{v} \qquad (2.7)$$

$$Sc = \frac{v}{D_m} \qquad (2.8)$$

Where *Sh* is the Sherwood number, which is defined by dimensionless mass transfer coefficient, r_p is the pore radius, D_m is the acid diffusivity, sh_∞ is the asymptotic Sherwood number, Re_p is the pore scale Reynold's number which is defined as in **Eq. 2.7**, *Sc* is the Schmidt number which is defined as in **Eq. 2.8**, v is the kinematic viscosity, α_{os} is the pore connectivity constant, D_{eX} is the longitudinal dispersion coefficient, D_{eT} is the transversal dispersion coefficient in the y- and z- directions, λ_X and λ_T are constants based on porous medium structure. The transport phenomena governed by diffusion and advection processes are incorporated in those demonstrated correlations (Maheshwari and Balakotaiah, 2013).

Eq. 2.9 demonstrates the reaction rate that establishes equilibrium between the amount of acid transported from the bulk to the surface and the amount of acid species reacted at the surface.

$$k_c(C_f - C_s) = R(C_s) \qquad (2.9)$$

The porosity evolution during the dissolution process is described by **Eq. 2.10** which is derived from the mass balance between the consumed acid and the dissolved rock surface.

$$\frac{\partial \varepsilon}{\partial t} = \frac{R(C_s)a_v\alpha}{\rho_s} \quad (2.10)$$

Where $R(C_s)$ is the reaction rate of the acid-rock system, ρ_s is the rock density, and α is the acid dissolving power. The reaction rate $R(C_s)$ can also be described as in **Eq. 2.11** where k_s is the constant of dissolution rate and n is the reaction exponent.

$$R(C_s) = k_s {C_s}^n \quad (2.11)$$

The dissolution rate constant (k_s) and the reaction exponent (n) can be calculated from **Eq. 2.12** and **Eq. 2.13** for hydrochloric acid (HCl) and dolomite system using Lund et. al (1973) correlations.

$$k_s = k_{so} e^{-\frac{E}{RT}} \quad (2.12)$$

$$n = \frac{RT}{(1-aT)X_m} \quad (2.13)$$

Where k_{SO} is the frequency factor, E is Arrhenius activation energy, R is the ideal gas constant (8.314 J / mol. K), T is the absolute temperature, and a and X_m are Freundlich isotherm parameters. For a system composed of hydrochloric acid and calcite, the reaction exponent is equal to 0.63 as recommended by Lund et al. (1975).

2.1.3. Pore-Scale Equations

Two-scale continuum model considers the reaction of acid with the porous medium at pore scale. The dissolution phenomenon caused by acid propagation in the medium tends to increase its porosity which leads to an increase in permeability of the medium, pore-radius distribution, and interfacial surface area per unit volume. Carman-Kozeny (1956) correlation incorporates all these mathematical relationships between the porosity and rock properties. Maheshwari and Balakotaiah (2013) coupled Carman-Kozeny correlation with the pore-scale equations described in **Eq. 2.14**, **Eq. 2.15**, and **Eq. 2.16**.

$$\frac{\boldsymbol{K}}{\boldsymbol{K_o}} = \left(\frac{\varepsilon}{\varepsilon_o}\right)^{\gamma} \left(\frac{\varepsilon(1-\varepsilon_o)}{\varepsilon_o(1-\varepsilon)}\right)^{2\beta} \qquad (2.14)$$

$$\frac{\boldsymbol{r_p}}{\boldsymbol{r_{po}}} = \left(\frac{\varepsilon(1-\varepsilon_o)}{\varepsilon_o(1-\varepsilon)}\right)^{\beta} \qquad (2.15)$$

$$\frac{\boldsymbol{a_v}}{\boldsymbol{a_{vo}}} = \left(\frac{\varepsilon}{\varepsilon_o}\right) \left(\frac{\varepsilon(1-\varepsilon_o)}{\varepsilon_o(1-\varepsilon)}\right)^{-\beta} \qquad (2.16)$$

Where γ and β are matching parameters for specified porous medium that correspond to pore-connectivity and pore broadening, respectively.

2.2. Solution Method

2.2.1. Model Implementation

Two-scale continuum model with Navier-Stokes formulation was implemented using ANSYS FLUENT, a computational fluid dynamics platform with several numerical schemes that can solve the set of governing equations in the two-scale model efficiently. The solution algorithm is constructed in a way to solve the momentum, mass continuity and the acid-transport equations in the closed-fracture and the rock-matrix at the Darcy scale. The algorithm is coupled with user-defined functions and routines formulated using C programming language to solve the equations of pore-scale in the two-scale continuum model including porosity evolution, updating the parameters in the pore-scale, and combining the flow equations in the pore-scale with the Darcy-scale. **Fig. 2.1** demonstrates the workflow of the solution algorithm and the sequence of equations solved in the two-scale model. The simulation models were run on Texas A&M University (TAMU) High Performance Research Computing (HPRC) clusters to benefit from the parallel processing.

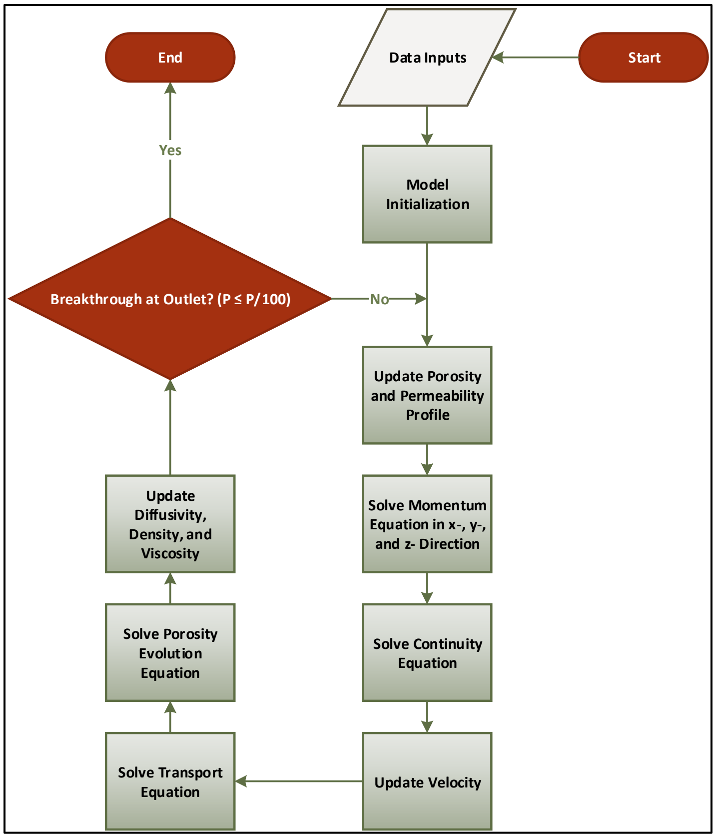

Fig. 2.1 – Workflow of solution algorithm illustrating the sequence of equations solved and the updated properties.

2.2.2. Numerical Scheme

The solution technique adapted to solve two-scale continuum model is the finite volume method that is formulated in the utilized computational fluid dynamics platform. ANSYS Fluent is based on that method to solve the momentum conservation and transport equations in the Darcy-scale and pore-scale of closed-fracture acidizing model. The system of partial differential equations that forms the backbone of two-scale continuum model is converted to its corresponding integral form that preserve the mass conservation laws, and then converted to system of algebraic equations that are solved simultaneously and numerically using finite volume method.

The utilized pressure-velocity coupling technique is Pressure-Implicit with Splitting of Operators (PISO). The PISO algorithm is an enhanced numerical version of Semi-Implicit Method for Pressure Linked Equations (SIMPLE) scheme to solve Navier-Stokes equation with the advantage of less required iterations and larger time steps that optimize the computational efforts. PISO scheme is recommended to solve a system of multiple transport phenomena associated with the reactive flow that is in transient state. **Fig. 2.2** summarizes the workflow of PISO scheme in solving two-scale continuum model.

The acid consumption during the dissolution process and the bulk concentration is calculated numerically at the cell faces using the least squares cell based spatial discretization method combined with a second-order upwind scheme for a better accuracy. For the pressure interpolation scheme, Pressure-Staggering Option (PRESTO) is adapted to efficiently and accurately calculate the pressures during the closed-fracture acidizing process, this scheme is recommended for fluid flow in porous media. As for the momentum interpolation scheme, second-order upwind scheme is adapted to solve the momentum term and update the required velocities for a better accuracy. The optimum number of gird blocks was determined after several trial and error attempts to obtain the optimum accuracy from the simulation runs. The proper size of time step was determined based on the type of formation that is dealt with. For calcite formation, time step size was in the range of 0.005 to 0.01 seconds to capture all the events that take place during the CFA dissolution process due to the accelerated reaction rate in the acid-calcite system. For dolomite formation, time step size was in the range of 0.1 to 0.5 due to the extremely slow reaction rate in the acid-dolomite system that provides tolerance for larger time steps without numerical divergence. And for the same reason, the number of grid blocks required for the calcite model is exponentially larger than the required number of grid blocks in the dolomite model as it will be demonstrated in the subsequent sections.

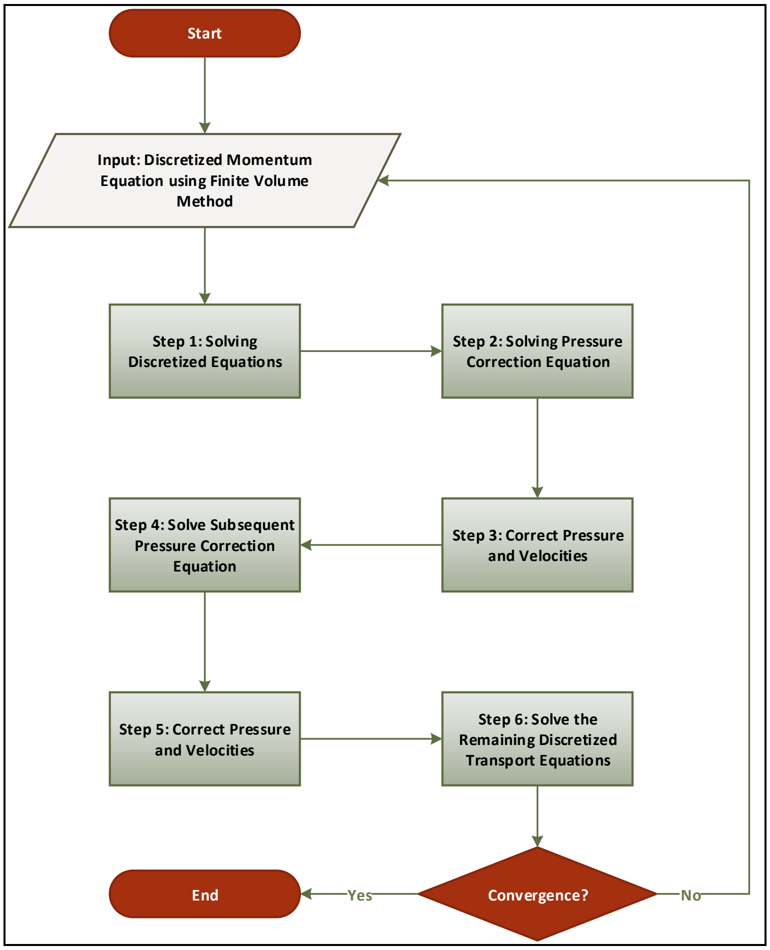

Fig. 2.2 – PISO algorithm to solve the system of equations in the two-scale continuum model.

2.3. Model Development and Initialization

2.3.1. Porosity Distribution Profile

CFA model is a dual-permeability model that consists of the conductive fracture and the porous medium representing the formation. The constructed models are populated with natural porosity profiles from cores that represent the actual porosity distribution presented downhole. Three different cores are used in this study which are Indiana Limestone, Silurian Dolomite, and Guelph Dolomite. **Table 2.1** shows the properties of the mentioned cores used in this study.

Table 2.1 – Rock properties of different cores.

Core Sample	**Porosity**	**Permeability (md)**
Indiana Limestone	0.158	4.00
Silurian Dolomite	0.170	50.66
Guelph Dolomite	0.109	0.53

Initial porosity field in the domain was obtained from Computed Tomography (CT) scans of the mentioned cores to study the variations in mineralogy and permeability. Dry and wet CT scans are measured from the apparatus for different core samples that are mentioned in **Table 2.1** to generate the porosity profiles using **Eq. 2.17** (Akin and Kovescek, 2003).

$$\varepsilon = \frac{CT_{wet} - CT_{dry}}{CT_{water} - CT_{air}} \qquad \ldots\ldots 2.17)$$

Accordingly, three different porosity profiles are generated for Indiana Limestone, Silurian Dolomite that was studied by Ali and Nasr-El-Din (2019), and Guelph Dolomite.

Fig. 2.3, **Fig. 2.4**, and **Fig. 2.5** show the histogram and porosity distribution generated by CT scans for Indiana Limestone, Silurian Dolomite, and Guelph Dolomite, respectively. The porosity distributions were utilized to initialize the porous domain for several models that were developed to validate the CFA models and to conduct parametric study for the constructed calcite and dolomite CFA models. For dolomite porosity distributions, two models were developed to study the effect of permeability which are high-permeability dolomite (HPD) and low-permeability dolomite (LPD). The HPD model adapts the porosity profile shown in **Fig. 2.4** which belongs to Silurian Dolomite core, while the LPD model adapts the porosity profile shown in **Fig. 2.5** which belongs to Guelph Dolomite core. Two calcite models were developed for this study which are the validation model of fracture-conductivity experiment and CFA-Calcite model that is used to conduct the parametric study on CFA process in calcite formation. Both models adapt the porosity profile shown in **Fig. 2.3** which belongs to tight Indiana Limestone core.

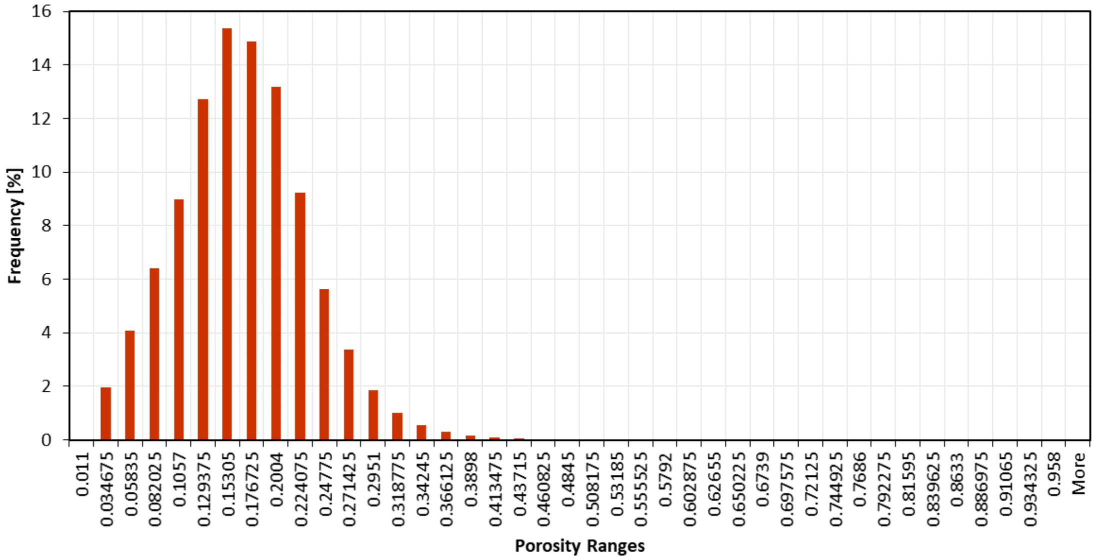

Fig. 2.3 – Histogram and porosity distribution generated from CT scan of Indiana Limestone core.

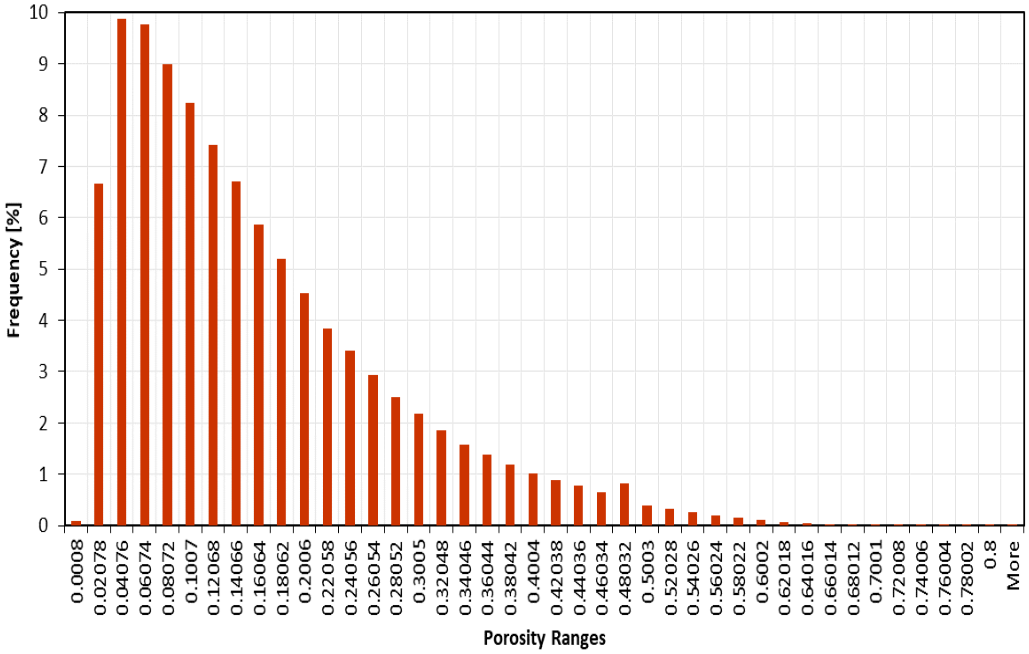

Fig. 2.4 – Histogram and porosity distribution of high-permeability Dolomite (HPD) generated from CT scan of Silurian Dolomite core.

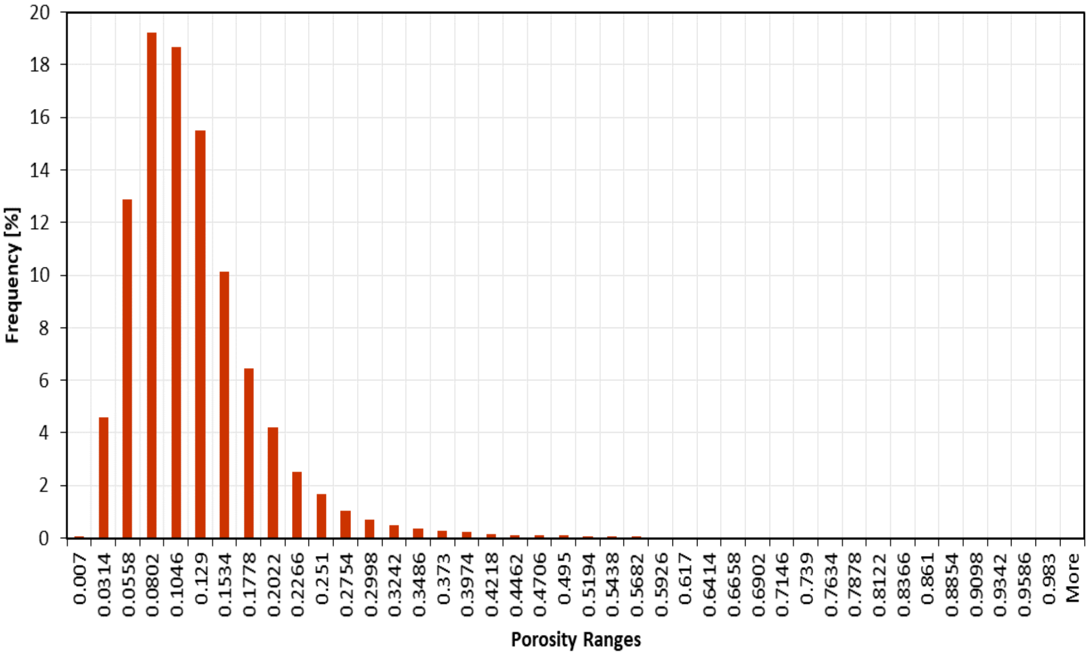

Fig. 2.5 – Histogram and porosity distribution of low-permeability Dolomite (LPD) generated from CT scan of Guelph Dolomite core.

2.3.2. Fracture-Conductivity Model for Validation

A three-dimensional CFD model was constructed to validate the developed CFA model in capturing the acid-etching pattern and wormholing phenomenon. The validation model is developed based on the actual dimension of a modified API conductivity cell with a body dimension of 10x3.25x8 in. with 7.25x1.75 in. hole. The model has a length of 7.11 in., a thickness of 3 in., a width of 1.61 in., and a fracture aperture of 0.12 in. to allow the acid to flow into the fracture and etch the fracture's surfaces. The model is validated with the experimental work that was conducted by Pournik et al. (2013), in which the effect of acid-spending was investigated on the etching pattern and acid-fracture conductivity. The model is populated with the porosity distribution shown in **Fig. 2.3** of Indiana Limestone that has a porosity of 0.158 and a permeability of 4 md to match the core that was used in the experimental work. **Fig. 2.6** shows the developed validation model with the specified dimensions and porosity distribution. The developed model has 1.8 million grid blocks to capture the dissolution process accurately.

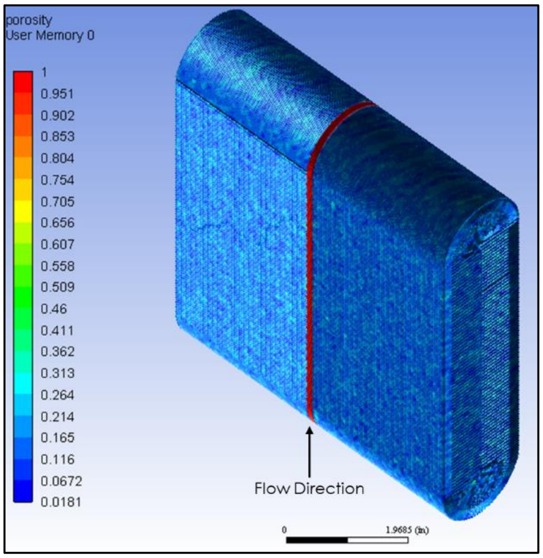

Fig. 2.6 – Fracture-conductivity model for validation.

The matching criteria in this study is based on a qualitative relationship between the straight HCl and gelled HCl with low polymer loading that was presented in the experimental work. The fluid used in the study is a straight HCl with different acid concentrations of 5, 10, and 15 wt%. To depict the experimental procedures, a flow rate of 1 L/min was used in the model with an injection duration of 15 minutes. The temperature used was 150°F.

For the initial conditions, zero acid flux and zero acid concentration were imposed in the computational domain.

For the boundary conditions, the fracture inlet at the bottom of the model was used as a velocity inlet as shown in **Fig. 2.6**. The fracture outlet at the top of the model was set as a pressure outlet. As for the sides of the model, the imposed boundary conditions were constant mass flux to control the leakoff of the acid as in the experimental work. **Table 2.2** shows the leakoff rates and mass fluxes of different acid concentrations that were used in the experimental work done by Pournik et al. (2013). As for the other interfaces, wall condition is imposed in all of them.

Table 2.2 – Leakoff rates and mass fluxes of different acid concentrations used in the simulation cases.

Simulation Cases	**Leakoff Rate Controlled in the Experiments (ft/min)**	**Density Measured in the Experiments (g/cc)**	**Mass Flux (kg/s)**
15 wt% HCl	0.0035	1.07	1.4761E-05
10 wt% HCl	0.006	1.11	2.6251E-05
5 wt% HCl	0.0052	1.16	2.3775E-05

As for the simulation parameters, the reaction exponent equals 0.63 from Lund et al. (1975), and the 15 wt% HCl viscosity at 150ºF is 0.65 cp (Nishikata et al., 1981). As for the values of initial mean pore size, initial interfacial area per unit volume, constant in dispersion correlation, and constants in axial dispersion correlation and in transversal dispersion correlation, they were extracted from the simulation study conducted by Maheshwari and Balakotaiah (2013). Acid diffusion coefficient and surface reaction rate are estimated initially from **Fig. 1.1** and **Eq. 1.6**, respectively. Then, the values are calibrated to acquire a qualitative match between the experimental work and the simulation study as demonstrated in section 3.1. **Table 2.3** summarizes the simulation parameters used in the validation study with the experimental work.

Table 2.3 – Simulation parameters used in the validation study at 150°F.

Simulation Parameters, Unit	**Value**
Initial average porosity (ε)	0.158
Initial average permeability (k), md	4
Initial mean pore size (r_{p_o}), µm	1
Initial interfacial area per unit volume (a_{v_o}), cm^{-1}	50
Pore connectivity parameter (γ)	1
Pore broadening parameter (β)	1
Rock density (ρ_s), g/cc	2.71
Surface reaction rate constant (k_s), $\frac{\text{mol}^{1-n}}{\text{cm}^{2-3n}.\text{s}}$	0.2
Surface reaction exponent (n)	0.63
Acid diffusion coefficient (D_m), cm^2/s	2.5E-4
15 wt% HCl viscosity (μ), cp	0.65
Constant in dispersion correlation (α_{os})	0.5
Constant in axial dispersion correlation (λ_x)	0.5
Constant in transverse dispersion correlation (λ_l)	0.1

2.3.3. Closed-Fracture Acidizing Model

The main model for this study is the closed-fracture acidizing "CFA" model. Several CFA models were developed to study different parameters and to cover different mineralogical compositions. The study covers the closed-fracture acidizing operation on limestone formation; which is predominantly composed of calcite mineral, and dolostone formation; which is predominantly composed of dolomite mineral.

3D CFD models were developed to study the parameters that affect CFA operations for vertical and horizontal wells, with and without natural fractures. Initial porosity field in the domain was obtained from Computed Tomography (CT) scans of different cores shown in **Table 2.1**. Fracture was imposed in the model as a high porosity/permeability conduit, as shown in **Fig. 2.7**. The figure shows the CFA model developed for dolomite formation and for vertical and horizontal wells with 1.83 and 1.73 million grid blocks, respectively. A concentrated grid pattern around the area of fracture was imposed to capture the wormholing phenomenon during CFA. It was extended to cover the calcite formation as well with 6.7 million grid blocks, since the reaction kinetics of HCl-Calcite system is exponentially larger than HCl-Dolomite system, so that it requires larger number of grid blocks to cover the accelerated dissolution process during CFA operation. The model has dimensions of 0.2 meter length, 0.2 meter width and 0.1 meter height. Wellbore radius in the model for both vertical and horizontal wells is 0.02 meters. To alleviate the need of large number of grids and computational capabilities, only half-fracture length was considered in the developed models. Fracture conductivity was calculated from **Eq. 1.1** utilizing the Carman-Kozeny correlation (1956) to convert porosity to permeability as shown in **Eq. 2.14**.

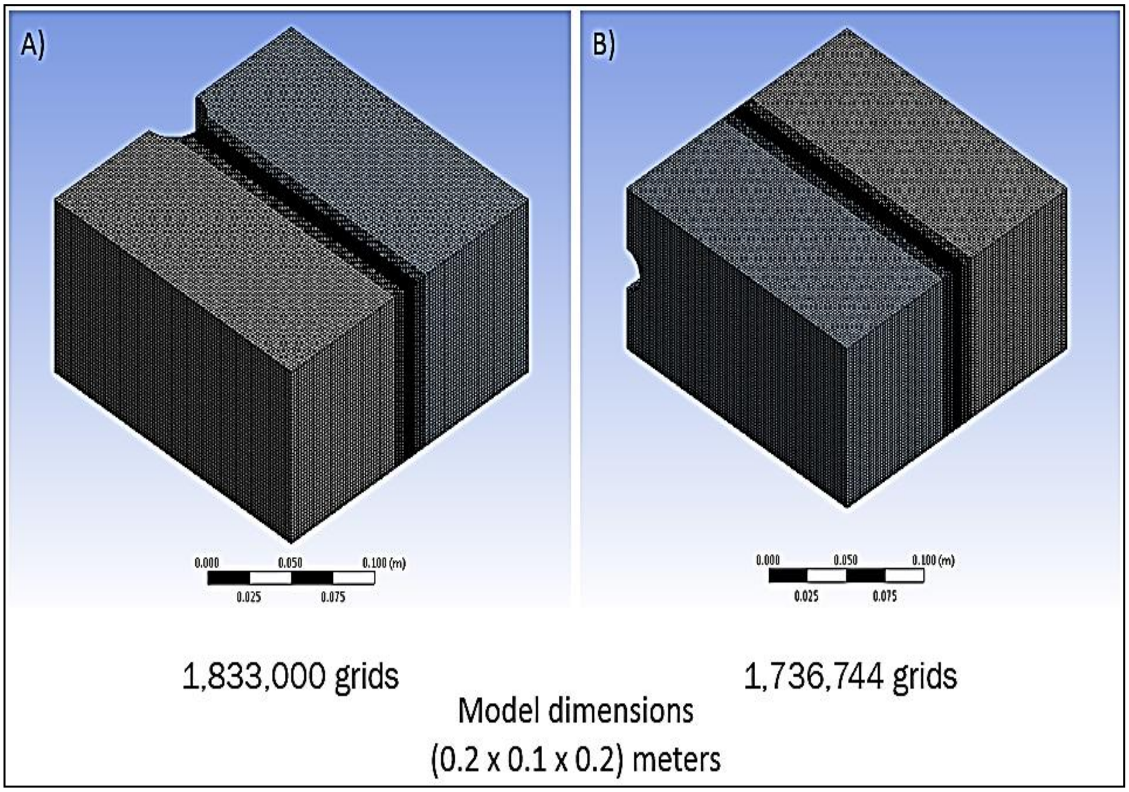

Fig. 2.7 – CFD model dimensions and number of grids. A) Vertical well model. B) Horizontal Well Model. Reprinted with permission from SPE-191440-18IHFT-MS.

For Calcite formation, a CFA model was developed using the porosity profile shown in **Fig. 2.3**. A horizontal well was imposed in the model with the mentioned dimensions as shown in **Fig. 2.8**. For Dolomite formation, Four models were developed for this study which are A) vertical well with high-permeability dolomite (HPD) distribution, B) horizontal well with high-permeability dolomite distribution, C) horizontal well with low-permeability dolomite (LPD) distribution and D) horizontal well with low-permeability dolomite (LPD) distribution and natural fractures.

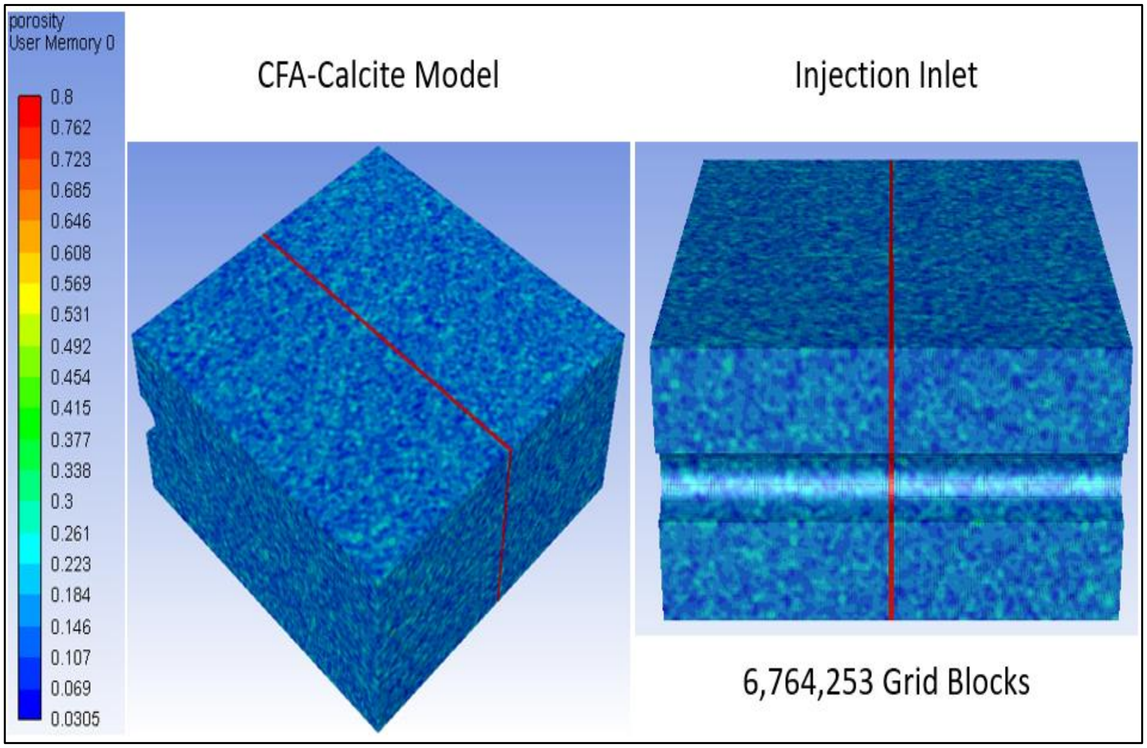

Fig. 2.8 – CFA model for Calcite formation illustrating the total number of grid blocks.

The porosity distribution of vertical well HPD model is presented in **Fig. 2.9A**. Horizontal well model was populated with two different porosity distributions which are HPD and LPD shown in **Fig. 2.4** and **Fig. 2.5**, respectively.

Natural fractures were studied using the LPD model. **Fig. 2.9B** shows the model dimensions and the total number of grids for the horizontal model. **Fig. 2.9B** shows the porosity distribution of horizontal well HPD model. The horizontal well model was initialized with LPD distribution to depict tight dolomite formation. **Fig. 2.9C** and **Fig. 2.9D** show the porosity distribution of horizontal well LPD model. Fracture conductivity analysis was carried out for the same horizontal LPD model with different fracture conductivities imposed in the model. The simulation models were run on Texas A&M

University (TAMU) High Performance Research Computing (HPRC) clusters to benefit from the parallel processing.

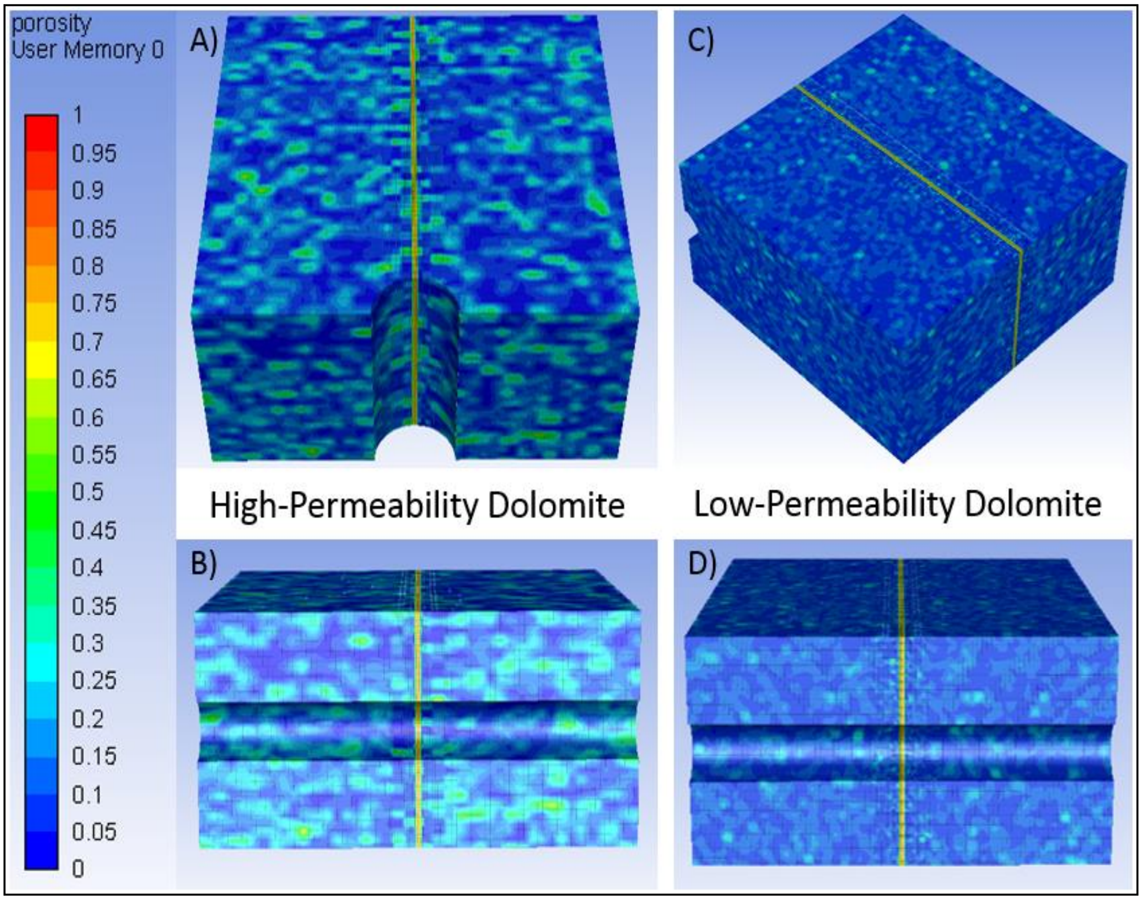

Fig. 2.9 – Porosity distribution of CFA models. A) Vertical well HPD model. B) Horizontal well HPD model. C) Horizontal well model LPD model. D) Horizontal well model LPD model (injection inlet view). Reprinted with permission from SPE-191440-18IHFT-MS.

In the current study, CFA operations in Calcite and Dolomite formations at 150°F were studied. For calcite model, the simulation parameters presented in **Table 2.3** were used after the process of calibration with the validation model. The simulations are terminated after an injection period of 10 minutes which considered to be the average injection time of a typical CFA operation.

For dolomite model, the simulation parameters presented in **Table 2.4** (Ali and Nasr-El-Din, 2019) were used. Most of the parameters are acquired from the same sources that were used to establish the calcite model. Simulations are terminated when the pressure drop is 100 times less than the initial pressure drop, this happens when acid fingers reach the sides (outlet) of the model.

Table 2.4 – Simulation parameters used in the HPD and LPD models at 150°F.

Simulation Parameters, Unit	**Value**
Initial average porosity (ε) for HPD model	0.170
Initial average porosity (ε) for LPD model	0.109
Initial average permeability (k) for HPD model, md	50.66
Initial average permeability (k) for LPD model, md	0.53
Initial mean pore size (r_{p_o}), µm	1
Initial interfacial area per unit volume (a_{v_o}), cm^{-1}	50
Pore connectivity parameter (γ)	1
Pore broadening parameter (β)	1
Rock density (ρ_s), g/cc	2.77
Surface reaction rate constant (k_s), $\frac{\mathrm{mol}^{1-n}}{\mathrm{cm}^{2-3n}.\mathrm{s}}$	5E-3
Surface reaction exponent (n)	0.65
Acid diffusion coefficient (D_m), cm^2/s	5E-4
15 wt% HCl viscosity (μ), cp	0.65
Constant in dispersion correlation (α_{os})	0.5
Constant in axial dispersion correlation (λ_x)	0.5
Constant in transverse dispersion correlation (λ_l)	0.1

To study the effect of temperature on the CFA-Calcite model, acid diffusion coefficient is estimated from **Fig. 1.1** for temperature values of 100°F and 200°F. Surface reaction rate constant is calculated from **Eq. 1.6** for the same range of temperatures given an activation energy of 62.8 KJ/mol for the dissolution of calcite in HCl acid (Lund et al., 1975). The values of diffusion coefficient are corrected by linear interpolation of the estimated parameters with the calibrated parameters of the validation model to maintain same trend. Densities and viscosities of HCl for 100°F and 200°F are extracted from the experimental work done by Nishikata et al. (1981), assuming constant acid density and viscosity with respect to concentration. **Table 2.5** illustrates the simulation parameters used in the CFA-Calcite model for different temperatures.

Table 2.5 – Simulation parameters used in the CFA-calcite model for different temperatures.

Simulation Parameters, Unit	**Temperature [°F]**		
	100	**150**	**200**
Acid Diffusion Coefficient (D_m) from Fig. 1.1, cm^2/s	3.5E-5	5.5E-5	8E-5
Corrected Acid Diffusion Coefficient (D_m), cm^2/s	1.59E-04	2.5E-4	3.64E-04
Surface Reaction Rate Constant (k_s) from Eq. 1.6, cm/s	0.0273	0.2	1.084
15 wt% HCl Density (ρ), g/cc	1.1	1.096	1.084
15 wt% HCl Viscosity (μ), cp	0.9	0.65	0.45

3. MODEL VALIDATION

Two-scale continuum model was proved to be a robust model in capturing the process of acid dissolution in calcite and dolomite rocks, and the resulting wormholing patterns under different conditions (Akanni et al., 2017; Ali and Nasr-El-Din, 2019). This model is extended to cover the acid etching and wormholing phenomena for closed-fracture acidizing in calcite and dolomite. The developed CFA model is validated with the experimental work that covers the effect of different acid concentrations on etching patterns during acid fracturing (Pournik et al., 2013). In the experimental work, gelled acid was used to study the acid etching on Indiana Limestone with a permeability of 4 md and acid injection rate of 1 L/min at 150°F. The simulation runs adapted the same experimental conditions as demonstrated in section 2.3.2. An important point to highlight is that the laser profilometer which is used to characterize the acid etching on fractures faces has a limitation in measuring the depth profile of the etching pattern up to 0.5 inch, and so the apparatus is unable to identify the wormholes that were caused by the leakoff etching. The average etched width is calculated using **Eq. 3.1** on the etched fracture surface.

$$w_{etched} = \frac{(EV_{post-acidizing})-(EV_{pre-acidizing})}{A_{Fracture}} \qquad \ldots\ldots 3.1)$$

Where w_{etched} is the average etched width of the fracture, $EV_{pre\text{-}acidizing}$ is the surface volume of the etched fracture face before acidizing, $EV_{post\text{-}acidizing}$ is the surface volume of the etched fracture face after acidizing, and $A_{Fracture}$ is the surface area of the fracture. The numerator of **Eq. 3.1** can be calculated using the convex hull algorithm in MATLAB that is able to estimate the total etched volume of the fracture surface. The surface area of the fracture which is the denominator of **Eq. 3.1** is given by the dimensions of the modified API conductivity cell that was elaborated in section 2.3.2.

The objective of this study is to come up with a qualitative matching between the results of the experimental work and the simulation runs that establishes the relationship between the straight HCl and gelled HCl by comparing the etched surface profile and the average etched width of the two acid systems.

Imposing the suitable boundary conditions in **Table 2.2** on the fracture-conductivity model in **Fig. 2.6** and using the simulation parameters described in **Table 2.3** to depict the conditions of the experimental work, the validation model was run for 15 minutes and with several simulation scenarios that cover different acid concentration including 5, 10, and 15 wt% HCl.

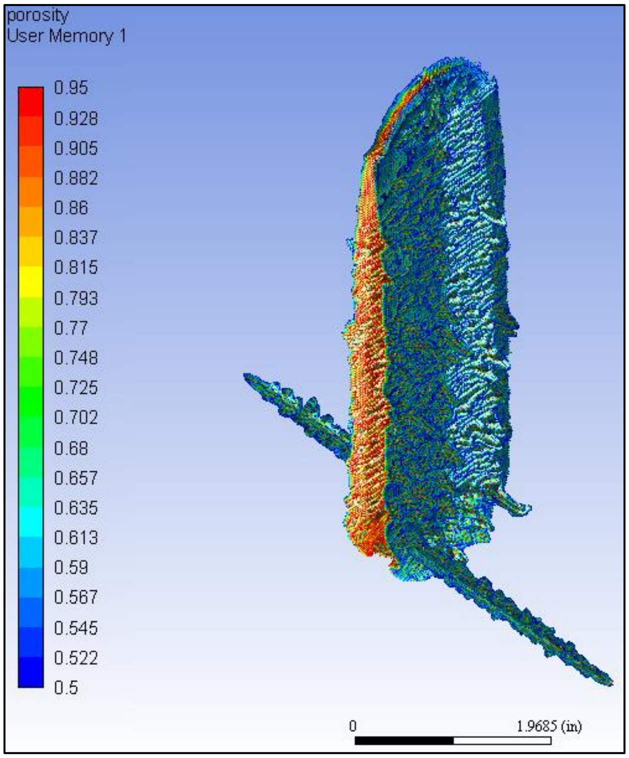

Fig. 3.1 – Acid wormholing of 15 wt% HCl on the fracture-conductivity model.

Fig. 3.1 illustrates the wormholing phenomenon of 15 wt% HCl simulation run on the validation model. Wormholes are associated with the acid leakoff into the formation during the fracture acidizing process. It can be noticed that there is a single dominant wormhole propagated from the fracture into the boundary to satisfy the imposed boundary condition of 0.0035 ft/min on the leakoff direction of the fracture conductivity cell used in the experiment. **Fig. 3.2** shows the acid etching on the fracture surface for the 15 wt% HCl simulation run on the validation model.

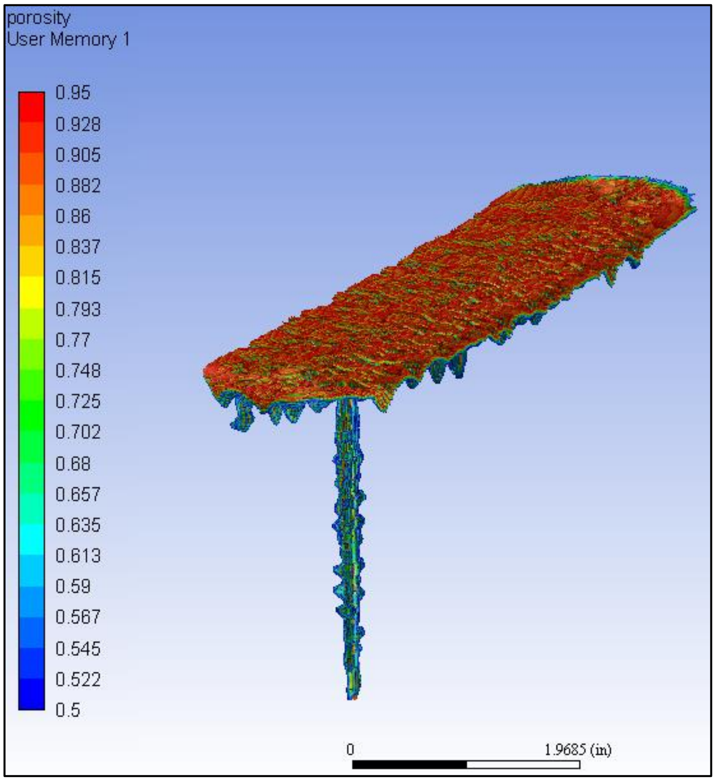

Fig. 3.2 – Etched surface profile caused by 15 wt% HCl on the fracture face in the validation model.

To further asses the ability of the two-scale continuum model in capturing the acid etching pattern, it was compared with the acid etching pattern resulted from the experiment.

Fig. 3.3 shows the etched surface profile of 15 wt% HCl on the fracture surface in both modeling and experimental results. The results coincide with the observations obtained from the previous works in the literature. In the experimental work, the type of acid etching is channel etching which is typical for gelled HCl system that is characterized with a large channel in the middle of the fracture surface due to the concentrated acid species [H^+] at the acid front during the dissolution process. In the modeling results, the type of acid etching is roughness etching which is typical for straight HCl system. The figure also shows the average etched width of both works with the modeling etched width calculated from **Eq. 3.1**, and it shows that the straight HCl system induces rougher and more erratic surface pattern than the gelled HCl system, and that observation aligns with the results demonstrated in the literature.

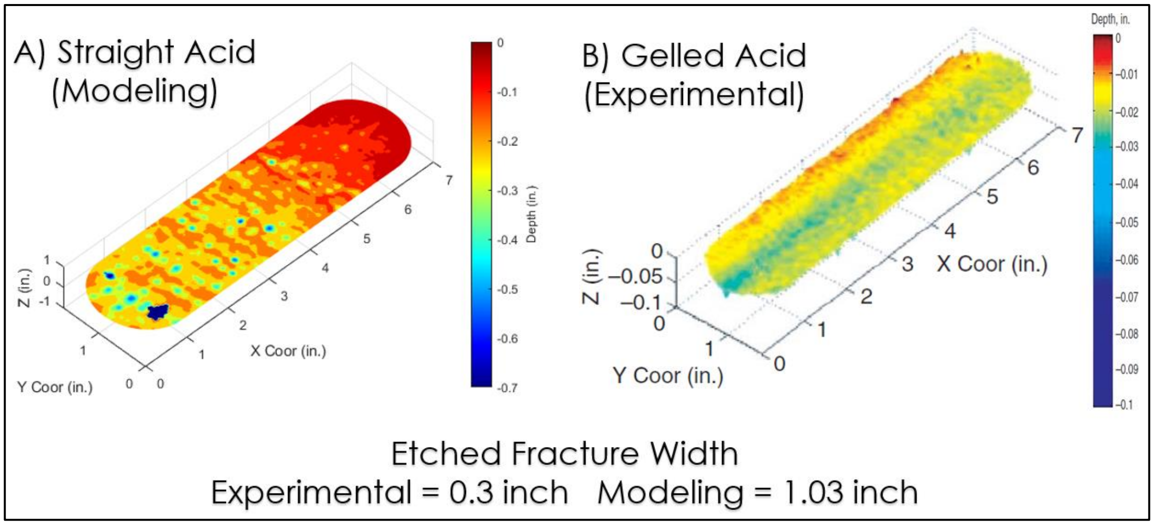

Etched Fracture Width
Experimental = 0.3 inch Modeling = 1.03 inch

Fig. 3.3 – Acid Etching of 15 wt% HCl on the fracture surface. A) Fracture-conductivity model. B) Experimental results from Pournik et al. 2013. Reprinted with permission from SPE-136217-PA.

Fig. 3.4 illustrates the wormholing phenomenon of 10 wt% HCl simulation run on the validation model. The wormholes propagated from the fracture in this case are not as dominant as the previous case because of the lower acid concentration. It can be observed that the wormholing phenomenon follows the same trend where the wormholes are concentrated around the vicinity of the injection inlet.

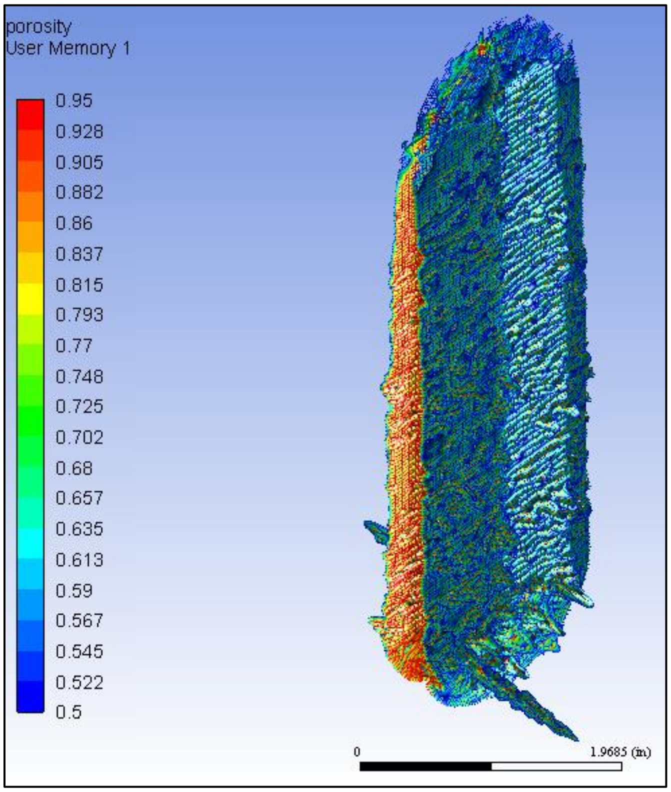

Fig. 3.4 – Acid wormholing of 10 wt% HCl on the fracture-conductivity model.

Fig. 3.5 illustrates the acid etching on the fracture surface for the 10 wt% HCl simulation run on the validation model. It can be observed that the surface etching profile is not as erratic as the acid etching with 15 wt% HCl. Also, the wormholes propagated from the fracture in this case do not extend to the model boundaries as most of the acid was consumed by etching the fracture surface, this dissolution pattern indicates that the acid leakoff in this case was much lower than the previous case due to the lower acid concentration as acid leakoff is a function of acid concentration and formation permeability which is very low in this study (4 md).

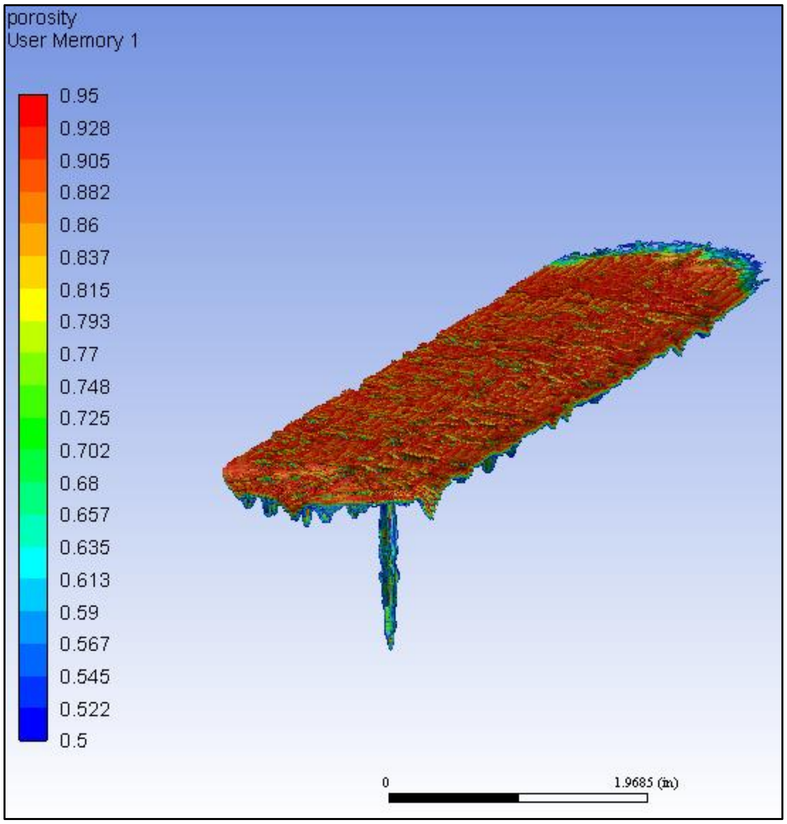

Fig. 3.5 – Etched surface profile caused by 10 wt% HCl on the fracture face in the validation model.

Comparing the results of 10 wt% HCl simulation run with the experimental work, **Fig. 3.6** shows the etched surface profile of 10 wt% HCl on the fracture surface in both modeling and experimental results. Pournik et al. (2013) deduced that the acid etching pattern for gelled HCl shifts from channel etching to roughness etching as the acid is consumed during the dissolution process, and that explains the surface etching profile shown in the figure for the experimental work. As for the modeling, it can be observed that the acid etching of 10 wt% HCl is able to capture this phenomenon and provide similar qualitative trend as the experimental result. Moreover, the average etched width caused by the straight HCl is greater than the etched width generated by gelled HCl. This behavior is common for the straight HCl as the diffusion coefficient of straight HCl is much larger than the diffusion coefficient of gelled HCl due to the high viscosity of gelled HCl that hinders the diffusion process of [H^+] from the bulk to the surface of the fracture.

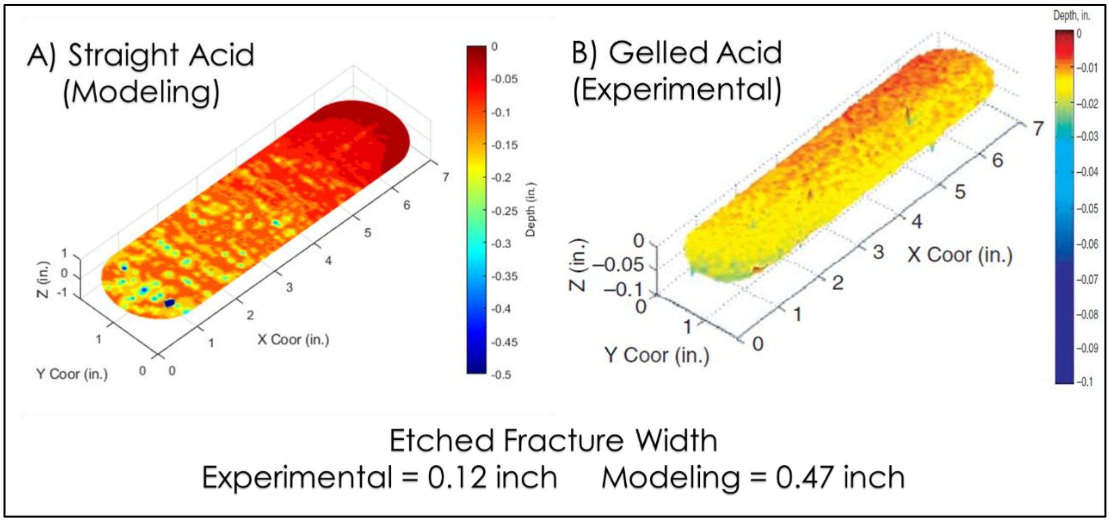

Fig. 3.6 – Acid Etching of 10 wt% HCl on the fracture surface. A) Fracture-conductivity model. B) Experimental results from Pournik et al. 2013. Reprinted with permission from SPE-136217-PA.

As for the 5 wt% HCl case, **Fig. 3.7** illustrates the wormholing phenomenon of 5 wt% HCl simulation run on the validation model. There are no wormholes propagated from the fracture in this case due to the very low acid concentration that was completely consumed in etching the fracture surface without being able to react with the formation to induce the wormholes. Typically, wormholes are induced by the acid leakoff into the formation with a flow direction that is perpendicular to the direction of the flow in the fracture. Moreover, formation permeability plays a key role in controlling acid leakoff into the formation as it will be demonstrated in the subsequent sections.

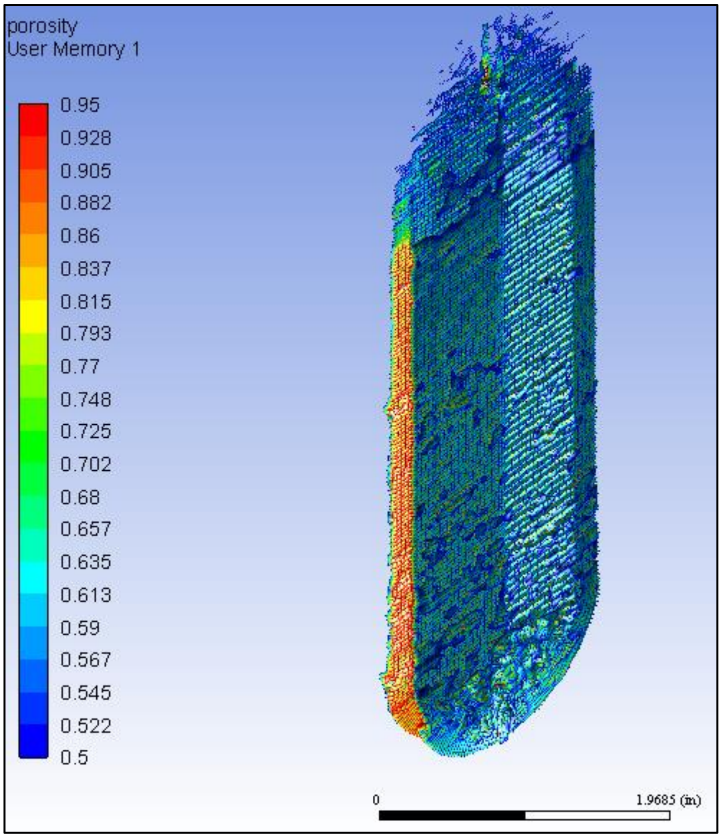

Fig. 3.7 – Acid wormholing of 5 wt% HCl on the fracture-conductivity model.

Fig. 3.8 illustrates the acid etching on the fracture surface for the 5 wt% HCl simulation run on the validation model. The etched surface profile caused by acidizing with 5 wt% HCl did not produce a desirable rough surface, and the surface is almost smooth due to the extremely low reactivity of the acid system. **Fig. 3.9** shows the etched surface profile of 5 wt% HCl on the fracture surface in both modeling and experimental results. The results of the experimental work and the simulation run are aligned together in which the 5 wt% straight HCl and gelled HCl did not etch the fracture surface vigorously to produce rough surface. Also, the average etched width for both cases are matched with insignificant difference between their values.

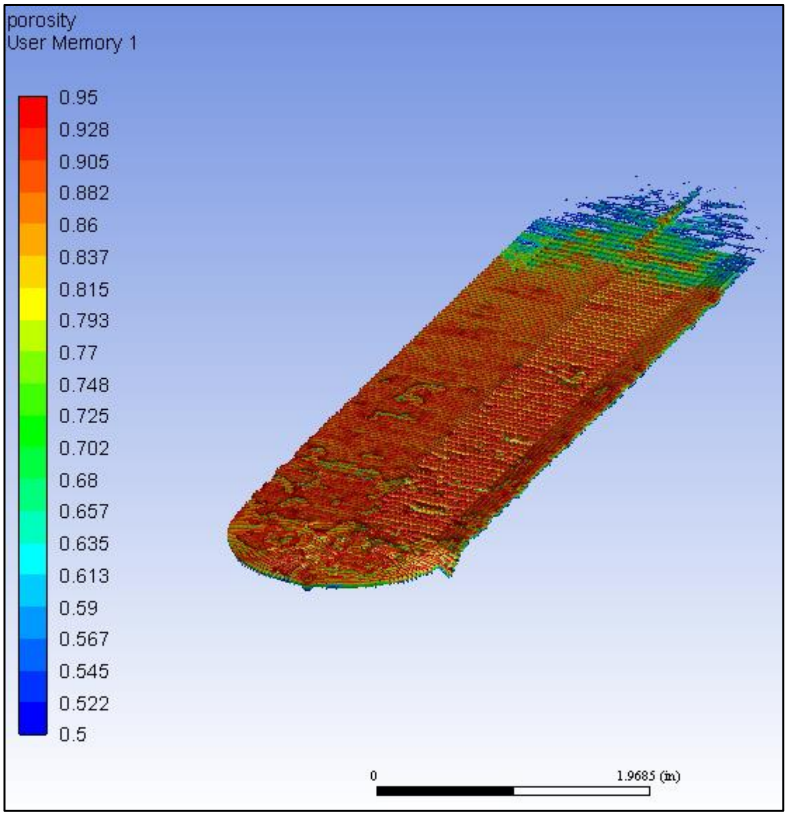

Fig. 3.8 – Etched surface profile caused by 5 wt% HCl on the fracture face in the validation model.

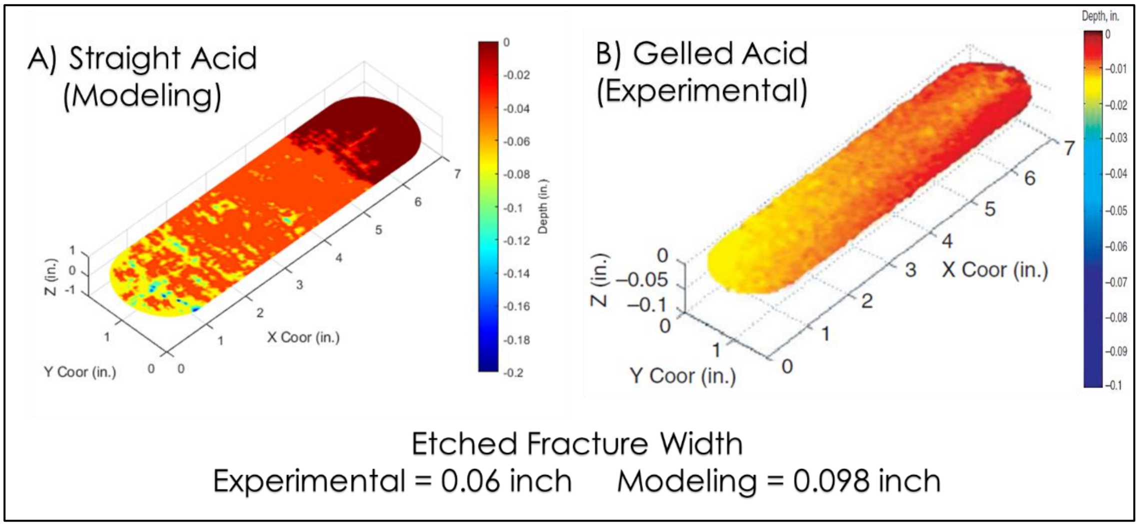

Fig. 3.9 – Acid Etching of 5 wt% HCl on the fracture surface. A) Fracture-conductivity model. B) Experimental results from Pournik et al. 2013. Reprinted with permission from SPE-136217-PA.

It was demonstrated in this study that the two-scale continuum model can capture the etching of the acid to the fracture surface and the womholing phenomenon caused by the leakoff etching of acid into the formation. **Fig. 3.10** summarizes the simulation runs done on the validation model for different acid concentrations. It can be observed that the process of acid etching on the fracture surface becomes less vigorous as the acid concentration decreases. Wormholes that propagated during fracture acidizing are concentrated in the injection inlet area where the acid is reacting with the formation rapidly to induce these wormholes which causes the acid to leakoff into the formation. Wormholing density decreases with the decrease in acid concentration indicating the low reactivity of the acid to etch the fracture surface and induce wormholes.

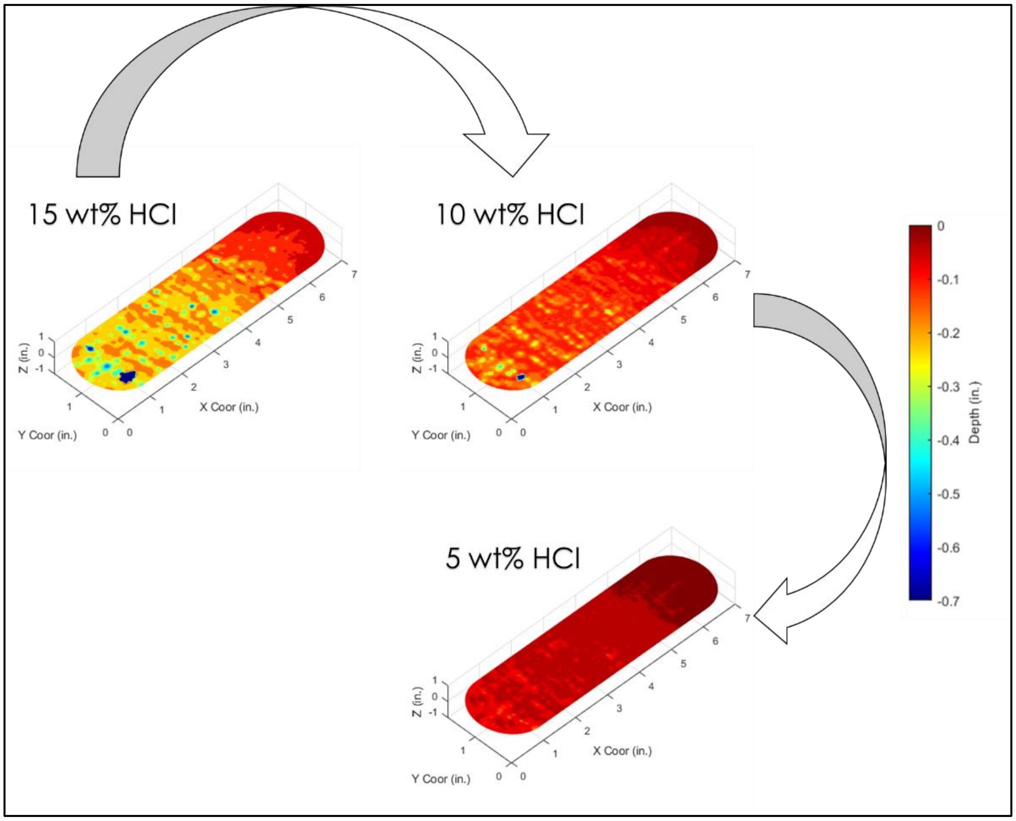

Fig. 3.10 – Summery of the different acid etching patterns with respect to acid concentrations in the validation model.

Fig. 3.11 shows the average etched width caused by fracture acidizing with different acid concentrations. This figure can provide a qualitative relationship between the straight HCl system and the gelled HCl system. Straight HCl system is typically associated with an extensive dissolution of the fracture at the injection inlet area, and that can be supported by the experimental work on fracture-conductivity cell done by Nieto et al. (2008) in which the fracture conductivity experiment was done on Indiana Limestone core sample for 15 wt% HCl at 300°F, and it shows that the fracture-conductivity experiment of straight HCl yields extensive dissolution pattern at the area around the injection inlet with a significant enlargement of etched-fracture width, taking into consideration that the surface profilometer has a limitation of scanning the etched surface in the vertical direction at a range of 0.5 inch.

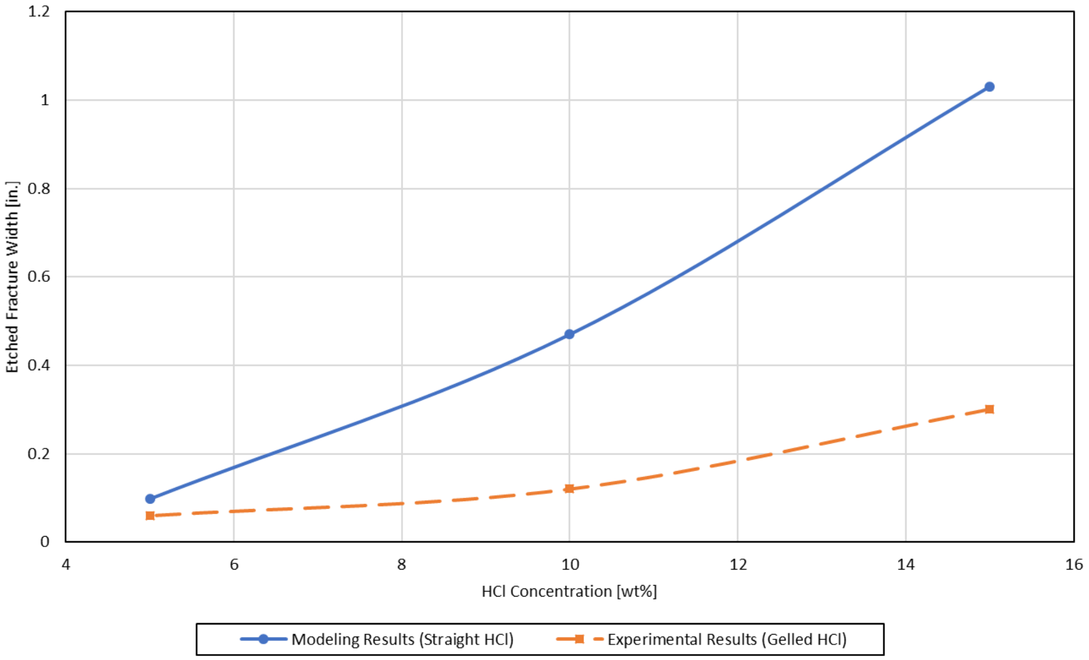

Fig. 3.11 – Average etched width of the fracture surface for different acid concentrations with a comparison between the validation model results and the experimental results (Pournik et al., 2013).

While the 15 wt% straight HCl system reacts rapidly with the fracture surface to produce erratic surface profile by acid roughness etching, the 15 wt% gelled HCl used in the experiment induces lower average etched profile than the straight HCl system because of the channel etching mechanism of gelled acid, and that explains the significant difference in the etched width between the two acid systems. Decreasing acid concentration causes a total reduction in acid etching on fracture surface, and that is noticeable in **Fig. 3.11** due to the low concentration of [H^+] species dispersed in the aqueous solution that is responsible for the low reactivity of the acid system. At the lowest acid concentration of 5 wt% HCl, the average etched width of both acid systems is matched with very small difference between the values, and that is aligned with the common observation of any acid system with very low acid concentration using in acid fracturing stimulation. Overall, the straight HCl system tends to produce a vigorous and more erratic etched fracture surface than any of the retarded acid systems, and this phenomenon has been captured successfully using the developed model that adapt the two-scale continuum model with Navier-Stokes formulation.

4. CLOSED-FRACTURE ACIDING IN CALCITE FORMATION

In this section, closed-fracture acidizing was studied thoroughly in calcite formation using the model shown in **Fig. 2.8** and the simulation parameters demonstrated in **Table 2.3**. Acid is injected in the closed-fracture at injection rates shown in **Table 4.1**. Field injection rates were obtained by assuming a fracture geometry of 0.5 in. aperture and a wellbore radius of 0.3 ft, then multiplying the injection velocity with the injection area of the fracture to obtain the field injection rate. This actual fracture geometry was used to upscale the numbers used in the model and be able to relate with a real CFA operation in the field. Since the model used in this study has a tremendous number of grid blocks, the model was run for an injection period of 10 minutes which considers an average time period for a conventional CFA operation.

Table 4.1 – Acid injection rates used in the CFA-Calcite model.

Injection Velocity (m/s)	**Field Injection Rate (GPM)**	**Total Injection Volume (Gallons)**
0.0045	12.09	120.9
0.008	21.50	215
0.045	120.90	1209

A parametric study of several parameters was conducted and covered in this section including the effect of injection rates, acid concentration, fracture conductivity, and temperature. Then, an analysis of dimensionless parameters was conducted to comprehend and understand the dissolution process during CFA operation and the wormholing phenomenon associated with it.

4.1. Effect of Acid Concentration

Hydrochloric Acid was injected in the closed-fracture with concentrations of 15, 20, and 28 wt% at a temperature of 150°F. The imposed fracture in the model has a conductivity of 7000 md-ft calculated from **Eq. 1.1** and **Eq. 2.14**. This high fracture conductivity value was used in this section to study the effect of acid concentration solely on the CFA process without the interruption of flow impedance from the acid fracture conductivity. **Fig. 4.1** shows the results of the simulation runs of CFA-Calcite model for different acid injection rates and acid concentrations for an injection time of 10 minutes. The figure demonstrates different dissolution pattern for different cases. At injection rates 12.09 and 21.5, the acid is flowing dominantly in the fracture without enough momentum to leakoff and flow into the formation. This dissolution phenomenon suggests a face dissolution on the fracture morphology without inducing dominant wormholes that propagate from the fracture. At an injection rate of 120.9 GPM, the flow rate was very high which provides the acid with enough momentum to percolate into the formation and react with the formation to create wormholes. In the case of high flow rate, the flow in the formation competes with the flow in the fracture which allows the acid to leakoff into the formation and reach the breakthrough state, in which the acid reaches the side boundaries of the model. Because of the accelerated reaction rate between HCl and calcite, the acid did not expand the width of the fracture in the case of 120.9 GPM injection rate as the acid was able to flow into the formation and react with it, unlike the case of lower injection rates where the acid was reacting mainly with the fracture. At 28 wt% HCl, the acid was reacting rapidly with the formation in which it creates wormholes around the area of the injection inlet even for the cases of lower injection rates. This dissolution behavior indicates that the acid was highly reactive in a way that allows the acid to leakoff into the formation, especially around the vicinity of the injection inlet.

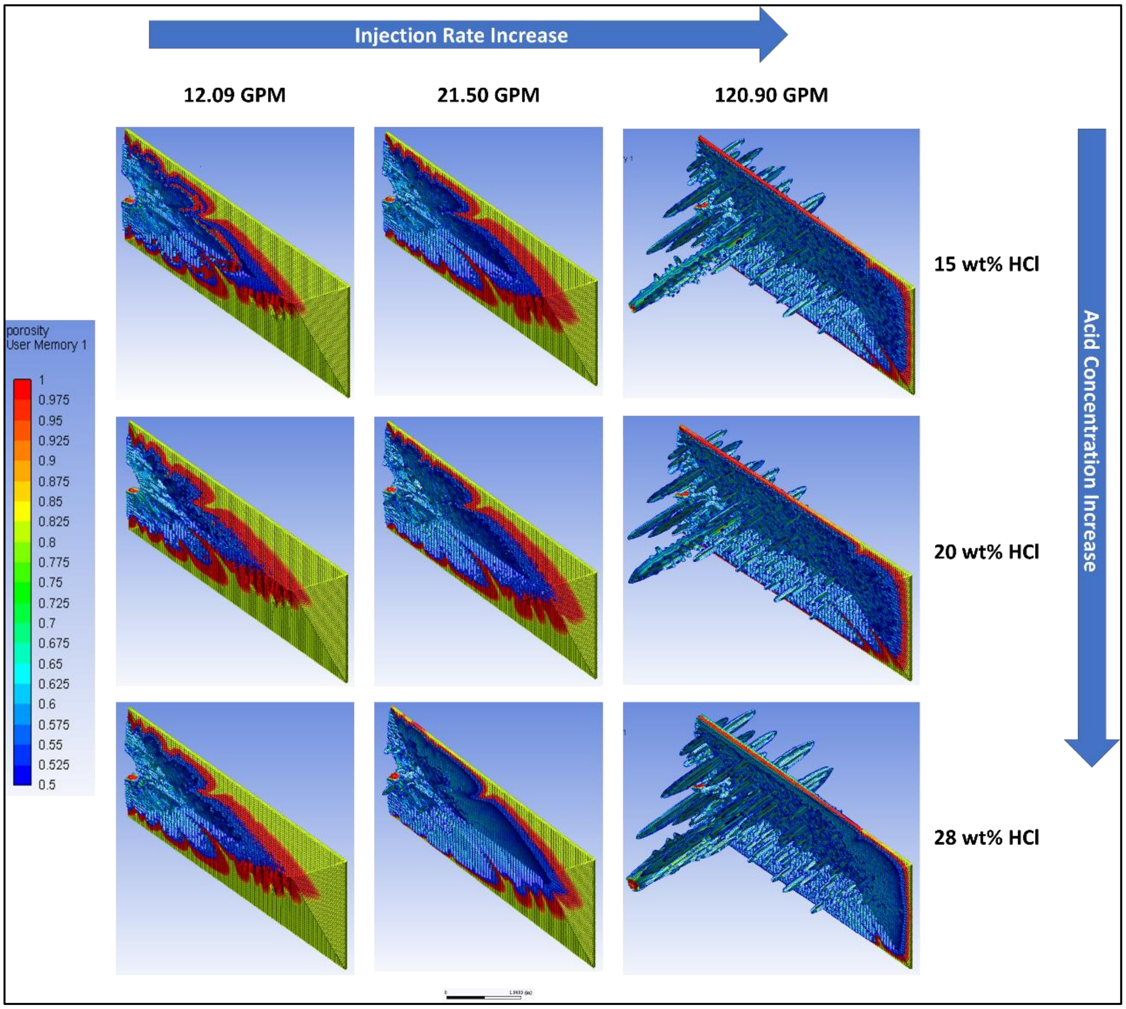

Fig. 4.1 – Dissolution pattern and wormholes propagation in CFA-Calcite model for different acid injection rates and acid concentrations with a fracture conductivity of 7000 md-ft at 150°F.

The dissolution phenomenon of HCl-calcite system can be assessed thoroughly by investigating the acid concentration profile in the fracture. **Fig. 4.2** shows the acid concentration profile of the fracture with a conductivity of 7000 md-ft for different acid concentration and injection rates. At injection rates of 12.09 and 21.50 GPM, the acid concentration profile exhibit smooth gradient which indicates the acid dissolution of the closed-fracture and the acid is reacting mainly with the fracture without leaking into the formation. At an injection rate of 120.9 GPM, the acid concentration profile in the fracture shows sharp gradients which indicate the existence of live acid inside the fracture because of the large volume injected during the injection period of the acid in the closed-fracture. This behavior demonstrates the existence of the wormholes that allow the acid to leakoff into the formation leaving some area in the fracture unstimulated, especially in the case of 28 wt% HCl. Sharp gradient in acid concentration profile in the fracture can be observed as well in the case of 28 wt% HCl, this distinguishable decline in the acid concentration indicates that the acid is reacting rapidly with the formation at the moment of acid-formation contact which induces wormholes that propagate from the fracture allowing the acid to flow into them prior to acid flow into the fracture.

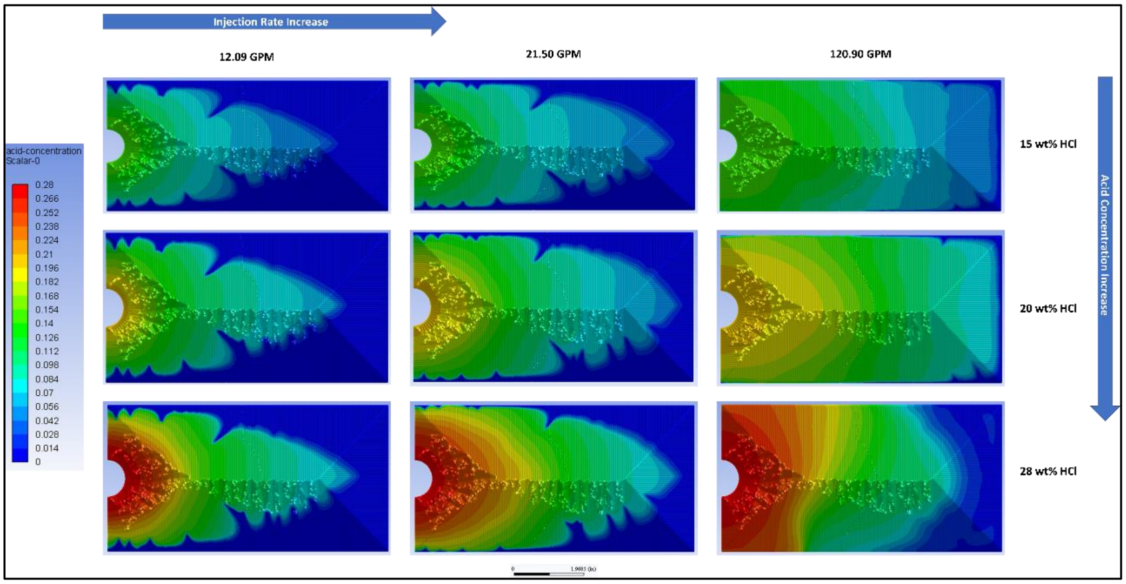

Fig. 4.2 – Acid concentration profile of the fracture in CFA-Calcite model with a fracture conductivity of 7000 md-ft at 150°F.

It can be observed that this decline pattern is associated with the wormholes propagated during the acid dissolution of the closed-fracture. This phenomenon can be explained by the rapid reaction rate between the HCl-calcite system that allows the acid to react instantaneously during the injection of the acid in the fracture. Wormholing phenomenon in the demonstrated cases indicates that the acid induces wormholes that propagate from the fracture in the cases of high injection rates and/or high acid concentrations.

4.2. Effect of Fracture Conductivity

In the previous section, a highly conductive fracture was imposed in the model to study the effect of acid concentration on the closed-fracture acidizing process. In This section, A fracture with low conductivity of 275 md-ft was imposed in the model using **Eq. 1.1** and **Eq. 2.14**, and a comparison is made between the results of high-conductivity fracture and low-conductivity fracture with acid injection duration of 10 minutes at 150°F.

For the low-conductivity fracture, simulation runs of CFA-Calcite model includes the injection of straight HCl with concentrations of 15 and 28 wt%. **Fig. 4.3** shows the results of the simulation runs done on the CFA-Calcite model with low-conductivity fracture for different injection rates and acid concentrations. Unlike the previous case of the high-conductivity fracture, there are wormholes that propagated from the fracture at injection rates of 12.09 and 21.5 GPM of both 15 and 28 wt% acid concentrations. This wormholing phenomenon indicates that an early acid leakoff into the formation occurred at the start of the injection which is a sign that the flow into the formation competes with the flow in the fracture due to the low fracture conductivity. In this case, wormholes initiated during the acid leakoff into the formation, and the acid contributed to grow these wormholes instead of flowing into the fracture which leaves significant unstimulated area in the fracture. At acid injection rate of 120.9 GPM, it can be observed that the acid has reached the state of breakthrough, and there is a single dominant wormhole that propagate from the fracture that allows the acid to flow into the formation and to reach the boundaries of the model. It can also be observed that the acid did not stimulate the whole fracture although the injection rate was highly enough to provide the acid with the required momentum, this is due to the initiated wormholes that was created from the beginning of CFA process allowing the acid to flow into the formation readily.

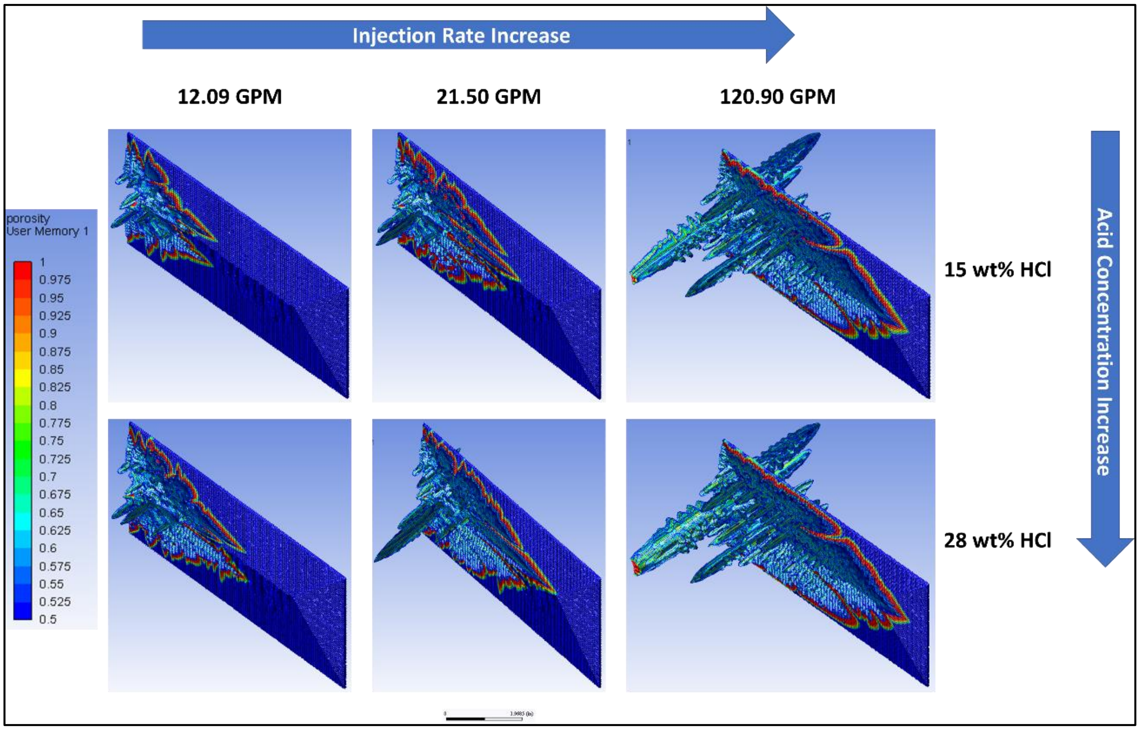

Fig. 4.3 – Dissolution pattern and wormholes propagation in CFA-Calcite model for different acid injection rates and acid concentrations with a fracture conductivity of 275 md-ft at 150°F.

The previous results can be supported further by investigating the acid concentration profile in the fracture. **Fig. 4.4** shows the acid concentration profile of the fracture with a conductivity of 275 md-ft for different acid concentration and injection rates. The results differ significantly from the results of 7000 md-ft fracture conductivity. At 15 wt% HCl concentration, it can be observed that the acid is not reacting with the fracture due to the existence of live inside the fracture at injection rates of 12.09 and 21.5 GPM as shown in the figure, this is due to the acid leakoff into the formation at the beginning of CFA operation. At 28 wt% HCl concentration, a sharp acid concentration gradient can be observed at injection rates of 12.09 and 21.5 GPM in the closed-fracture indicating significant acid leakoff into the formation as discussed previously. High acid concentration in the case of lower injection rates has contributed in the acid flow in the fracture, and that the 28 wt% acid concentration displaced the acid even further in the fracture than the 15 wt% acid concentration as the acid was more reactive than the previous case. At an injection rate of 120.9 GPM, the acid already reached the state of breakthrough at the early stage of acid injection in the closed-fracture, this can be indicated from the sharp gradient in the acid concentration profile with the acid is intensively concentrated at the injection inlet area. From the simulation results of 120.9 GPM injection rate, the time required for the acid to breakthrough and reach the boundaries of the model in the case of 7000 md-ft fracture conductivity is 3 minutes for 15 wt% HCl and 2.2 minutes for 28 wt% HCl, while the time required for the acid to breakthrough in the case of 275 md-ft fracture conductivity is 2.6 minutes for 15 wt% HCl and 1.7 minutes for 28 wt% HCl. Identifying the flowing time of acid to reach the breakthrough state in the model can yield significant information on the dissolution process of the acid to the fracture during CFA operation.

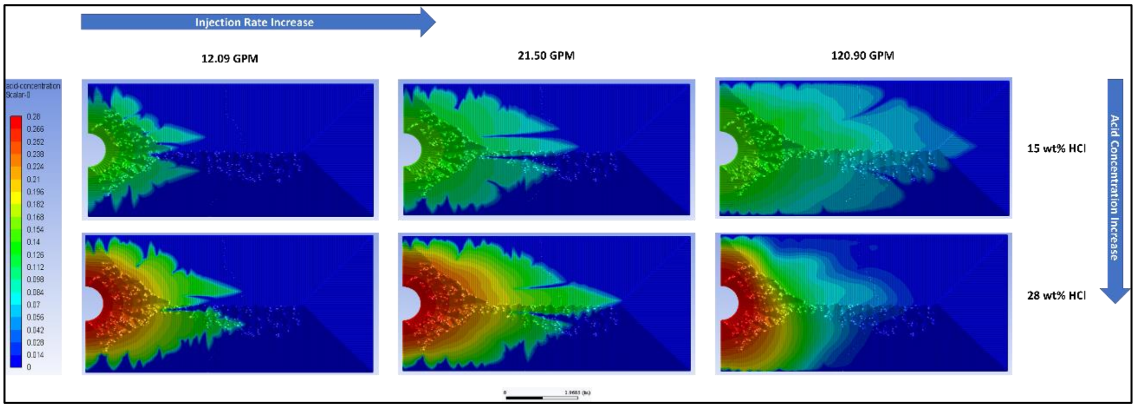

Fig. 4.4 – Acid concentration profile of the fracture in CFA-Calcite model with a fracture conductivity of 275 md-ft at 150°F.

To further understand the wormholing phenomenon during CFA operation, the total acid volume injected to breakthrough in the CFA-Calcite model is plotted versus acid concentrations for fracture conductivities of 7000 and 275 md-ft as shown in **Fig. 4.5**. It can be observed from the plot that larger acid volumes required for the acid to breakthrough in the model for the case of high fracture conductivity and low acid concentration, since the fracture in this case is the dominant conduit in the domain for the flow of acid in the model, and the acid is reacting predominantly with the fracture which will be consumed in that process because of the low acid concentration to begin with. As the acid concentration increase and/or fracture conductivity decrease, acid will get more opportunity to leak into the formation either due to the reactivity of the acid system because of its high concentration or due to the competition in the acid flow in the domain between the flow in the formation or the flow in the low-conductivity fracture. This phenomenon leads to low acid volumes required for the acid to breakthrough and reach the boundaries of the model. It can be observed from the plot that there is insignificant difference between the results of the two fracture conductivities in term of the total required acid volumes to breakthrough. This behavior is due to the high reaction rate of HCl-calcite system which allows the acid to react rapidly with the formation and induce wormholes that contribute to the flow of acid into the formation.

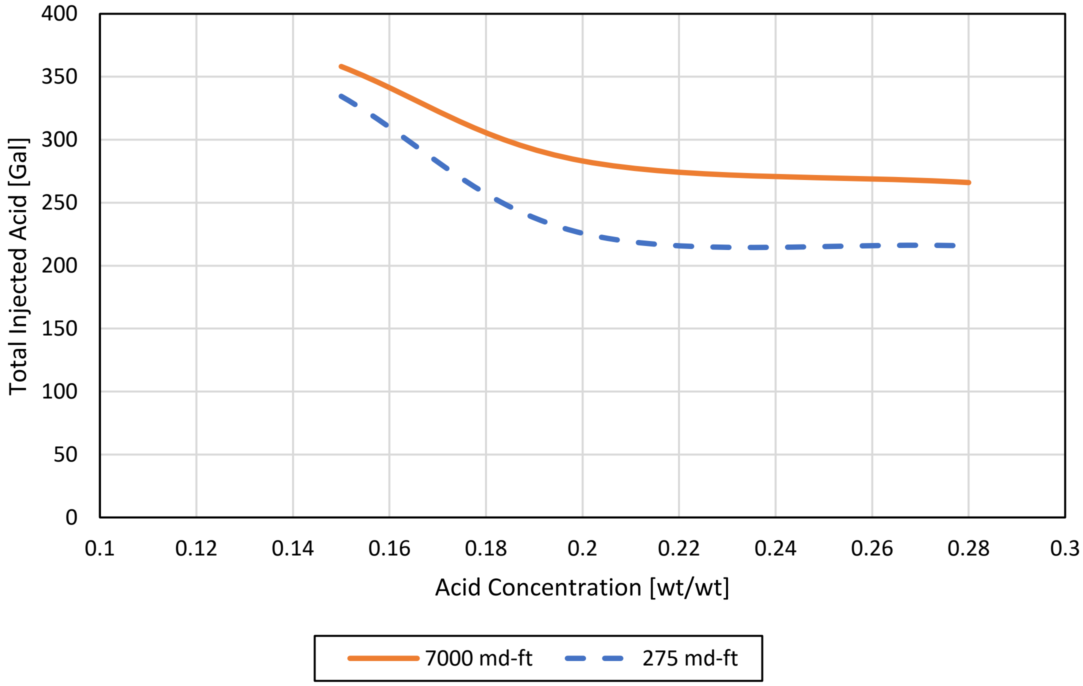

Fig. 4.5 – Total acid volume injected to breakthrough in CFA-Calcite model for different acid concentrations and fracture conductivities at an injection rate of 120.90 GPM and a temperature of 150°F.

4.3. Effect of Formation Temperature

The study that was conducted so far in the previous sections covers the parametric effects on CFA operation at a formation temperature of 150°F. The simulation parameters in CFA-Calcite model is modified with the temperature-related parameters demonstrated in **Table 2.5** to study the effect of temperature on CFA operation at 100°F and 200 °F.

Formation temperature has a direct effect on the simulation parameters used in the two-scale continuum model. Temperature increase in the medium leads to an increase in acid diffusivity and reaction rate constant of the acid-rock system, and it leads to a decrease in acid density and acid viscosity. **Fig. 4.6** shows the results of the simulation runs done on the CFA-Calcite model with 15 wt% HCl concentration and low-conductivity fracture for different injection rates and formation temperatures. It can be observed that temperature has a significant impact on the dissolution pattern and wormholing phenomenon of the acid during CFA operation. At a temperature of 100°F, a smooth dissolution pattern is associated with the acid front in the fracture along with a significant number of wormholes propagated during the dissolution process, this phenomenon is due to the low acid diffusivity and surface reaction rate associated with 100°F temperature that allows the acid to leak into the formation first, and then it starts to react with the fracture and the formation inducing wormholes. As temperature increases in the medium, the dissolution pattern associated with the acid front becomes sharper and pointy indicating rapid dissolution during acid injection. It can also be observed that the number of wormholes propagated from the fracture decreases with the increase in temperature which indicates the rapid acid consumption during the acid flow into the formation. Since the fracture conductivity in this study is low which promotes acid leakoff into the formation, the increase in temperature tends to accelerate the reaction in the HCl-calcite system which constrains the acid from flowing into the formation, and let it be consumed predominantly in the fracture at the start of acid injection which displaces the acid even further during the acid flow in the fracture. This phenomenon can be observed by investigating the simulation results at 200°F temperature in the elaborated figure.

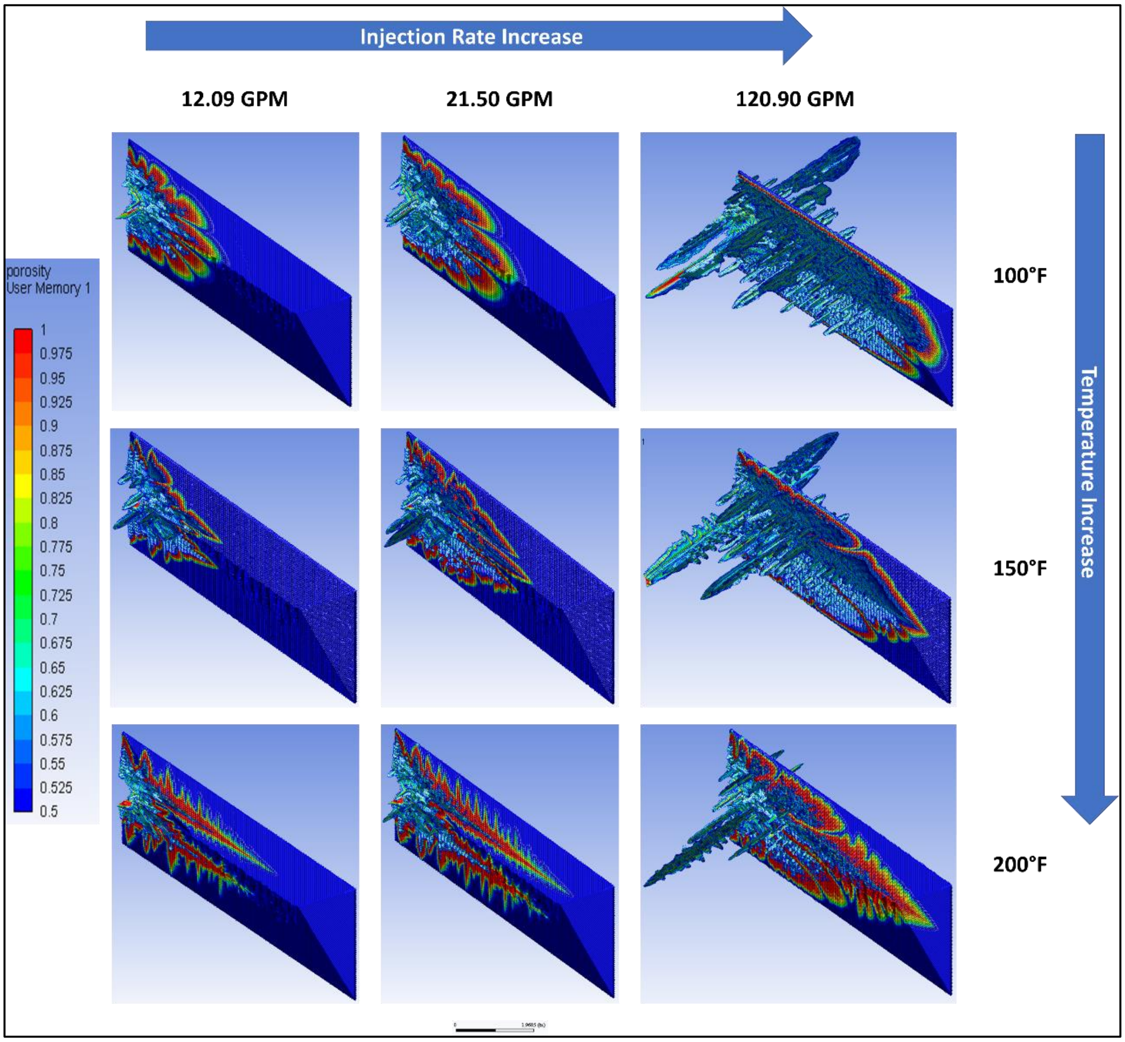

Fig. 4.6 – Dissolution pattern and wormholes propagation of 15 wt% HCl in CFA-Calcite model for different acid injection rates and formation temperatures with a fracture conductivity of 275 md-ft.

To further asses the dissolution process of the acid in the CFA-Calcite model, Fig. 4.7 shows the acid concentration profile of the fracture after injecting 15 wt% HCl for 10 minutes in the CFA-calcite model with low fracture conductivity and different formation temperatures. At a temperature of 100°F, the gradient of acid concentration profile in the fracture is smooth indicating decelerated dissolution of acid during the CFA process. As temperature increases in the domain, the acid concentration profile in the fracture exhibits sharp gradients with rapid decline in the value of acid concentration indicating rapid reaction and dissolution during the acid injection process. It can be observed that sharp and pointy patterns are associated with the acid front in the fracture as temperature increases in the medium. An important point to highlight is that the wormholing density in the fracture decreases with the temperature increase in the domain, this phenomenon can be observed at temperatures of 150°F and 200°F in the red-colored area concentrated around the vicinity of the injection inlet. Acid leakoff takes place regardless of formation temperature as discussed previously. However, temperature enhances the process of wormholes creation by the accelerated reaction between the acid and the formation.

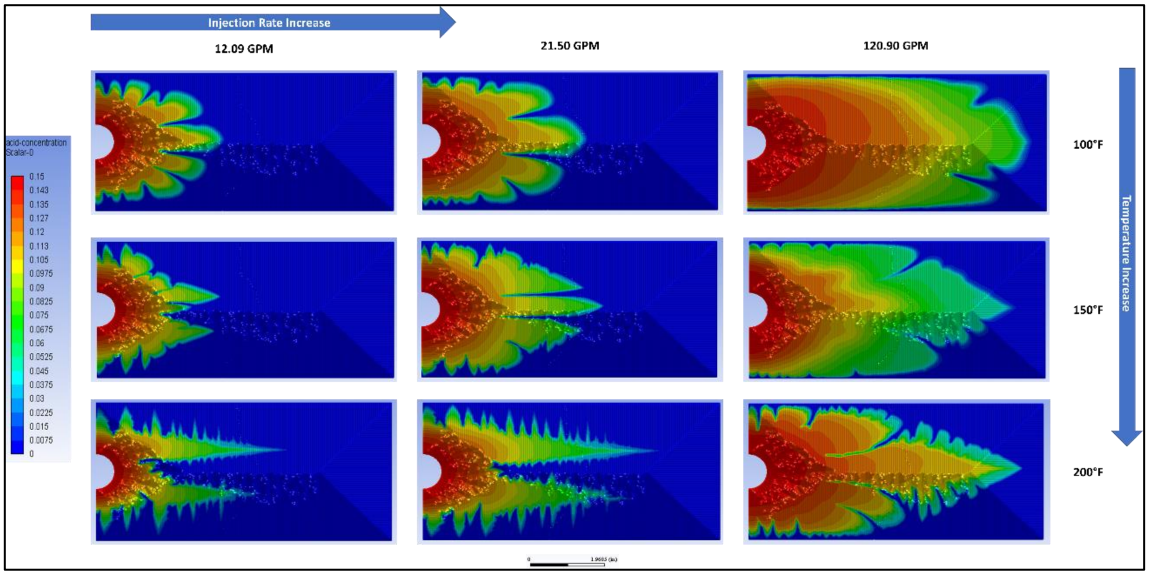

Fig. 4.7 – Acid concentration profile of the fracture after injecting 15 wt% HCl for 10 minutes in CFA-Calcite model with a fracture conductivity of 275 md-ft at different formation temperatures.

At an injection rate of 120.9 GPM, the acid reached the side-boundaries of the model which indicates the breakthrough of acid as a sign of dominant flow of acid in the wormholes prior to the fracture. The time required for the acid to reach the state of breakthrough decreases with the increase in temperature, as the durations required for acid breakthrough in the model are 5.75 minutes for a temperature of 100°F, 2.6 minutes for a temperature of 150°F, and 1.4 minutes for a temperature of 200°F at an injection rate of 120.9 GPM. This phenomenon is due to the decrease in wormholing density as the temperature increases in the domain. Wormholing density is a function of acid concentration, fracture conductivity and temperature, this can be proved by plotting the total injected volume of acid to breakthrough in the model with different formation temperatures as illustrated in **Fig. 4.8**. For a temperature of 100°F, acid leakoff takes place from the virtue of low fracture conductivity, but the wormholes propagated as a result of acid leakoff will take some time to be generated depending of acid diffusivity and reaction rate constant of the system. In the case of low temperature, the acid will leak into the formation generating multiple wormholes as a result of the decelerated reaction rate due to the low temperature. As temperature increases, acid diffusivity and the reaction rate constant will increase and accelerate the acid dissolution in the model at the start of acid injection. This dissolution process will lead to a smaller number of wormholes generated, and the acid will grow these few wormholes to be propagated from the fracture until they reach the boundaries of the model which will result in less total acid volume injected to breakthrough as demonstrated in the figure. This conclusion related to wormholing density associated with the acid dissolution in the closed-fracture is based on a steady state temperature model which assumes no transient heat transfer process occurring in the model and ignoring the effect of the generated heat from the reaction of HCl-calcite system.

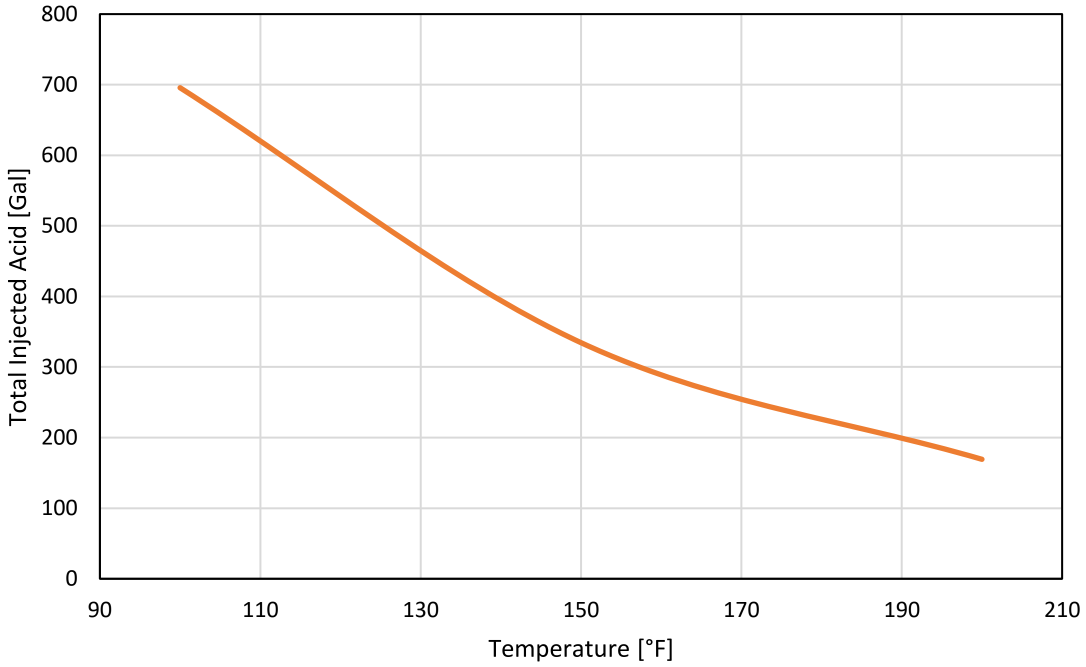

Fig. 4.8 – Total acid volume injected to breakthrough for 15 wt% HCl in CFA-Calcite model for different temperatures and a fracture conductivities of 275 md-ft at an injection rate of 120.90 GPM.

4.4. Analysis of Dimensionless Parameters

The analysis of dimensionless quantities is important in identifying the mechanisms of acid dissolution and the reaction regime governing the wormholing phenomenon during CFA operation. Three dimensionless parameters were covered in this study that demonstrate the coupling between the flow mechanics of the acid and its reactivity with the medium, these dimensionless numbers are Peclet number, kinetic number, and Damköhler number. Peclet number is the ratio of the convective mass transport rate to the diffusive mass transport rate of the acid species. In acid fracturing, Peclet number is defined in **Eq. 4.1** as described in designing acid fracturing jobs made by Williams and Nierode (1972).

$$N_{Pe} = \frac{v_L w}{2D} \qquad \text{.......4.1)}$$

Where N_{Pe} is leakoff Peclet number, and v_L is leakoff velocity. Peclet number characterizes the acid leakoff velocity during the acid flow in the fracture. At low values of Peclet number, the dominant acid transport mechanism is the diffusive mass transport and the acid concentration decreases rapidly during the acid flow in the fracture. At high values of Peclet number, the dominant acid transport mechanism is the convective mass transport and the acid concentration is conserved to penetrate deeper in the fracture. Acid leakoff velocity can be obtained from the simulation runs of CFA-Calcite model as the perpendicular component of the injection velocity vector which is transversal to the direction of the fracture.

Kinetic number is the ratio of acid-rock reaction rate to the acid diffusion rate (Buijse, 2000). It is defined in **Eq. 4.2** as,

$$N_{ki} = \frac{r_w k_s {C_0}^{n-1}}{D} \qquad \text{.......4.2)}$$

Where N_{ki} is the kinetic number, r_w is the wormhole radius, and C_0 is the acid concentration at wormhole entrance. Kinetic number can also be called wormholing efficiency number. At high values of kinetic number, the acid spending rate is diffusion-controlled that is defined as the reaction regime in which the reaction rate is much higher and faster than the acid diffusivity in the medium, this reaction regime results in deeper wormhole penetration into the formation due to acid leakoff during CFA process. At low values of kinetic number, the acid spending rate is reaction-controlled that is defined as the reaction regime in which the reaction rate of acid-rock system is much lower and slower than the acid diffusivity, and the overall acid spending rate is controlled by the reaction kinetics (Buijse, 2000). A diffusion-controlled regime is the main drive for acid leakoff into the formation to take place, and it is essential for wormholing to occur during the CFA process. Calcite formation exhibits a very high acid-rock reaction rate and so, it is characterized by diffusion-controlled regime. Wormhole radius can be obtained from the simulation runs of CFA-Calcite model as shown in **Fig. 4.1**, **Fig. 4.3**, and **Fig. 4.6**, and initial acid concentration at wormhole entrance can be obtained from the acid concentration profiles in the fracture as shown in **Fig. 4.2**, **Fig. 4.4**, and **Fig. 4.7**.

The acid reaction with the rock is called mass transport limited when the reaction rate of acid-rock system is relatively higher that the acid mass transfer rate. On the other hand, the reaction is called reaction rate limited when the acid mass transfer rate is relatively higher than the reaction rate of acid-rock system. For mass transport limited reaction in the case of HCl-calcite system, Damköhler number is the ratio of the reaction rate that is characterized by the diffusion coefficient for a mass transport limited reaction and the rate of reactant transport by convection (Hoefner and Fogler, 1989). Damköhler number is defined in **Eq. 4.3** as (Buijse, 2000),

$$N_{Da} = \frac{N_{ki}}{N_{Pe}} \qquad (4.3)$$

Where N_{Da} is the Damköhler number. This description of Damköhler number includes both Peclet number and kinetic number formulations which can be used to describe the acid flow and reaction regime during the CFA operation. At high values of

Damköhler number, live acid will penetrate deeper in the fracture before being consumed resulting in steep acid concentration profile. At low values of Damköhler number, the acid concentration profile in the fracture will exhibit sharp front due to very rapid acid spending at the tip of acid dissolution front in the fracture, and this acid spending phenomenon will be associated with significant leakoff of acid into the formation due to inability of the acid to penetrate deeper in the fracture during acid injection in the closed-fracture.

Given all the parameters that are used or obtained from the simulation runs of CFA-Calcite model, the three dimensional quantities can be calculated for different injection rates, acid concentrations, fracture conductivities, and formation temperatures. **Fig. 4.9** shows Peclet numbers obtained from the simulation runs of CFA-Calcite model for different acid injection rates, acid concentrations, and fracture conductivities. It can be observed that Peclet number increases with the increase in the acid injection rate due to the increase in the associated acid leakoff velocity. Peclet numbers for high acid concentrations is always higher than the Peclet numbers for low acid concentrations at the same fracture conductivity due to the accelerated acid leakoff process into the formation caused by the reactivity of the acid with high concentrations. Low-conductivity fracture exhibits higher Peclet numbers than high-conductivity fracture, since the fracture with low-conductivity promotes high acid leakoff into the formation, and hence the acid induces wormholes due to acid leakoff which can compete with the acid flow in the fracture at certain wormholing density in the medium. It can be observed that at higher values of Peclet numbers, acid can penetrate deeper into the fracture giving that a high fracture conductivity is required with low acid concentration as discussed previously.

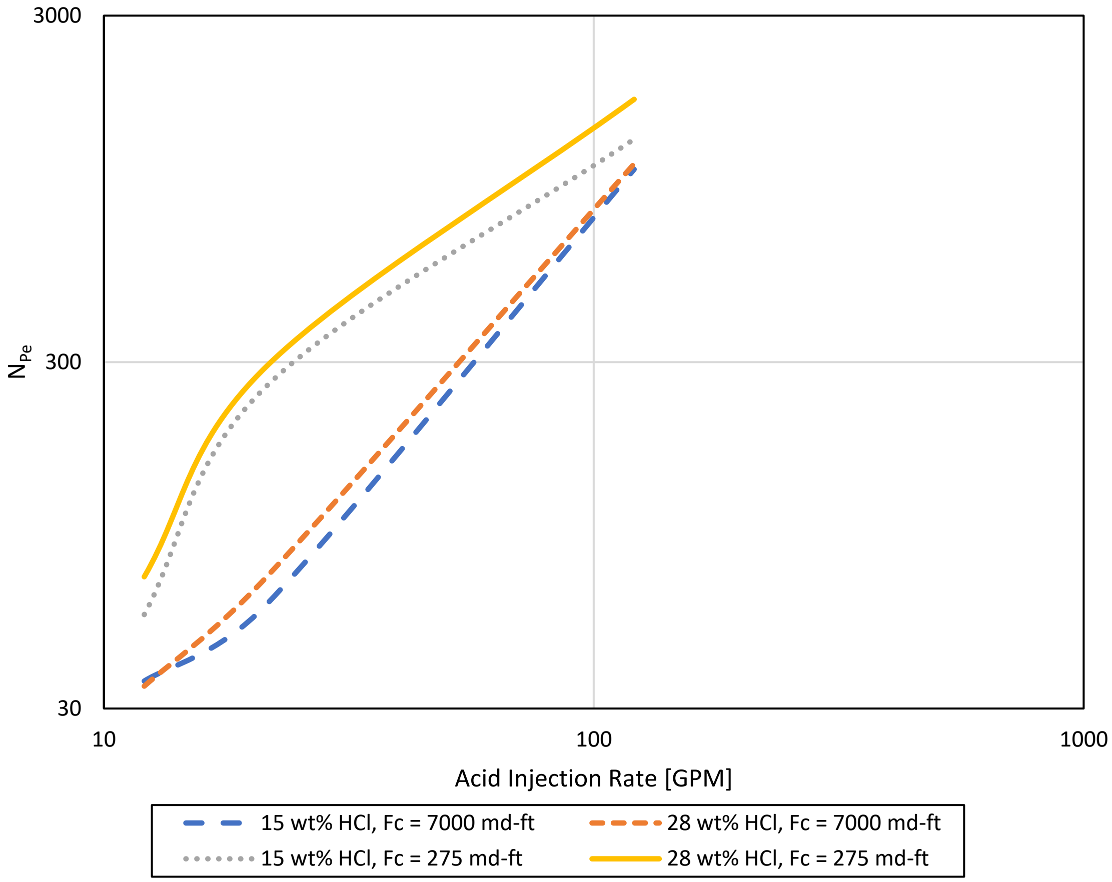

Fig. 4.9 – Peclet number for different acid injection rates, acid concentrations, and fracture conductivities in the CFA-Calcite model.

To assess the wormholing phenomenon associated with the CFA process, Damköhler number should be investigated. **Fig. 4.10** shows Damköhler numbers obtained from the simulation runs of CFA-Calcite model for different acid injection rates, acid concentrations, and fracture conductivities. Generally, Damköhler number is low for very high acid injection rate due to the high acid leakoff velocity, it also indicates that the dissolution process of the fracture is governed by the convective forces of the acid which leads a sharp gradient in acid concentration profile as demonstrated previously. High acid concentrations exhibit lower Damköhler numbers than low acid concentration for the same fracture conductivity due to the increase in acid leakoff into the formation caused by the rapid reaction between the acid system and the formation that induces deep wormholes propagated from the fracture. For low-conductivity fracture, a peak point exists at the range of intermediate acid injection rates. This point indicates an intensive wormhole growth around the vicinity of the injection inlet characterized by high Damköhler number with relatively low acid injection rate which allows the acid to flow easily into the formation to grow the propagated dominant wormhole due the low conductive fracture in the medium. At high-conductivity fracture, Damköhler number exhibits straight-line decline with respect to acid injection rate because of the nonexistence of dominant and deep wormhole that allows the acid to flow into the formation in which the acid spending occurs at the fracture surfaces giving that the acid has low concentration. It can be concluded that injecting the acid at low rates for CFA operations might not be the wisest choice because of the acid leakoff that occurs at high Damköhler number due to the initiation of dominant and deep wormholes around the area of injection inlet that promote extensive acid flow into the formation leaving significant area of the fracture unstimulated, especially in the low conductive fracture. Also, it is not recommended to inject the acid at high rates because of surface smoothing phenomenon that promotes the acid to dissolve the asperities that hold the fracture open and create the required fracture conductivity. The results shown in this section coincide with the results demonstrated in the previous section. The cases that have high values of Damköhler number such as low acid concentration, low injection rate, and high fracture conductivity exhibit smooth acid concentration profile in the fracture with deeper acid traveling distance. While The cases that have low values of

Damköhler number such as high acid concentration and low fracture conductivity exhibit sharp acid concentration profile in the fracture with acid consumption close to the injection inlet area that is associated with deeper wormholes propagated from the fracture.

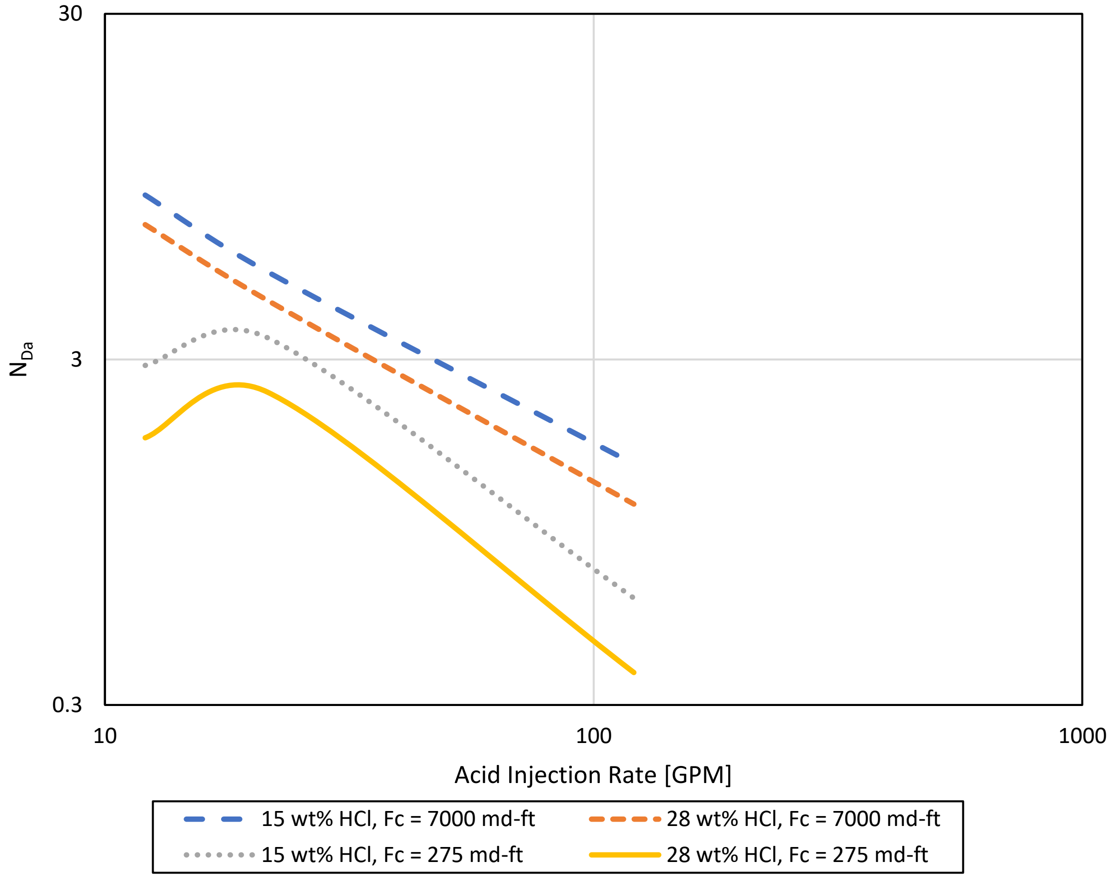

Fig. 4.10 – Damköhler number for different acid injection rates, acid concentrations, and fracture conductivities in the CFA-Calcite model.

Formation temperature has a great impact om the parameters related to acid dissolution and reaction mechanism such as acid diffusivity and reaction rate of acid-rock system. **Fig. 4.11** shows the results of Peclet number obtained from the simulation runs of 15 wt% HCl in CFA-Calcite model at different formation temperatures and a fracture conductivity of 275 md-ft. It can be observed that Peclet number decreases with the increase in formation temperature. Temperature increase in the medium leads to an increase in acid diffusivity, and hence Peclet number decreases. This effect is coupled with the increase in acid leakoff due to the increase in the total acid injection rate during CFA process. It is worth to mention that the increase in temperature changed the dissolution regime of the acid-rock system. At a temperature of 200°F, the diffusion coefficient increases significantly as demonstrated in **Table 2.5**, and hence Peclet number decreases the dissolution regime changed from diffusion-controlled reaction regime to reaction-controlled regime in which acid leakoff occurs regardless of acid injection rate due to the rapid reaction that takes place during acid injection.

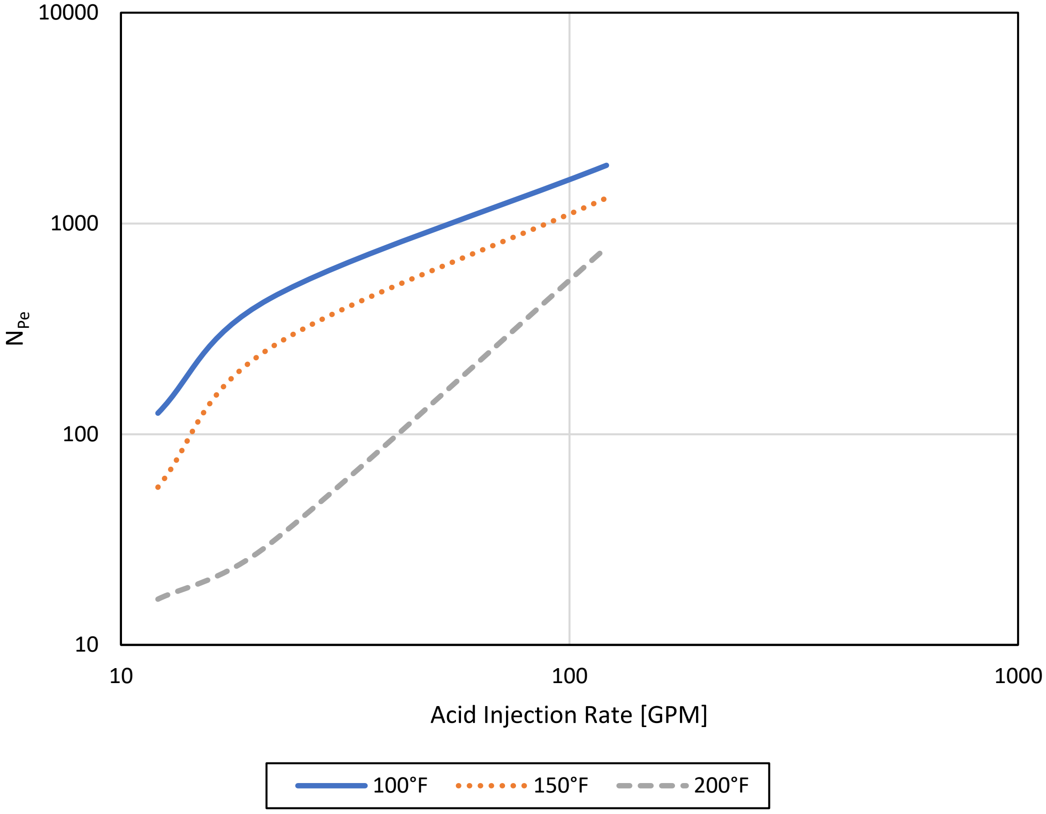

Fig. 4.11 – Peclet number of 15 wt% HCl injected at different rates in the CFA-Calcite model with different formation temperatures and a fracture conductivity of 275 md-ft.

This can be observed through the change in slope line between the Peclet number of 200°F and the Peclet number of other temperatures. To ascertain the wormholing phenomenon associated with CFA operation at different formation temperatures, Damköhler number is investigated. **Fig. 4.12** shows the results of Damköhler number obtained from the simulation runs of 15 wt% HCl in CFA-Calcite model at different formation temperatures and a fracture conductivity of 275 md-ft.

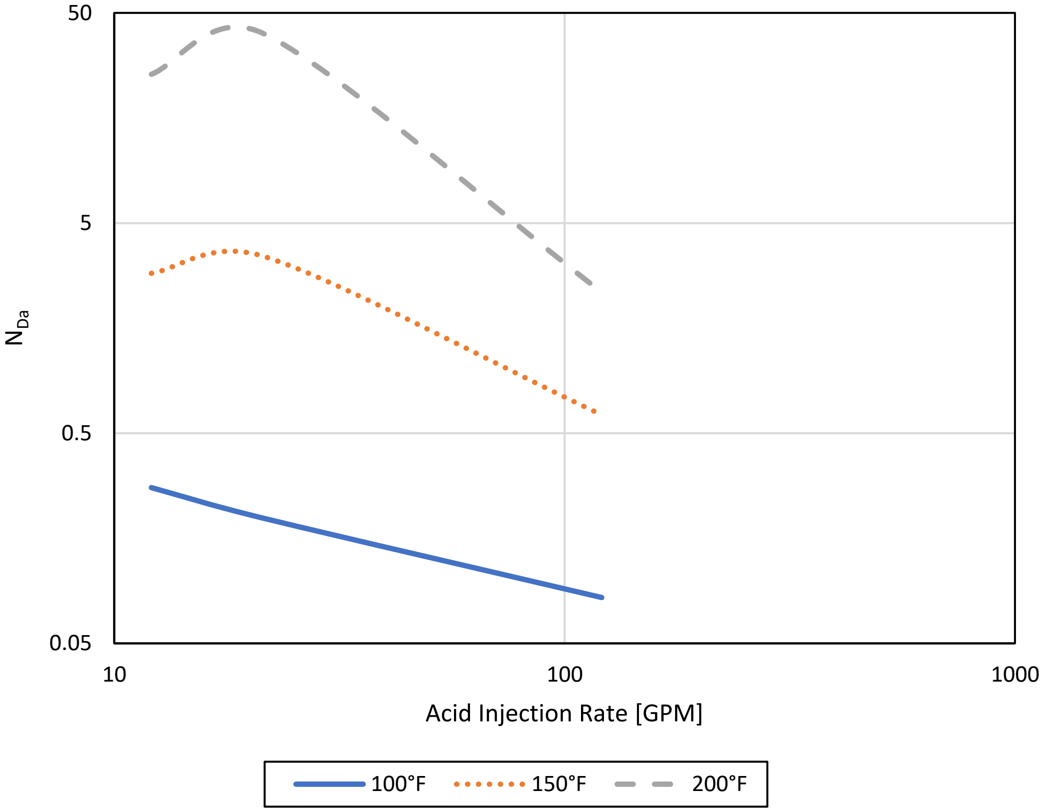

Fig. 4.12 – Damköhler number of 15 wt% HCl injected at different rates in the CFA-Calcite model with different formation temperatures and a fracture conductivity of 275 md-ft.

It can be observed from **Fig. 4.12** that Damköhler number increases with the increase in temperature due to the increase in the reaction rate of acid-rock system.

Although the fracture conductivity in this study is low, the peak points can only be observed at the temperatures of 150°F and 200°F. The peak points on the curves of 150°F and 200°F temperatures are associated with the initiation of dominant and deep wormholes that propagated from the fracture during CFA operation. This point does not exist on the curve of 100°F temperature as it is a straight line with very low values of Damköhler number which indicates that there is no dominant wormhole growth in the domain, and the low Damköhler number for the case of 100°F indicates the change in the dissolution regime from the conventional diffusion-controlled regime in calcite formations to reaction-controlled regime that is independent on acid injection rate. It can be concluded that the results of Damköhler numbers for different temperatures align with the results that was discussed in the previous section of the temperature effect on CFA process. High temperatures exhibit high values of Damköhler number that are associated with sharp acid concentration profile in the fracture with extensive acid leakoff into the formation. While low temperatures exhibit low value of Damköhler number that are associated with smooth acid concentration gradient and steep front pattern during acid flow in the domain.

5. CLOSED-FRACTURE ACIDING IN DOLOMITE FORMATION[3]

In this section, closed-fracture acidizing was studied thoroughly in dolomite formation. Two CFA models were developed in this study that adapt the same model scale and dimensions as the one studied in calcite section, these models are vertical well model and horizontal well model to study the effect of well geometry on CFA operation. For the vertical well model, the model is populated with the porosity distribution profile that belongs to Silurian Dolomite core shown in **Fig. 2.4**. While for the horizontal well model, the model is populated with two different porosity distribution profiles which are the HPD model populated with Silurian Dolomite porosity distribution shown in **Fig. 2.4** and LPD model populated with Guelph Dolomite porosity distribution shown in **Fig. 2.5** to study the effect of formation permeability on CFA operation. The CFA models are demonstrated in the Methodology section.

5.1. Pressure Profile of CFA-Dolomite Models

After initializing the models with the desired porosity distribution profiles. The models are run in an algorithmic sequence to apply two-scale continuum approach and solve for the transport equations and porosity evolution during CFA for each time step which is defined in **Eq. 5.1** as,

---

[3] Partially reprinted with permission from "Acid Wormholing in Multistage Acid Fractured Wells Completed in Tight Naturally Fractured Dolomite Formation: Benefits and Impacts on Acid Fracturing Stimulation Design" by K. Aldhayee, M. Ali, and H. Nasr-El-Din, 2019. SPE-191440-18IHFT-MS, Copyright 2019 by Society of Petroleum Engineers.

$$Time\ Step = 0.5\ \times Actual\ Flowing\ Time\ (seconds) \qquad (5.1)$$

For each time step, Total Pressure (TP) is calculated in ANSYS FLUENT using PISO scheme for the solution of pressure-velocity coupling. The simulation parameters used to solve the equations in all CFA-Dolomite models are shown in **Table 2.4**. For each simulation run, different conditions are imposed in the model with different acid injection rates. Pressure profile for each run is recorded as a graph of relative pressure versus time step. Relative pressure (RP) of specific time step is defined in **Eq. 5.2** as,

$$RP_{Time\ step} = \frac{TP_{Time\ step}}{TP_{initial}} \qquad (5.2)$$

For example, running the horizontal well LPD model for 28 wt% HCl injected at 12.09 GPM yields the pressure profile as shown in **Fig. 5.1**. The pressure profile demonstrates the flow pattern of acid during CFA. First, slight increase in the total pressure indicating the injection of acid in the fracture with no reactions taking place between the acid system and the dolomite matrix existed in the fracture. When the reaction takes place and the acid starts to flow in the formation as a result of acid leakoff out of the fracture, the pressure decreases from the initial trend indicating the initiation of wormholes in the model. As the flow of acid proceeds in the fracture, the wormholes that were initiated will grow until it reaches a point where the flow of acid in the wormholes competes the flow in the fracture and a significant amount of acid will propagate in the formation. Finally, the acid will reach the boundaries of the model and the total pressure decreases 100 times of its initial value indicating that the acid reached the state of breakthrough. For the simulation models, the initial conditions are zero velocity field in the medium and zero acid concentration. As for the boundary conditions, constant injection velocity at the injection inlet and no flow boundary imposed at the top, bottom and front side of the model. The lateral sides of the model are the outlets of the model in which acid flux and pressure equals zero.

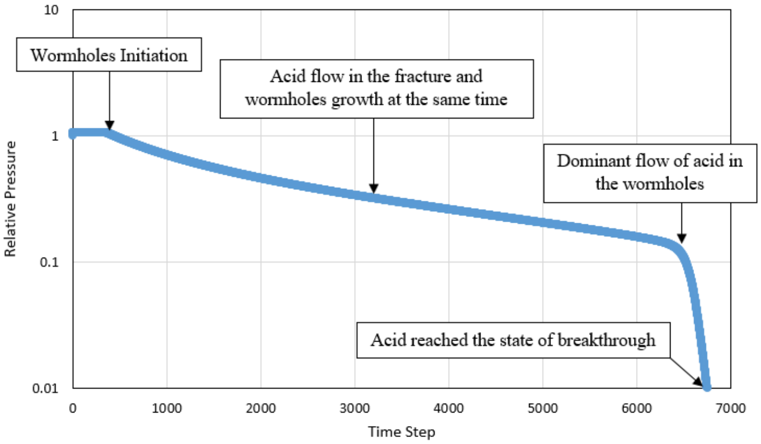

Fig. 5.1 – Pressure Profile of horizontal LPD model after injecting 28 wt% HCl at injection rate of 12.09 GPM

5.2. Vertical Well Performance

Acid is injected in the closed-fracture at injection rates shown in **Table 5.1**. Field injection rates were obtained by assuming a fracture geometry of 0.5 inch aperture and 10 feet height, then multiplying the injection velocity with the injection area of the fracture to obtain the field injection rate.

Table 5.1 – Acid injection rates used in the CFA-Dolomite vertical well model. Reprinted with permission from SPE-191440-18IHFT-MS.

Injection Velocity (m/s)	**Field Injection Rate (GPM)**
0.0008	0.49
0.0045	2.76
0.008	4.91
0.045	27.61
0.08	49.10

At very low injection rate (0.49 GPM), acid concentration has significant effect on wormholing during CFA as illustrated in **Fig. 5.2**. Wormholes were initiated after injecting 69.5 gallons of 15 wt% HCl while they were initiated after injecting 5.11 gallons of 28 wt% HCl. The reason for this behavior of wormholing phenomena is that the dissolution process is controlled by the acid diffusion and how strong the acid system is.

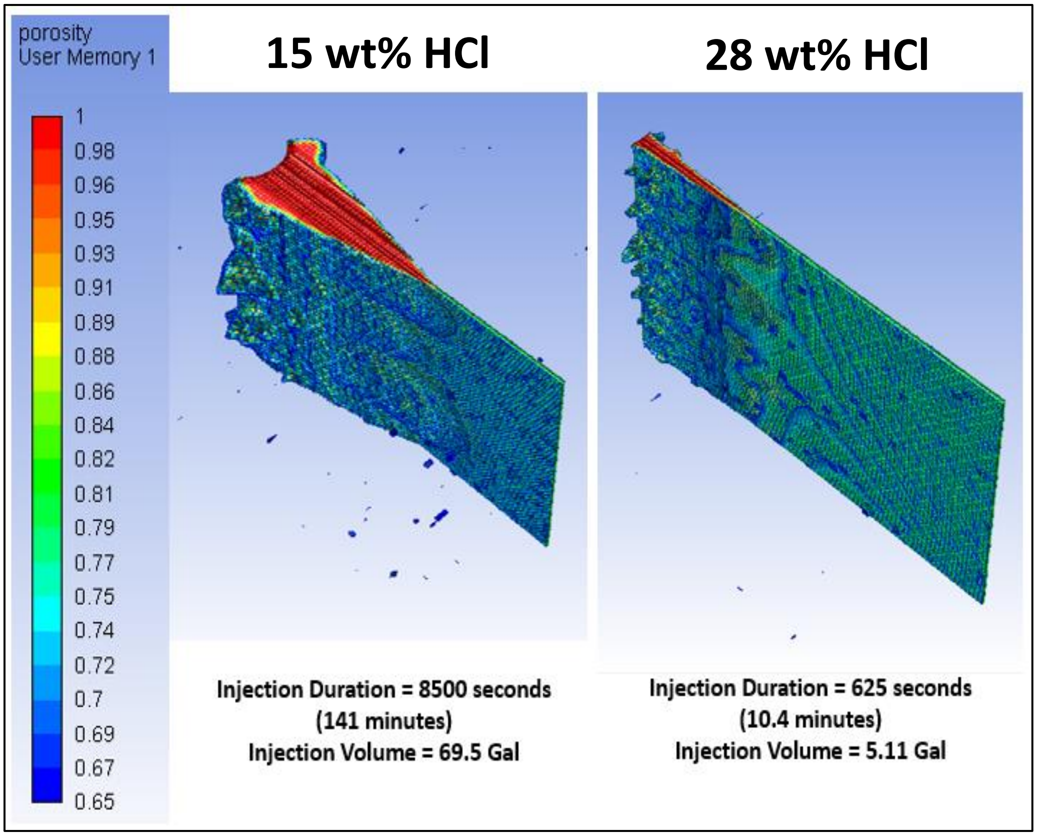

Fig. 5.2 – Wormholes initiation during CFA process of 0.49 GPM with different acid concentrations in CFA-Dolomite vertical well model.

Fig. 5.3 demonstrates the pressure profile for the vertical well model utilizing different injection rates and acid concentrations. The pressure profile follows a general trend for all the rates and concentrations as it decreases very slowly at the early time steps indicating a dominant flow of acid in the fracture. The first sharp decrease of the pressure indicates the initiation of wormholes and the starting point where the acid flows significantly in the formation which leads to the wormhole growth until the acid reaches the breakthrough state of relative pressure equals to 0.01.

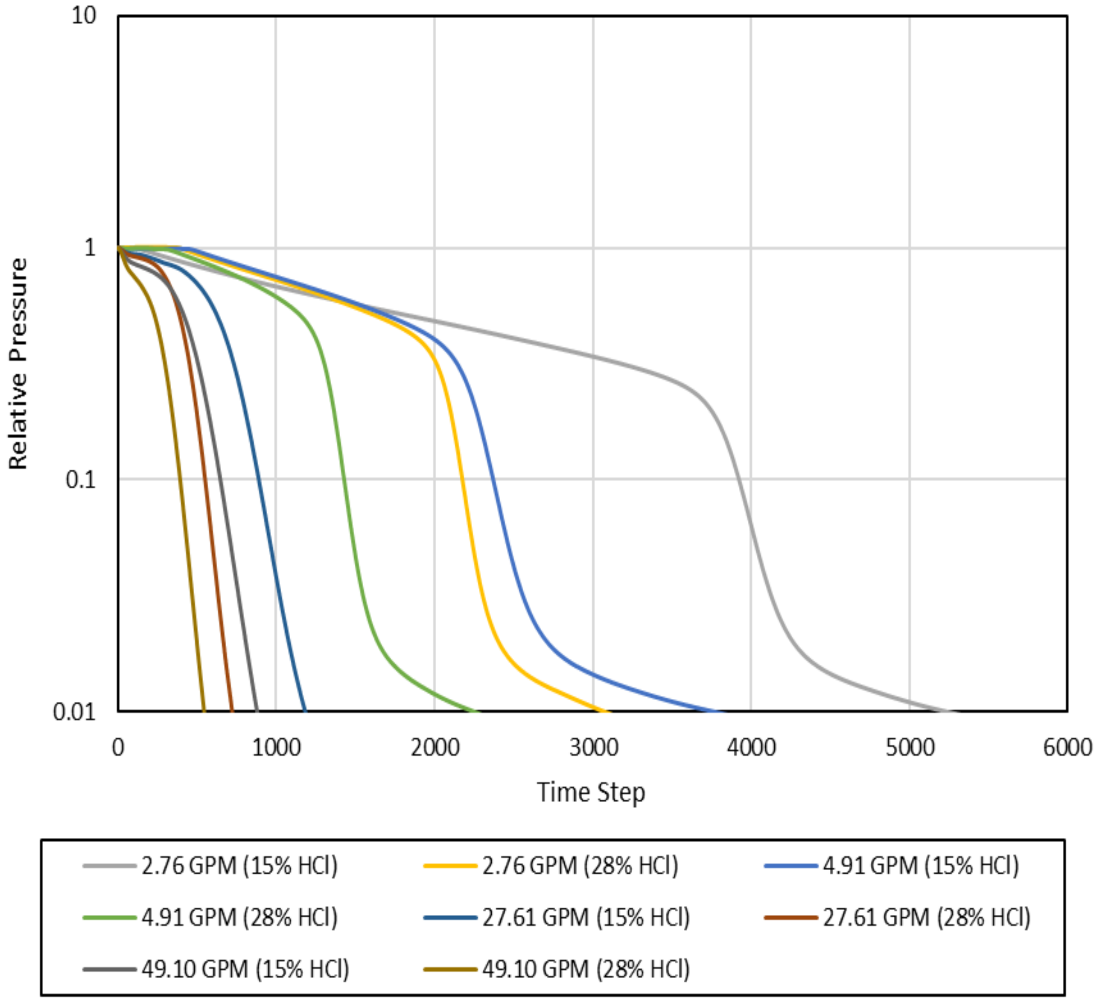

Fig. 5.3 – Pressure profiles of the CFA-Dolomite vertical well model illustrating different injection rates and acid concentrations.

At 4.91 GPM injection rate, Wormholes were initiated after injecting 12.3 gallons of 15 wt% HCl while they were initiated after injecting 8.2 gallons of 28 wt% HCl. **Fig. 5.4** shows the dissolution pattern of the closed fracture and the initiation of wormholes. It can be noticed that the dissolution pattern and the initiation of wormholes have the same shape for both 15 wt% HCl and 28 wt% HCl, but the higher acid concentration accelerates the dissolution process which will require less total injected volume of acid.

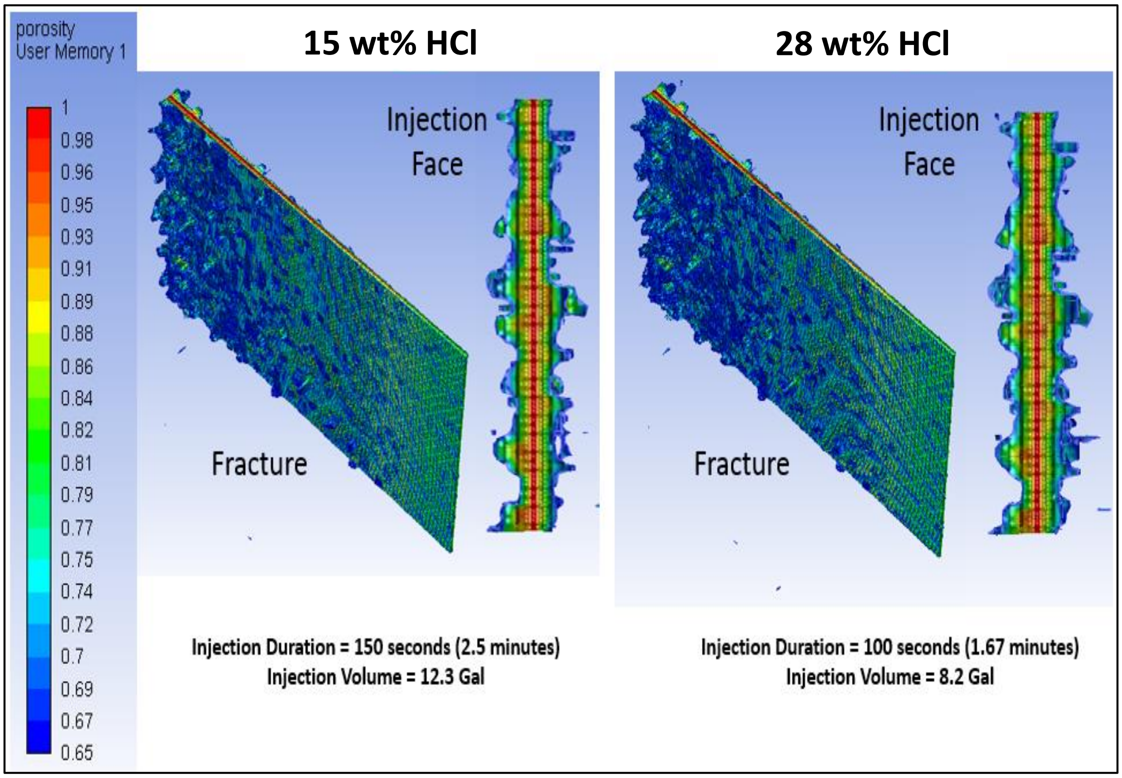

Fig. 5.4 – Wormholes initiation during CFA process of 4.91 GPM with different acid concentrations in CFA-Dolomite vertical well model.

As for the breakthrough state of 4.91 GPM, the injected volume to breakthrough for 15 wt% HCl is 163 gallons while the injected volume to breakthrough for 28 wt% HCl is 88 gallons. **Fig. 5.5** shows the dissolution pattern and wormholes growth at the state of breakthrough for 4.91 GPM with different acid concentrations in vertical well model. The same conclusion can be drawn here is that the dissolution patterns for both concentrations (15 wt% HCl and 28 wt% HCl) have the same dissolution pattern but the higher concentration accelerated the dissolution process with less required volume of injected acid.

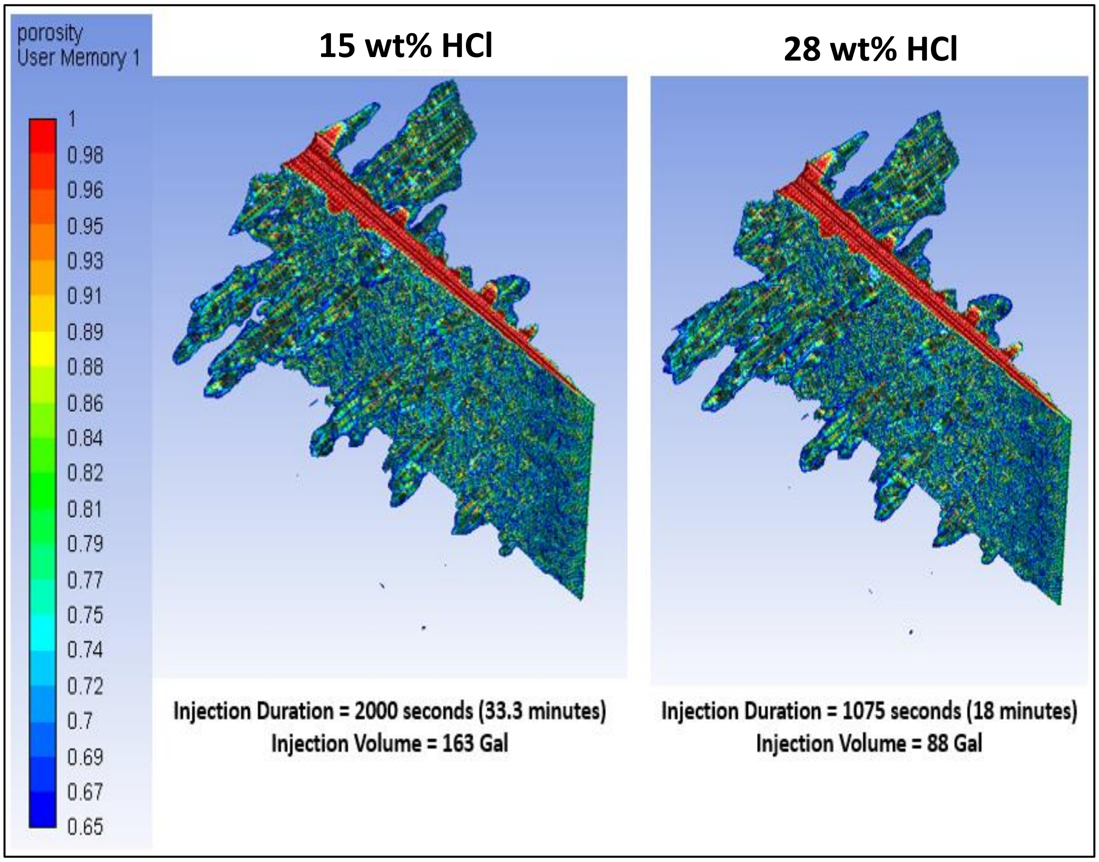

Fig. 5.5 – Breakthrough state of 4.91 GPM with different acid concentrations in the CFA-Dolomite vertical well model. Reprinted with permission from SPE-191440-18IHFT-MS.

At 49.10 GPM injection rate, the injection velocity is high, and the acid is penetrating the formation at the beginning of acid injection in the closed-fracture. **Fig. 5.6** shows the dissolution pattern of the closed fracture and the initiation of wormholes for 49.10 GPM for both 15 wt% HCl and 28 wt% HCl. The dissolution patterns are identical and the required injected volumes for both acid concentration to initiate wormholes are close to each other because the dissolution process is controlled by surface reaction between the acid and the formation, and since the formation is dolomite and the reaction is too slow between HCl and dolomite, it needs certain amount of time to create wormholes in the formation.

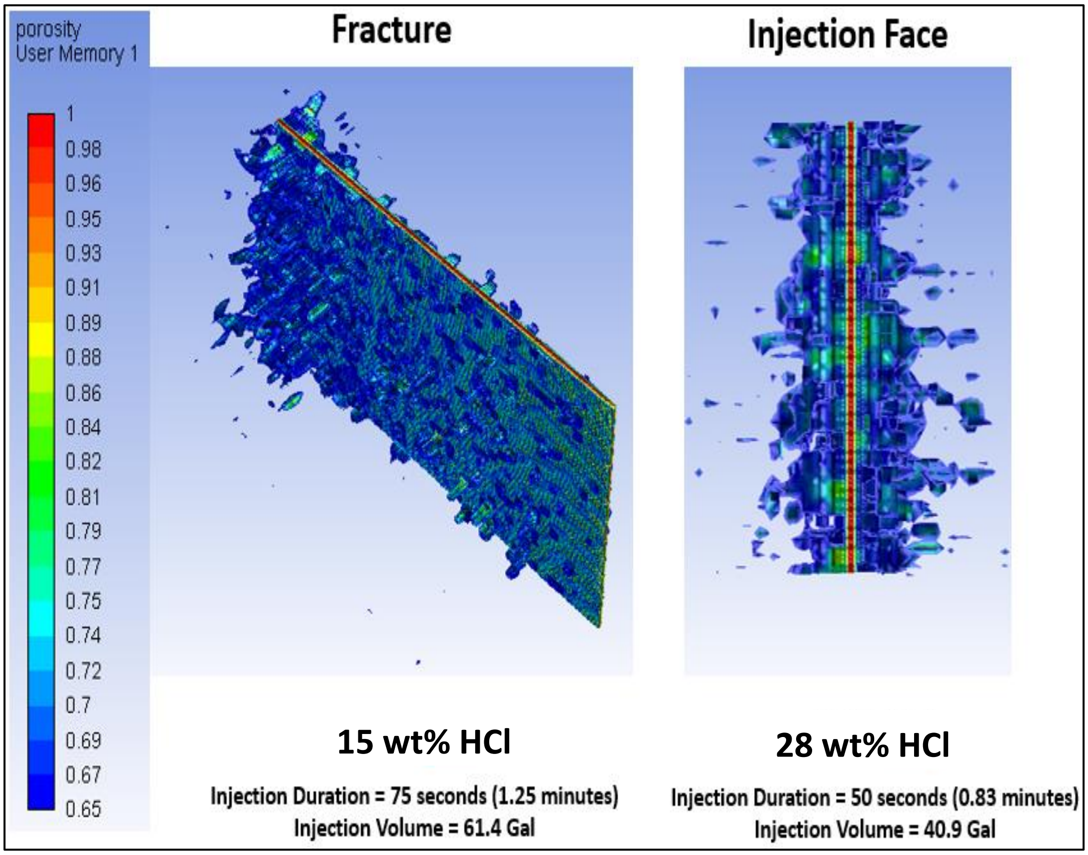

Fig. 5.6 – Wormholes initiation during CFA process of 49.10 GPM with different acid concentrations in the CFA-Dolomite vertical well model.

As for the breakthrough state of 49.10 GPM, the injected volume to breakthrough for 15 wt% HCl is 327.2 gallons while the injected volume to breakthrough for 28 wt% HCl is 225 gallons. **Fig. 5.7** shows the dissolution pattern and wormholes growth at the state of breakthrough for 49.10 GPM with different acid concentrations in vertical well model. In this case, wormholes are concentrated at the inlet of acid injection face, and they are not distributed evenly along the fracture area as in the case shown in **Fig. 5.5**. The injection rate is very high that the flow in the formation is competing with the flow in the fracture even though the fracture is highly conductive.

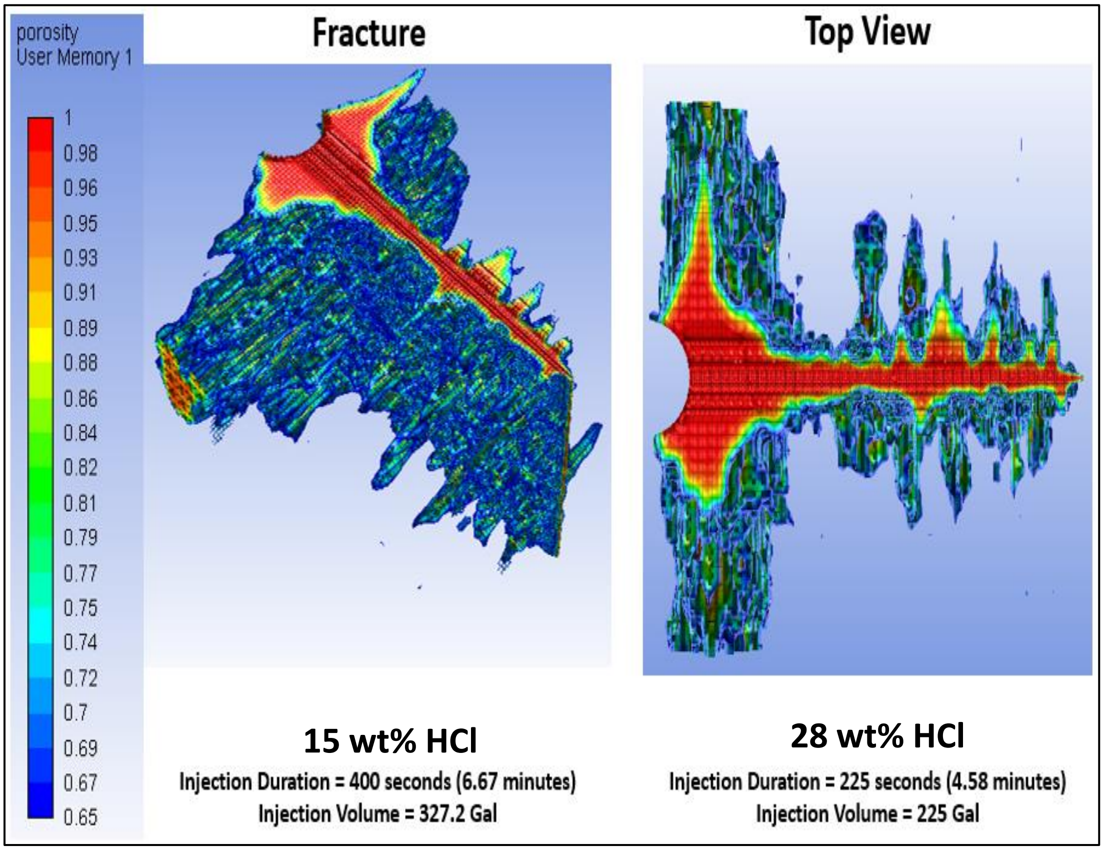

Fig. 5.7 – Breakthrough state of 49.10 GPM with different acid concentrations in the CFA-Dolomite vertical well model. Reprinted with permission from SPE-191440-18IHFT-MS.

Fig. 5.8 shows the required acid volume for 15 wt% HCl and 28 wt% HCl to initiate wormholes at different injection rates. At very low injection rate, the acid concentration has significant effect on wormholing phenomena in CFA since the dissolution process is dominated by acid diffusion. **Fig. 5.9** shows the required acid volume for 15 wt% HCl and 28 wt% HCl to breakthrough at different injection rates. The total injected acid volume required to breakthrough for 28 wt% HCl is always less than the total injected acid volume required to breakthrough for 15 wt% HCl. Higher acid concentration accelerates the dissolution process given that the dissolution patterns are the same for both acid concentrations. The reason for this behavior is that the formation is dolomite and the dissolution process is controlled by the surface reaction between the acid system and the formation which is too slow and depend highly on acid concentration and soaking time of acid in the formation. As a conclusion, 28 wt% HCl is utilized for the subsequent sections as it is effective in the dissolution process of dolomite formation.

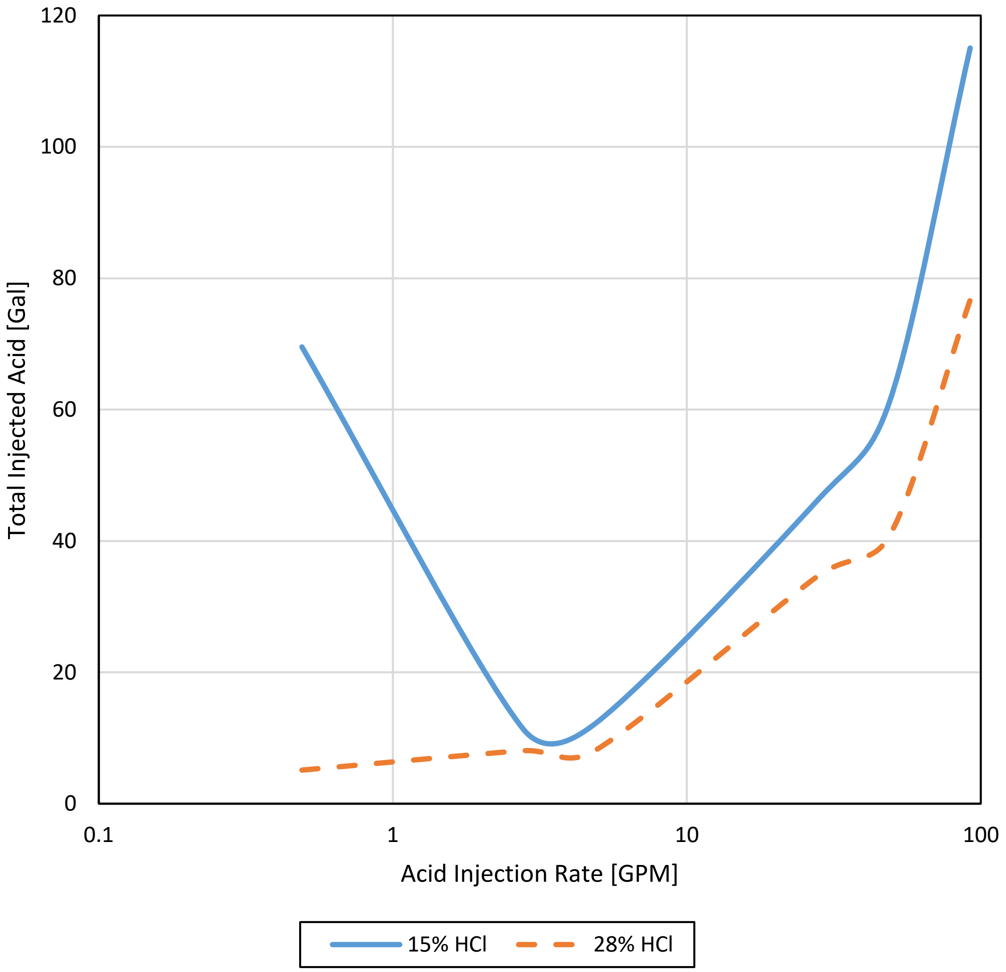

Fig. 5.8 – Wormholes initiation of 15 wt% HCl and 28 wt% HCl injected at different rates in the CFA-Dolomite vertical well model.

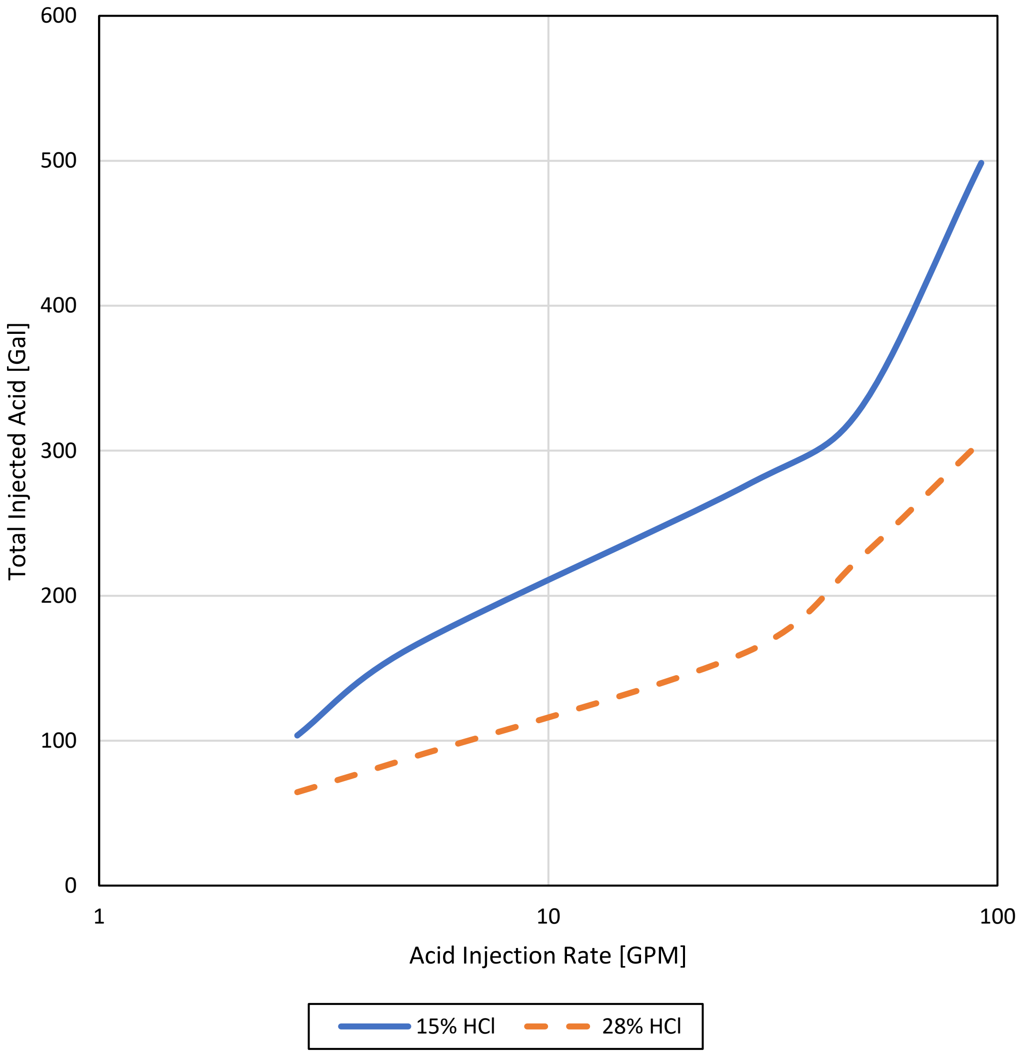

Fig. 5.9 – Total acid injected volume to breakthrough of 15 wt% HCl and 28 wt% HCl injected at different rates in CFA-Dolomite vertical well model. Reprinted with permission from SPE-191440-18IHFT-MS.

5.3. HPD Horizontal Well Performance

Acid is injected in the closed-fracture at injection rates shown in **Table 5.2**. Field injection rates were obtained by assuming a fracture geometry of 0.5 inch aperture and a wellbore radius of 0.3 feet, then multiplying the injection velocity with the injection area of the fracture to obtain the field injection rate.

Table 5.2 – Acid injection rates used in the CFA-Dolomite horizontal well model. Reprinted with permission from SPE-191440-18IHFT-MS.

Injection Velocity (m/s)	Field Injection Rate (GPM)
0.0008	2.15
0.0045	12.09
0.008	21.50
0.045	120.90

At very low injection rate (2.15 GPM), the wormholing phenomenon that occurs in the fracture is similar to the wormholing phenomenon that occurs in the cores during coreflooding with low injection rate which is face dissolution. **Fig. 5.10** shows the dissolution of the fracture after injecting 28 wt% HCl for a certain duration of time. It can be noticed that the acid flow is favorable in the fracture rather than the formation since the momentum of acid is not highly enough for the acid to propagate through formation; hence no wormholes have been formed. However, the acid is reacting with fracture walls and expanding them which results in face dissolution pattern in the fracture.

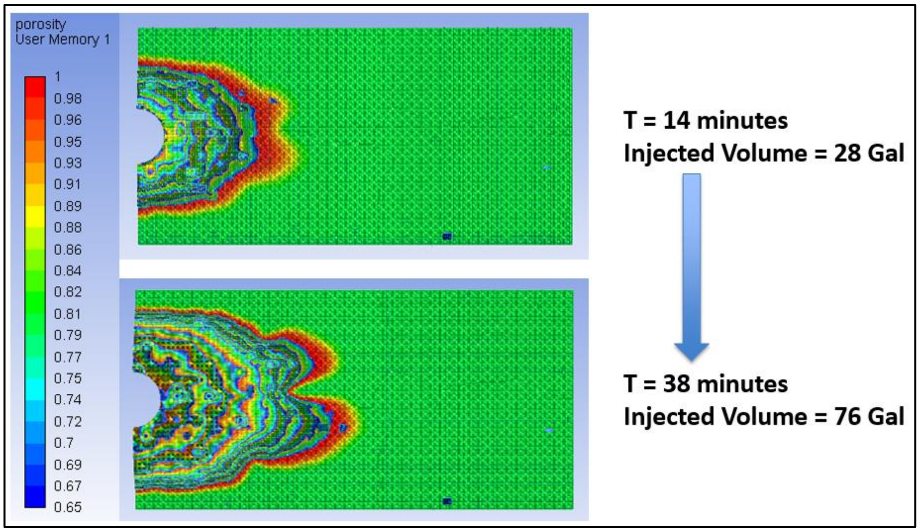

Fig. 5.10 – Dissolution of the acid-fracture at 2.15 GPM acid injection rate of 28 wt% HCl in the HPD horizontal well model.

Fig. 5.11 shows the pressure profile of the horizontal model illustrating different injection rates for 28 wt% HCl and demonstrates the wormholes initiation in the model and the state of breakthrough for each acid injection rate.

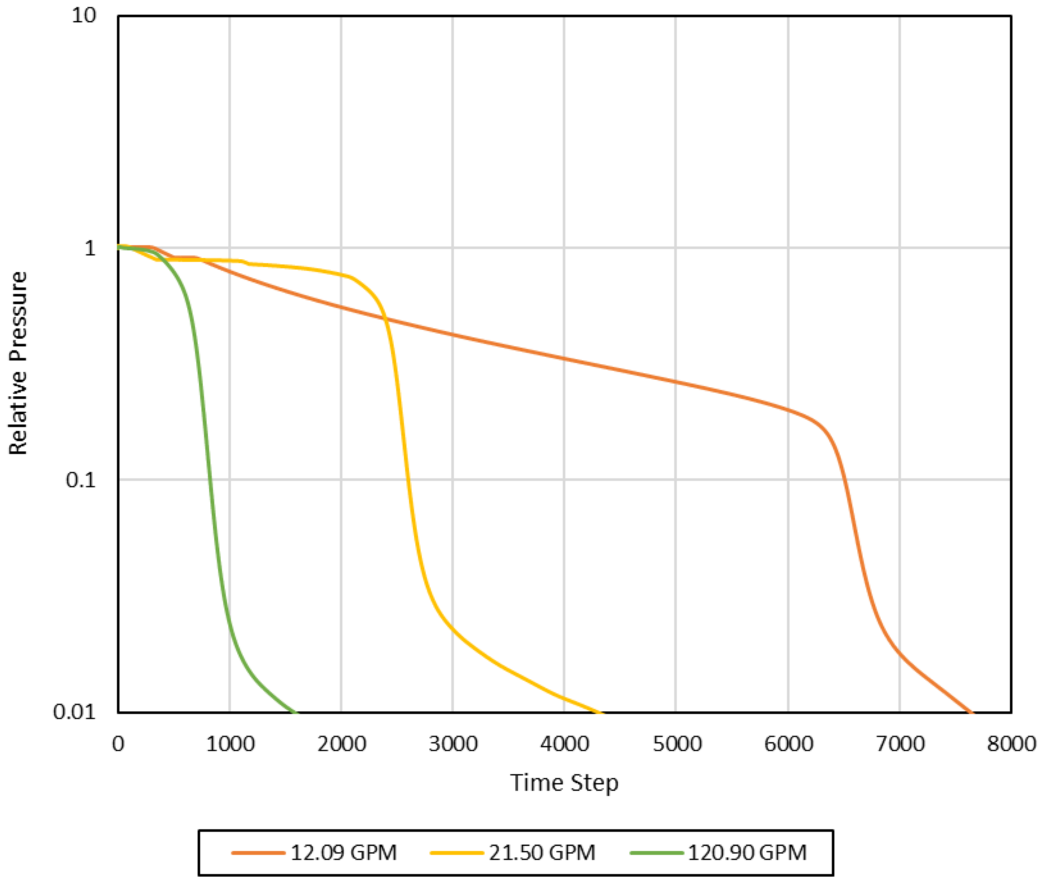

Fig. 5.11 – Pressure profiles of the HPD horizontal well model illustrating different injection rates of 28 wt% HCl.

For 12.09 GPM injection rate, the wormholes initiation occurs after injecting 50.4 gallons as shown in **Fig. 5.12**. Before reaching breakthrough state, the wormholes that were initiated will grow as the acid travels certain distance in the fracture, and then the acid flows even further in the wormholes as it competes with the fracture in the flowing of acid as shown in **Fig. 5.13**. At the state of breakthrough, the acid volume required to breakthrough is 775 gallons, and it can be noticed that the wormholes are concentrated at the injection inlet and parallel to the direction of the horizontal well as shown in **Fig. 5.14**. The top view of **Fig. 5.14** shows extensive dissolution of the fracture at the injection inlet indicating face dissolution pattern.

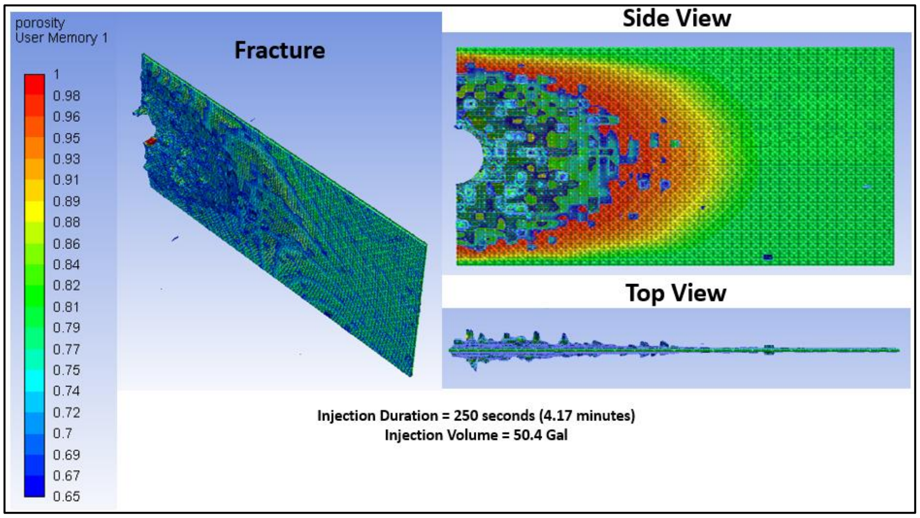

Fig. 5.12 – Wormholes initiation of 28 wt% HCl injected at 12.09 GPM in HPD horizontal well model.

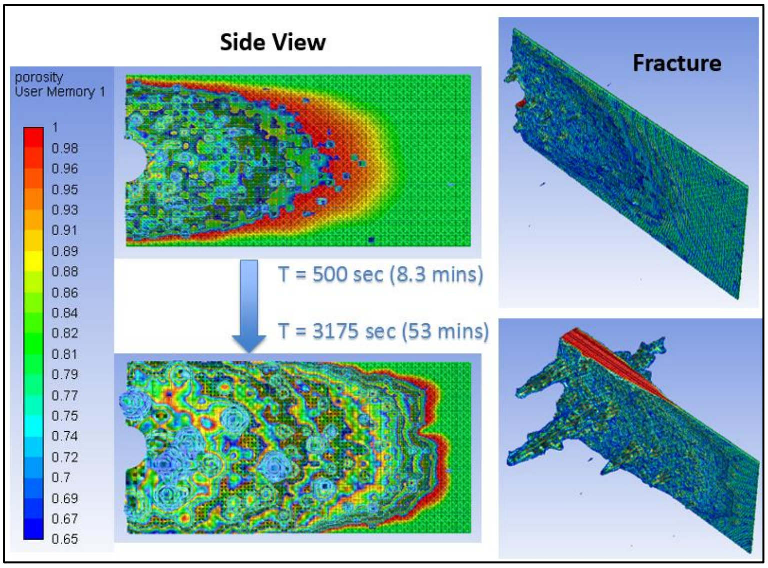

Fig. 5.13 – Acid flow in the fracture and wormholes growth before reaching the state of breakthrough for 12.09 GPM injection rate in the HPD horizontal well model.

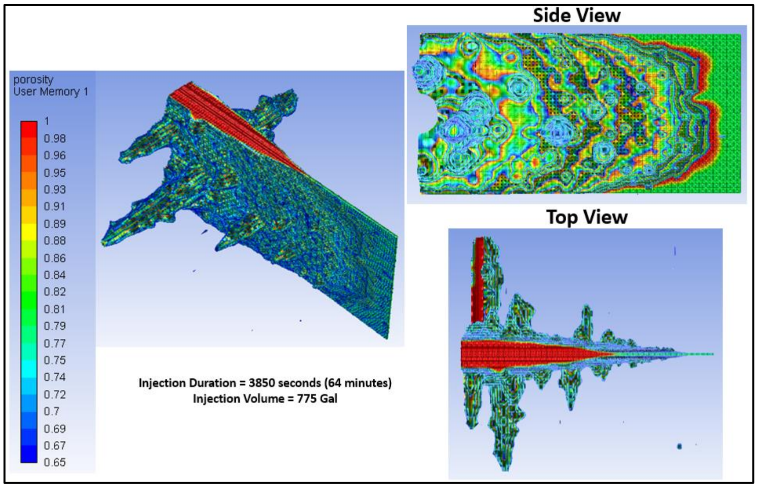

Fig. 5.14 – Breakthrough state of 28 wt% HCl injected at 12.09 GPM in the HPD horizontal well model. Reprinted with permission from SPE-191440-18IHFT-MS.

For 21.50 GPM injection rate, the wormholes initiation occurs after injecting 71.6 gallons as shown in **Fig. 5.15**. Before reaching breakthrough state, the wormholes that were initiated are distributed evenly across the fracture area and developing as the acid flow through the fracture as shown in **Fig. 5.16**. At the state of breakthrough, the acid volume required to breakthrough is 796.9 gallons and it can be noticed that the wormholes are developed at certain distance in the fracture and not only concentrated in the injection inlet as shown in **Fig. 5.17**.

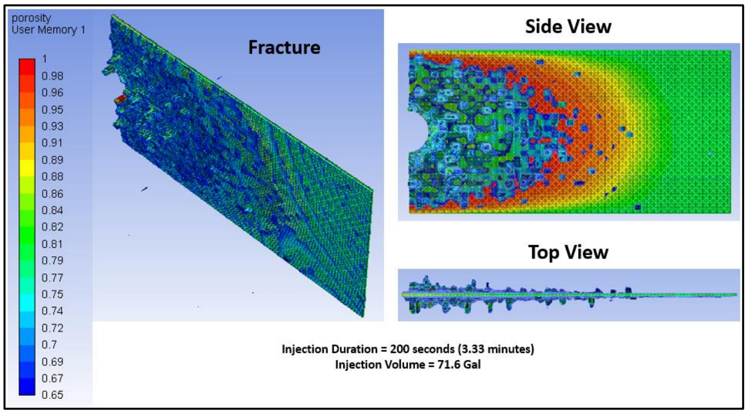

Fig. 5.15 – Wormholes initiation of 28 wt% HCl injected at 21.50 GPM in HPD horizontal well model.

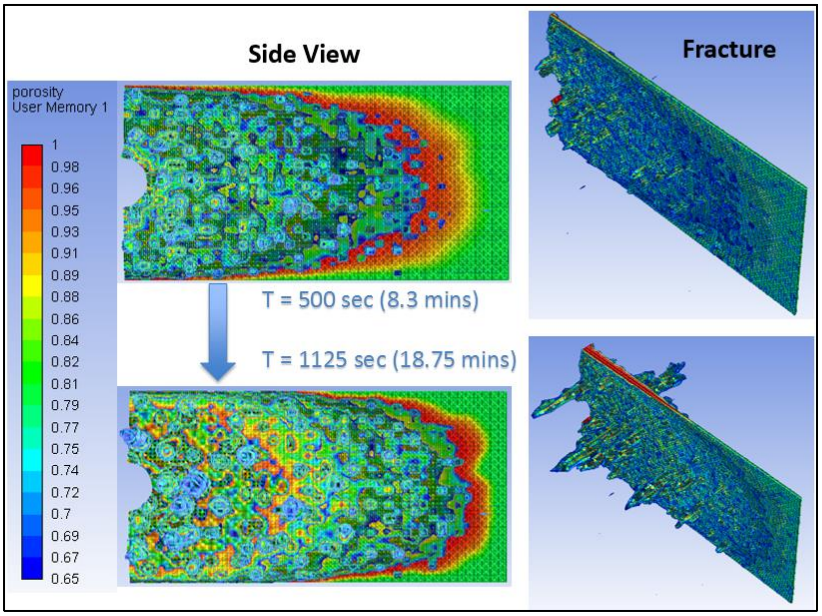

Fig. 5.16 – Acid flow in the fracture and wormholes growth before reaching the state of breakthrough for 21.50 GPM injection rate in the HPD horizontal well model.

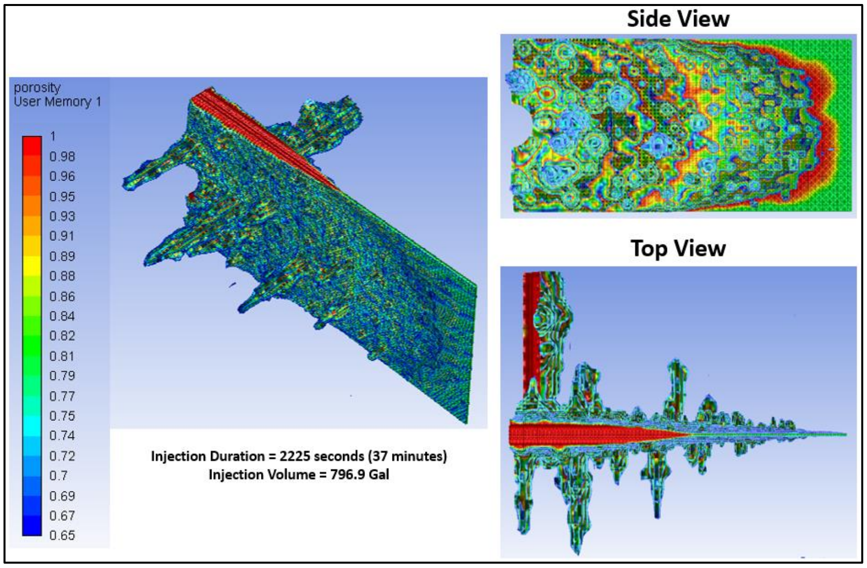

Fig. 5.17 – Breakthrough state of 28 wt% HCl injected at 21.50 GPM in the HPD horizontal well model. Reprinted with permission from SPE-191440-18IHFT-MS.

For 120.90 GPM injection rate, the wormholes initiation occurs after injecting 201.5 gallons as shown in **Fig. 5.18**, it can be noticed that significant acid leak-off occurs at the beginning of acid injection in the closed-fracture, and the delayed time of wormholes initiation is caused by the slow reaction between HCl and dolomite system. At the state of breakthrough, the acid volume required to breakthrough is 1108 gallons and the wormholes are evenly distributed along the fracture area with approximately same geometry as shown in **Fig. 5.19**.

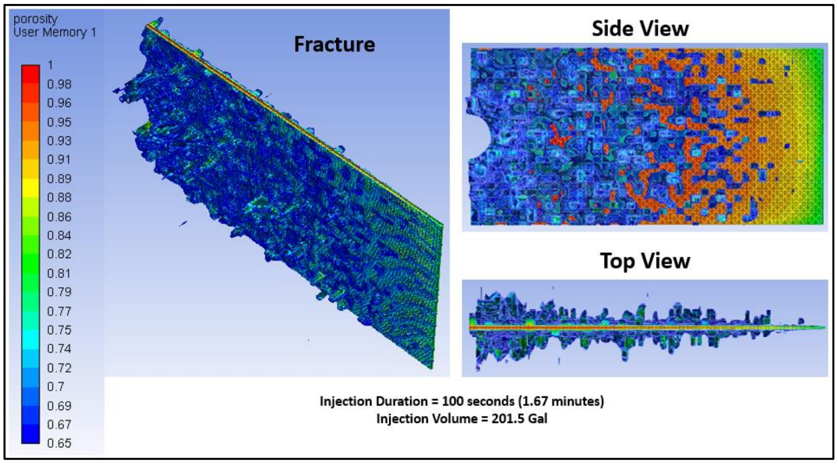

Fig. 5.18 – Wormholes initiation of 28 wt% HCl injected at 120.90 GPM in HPD horizontal well model.

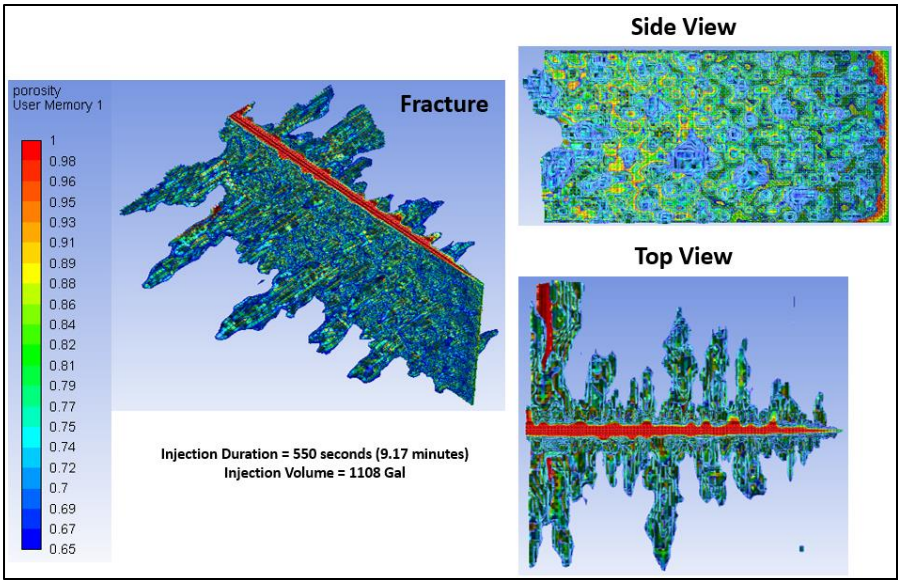

Fig. 5.19 – Breakthrough state of 28 wt% HCl injected at 120.90 GPM in the HPD horizontal well model. Reprinted with permission from SPE-191440-18IHFT-MS.

5.4. Effect of Well Geometry

In the previous sections, vertical well model and horizontal well model has been discussed separately. **Fig. 5.20** illustrates the pressure profiles of both models for 28 wt% HCl injected at different injection velocities. Injection velocities were investigated in this section to demonstrate the effect of injection area on CFA. **Fig. 5.21** and **Fig. 5.22** can be generated from the pressure profile shown in **Fig. 5.20**. From **Fig. 5.21**, it can be concluded that wormholes initiation requires less acid volume in vertical wells than horizontal wells because of the large injection area in the vertical wells that is available for the acid to flow. From **Fig. 5.22**, the total acid volume required to breakthrough for the vertical well model is always less than the total acid volume required to breakthrough for the horizontal well model for the same mentioned reason.

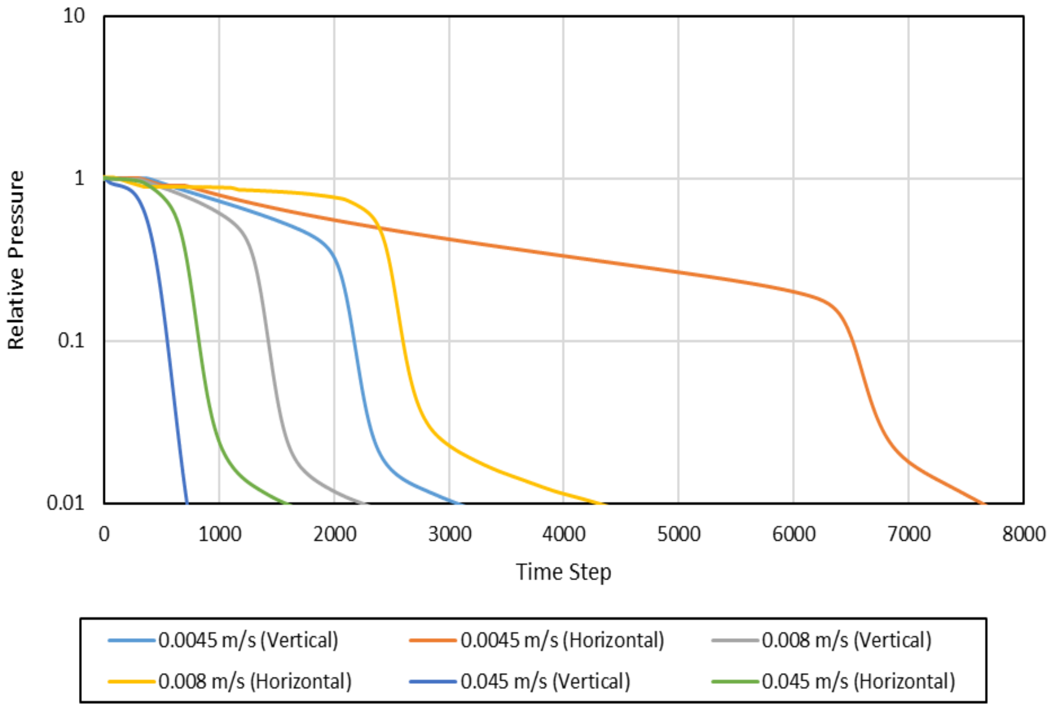

Fig. 5.20 – Pressure Profiles of vertical well model and HPD horizontal well model for 28 wt% HCl injected at different injection velocities.

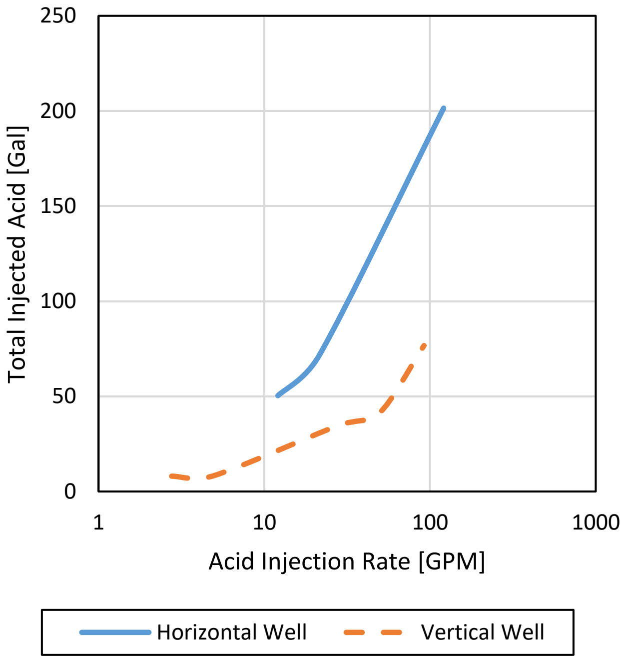

Fig. 5.21 – Wormholes initiation in vertical well model and HPD horizontal well model for 28 wt% HCl injected at different rates.

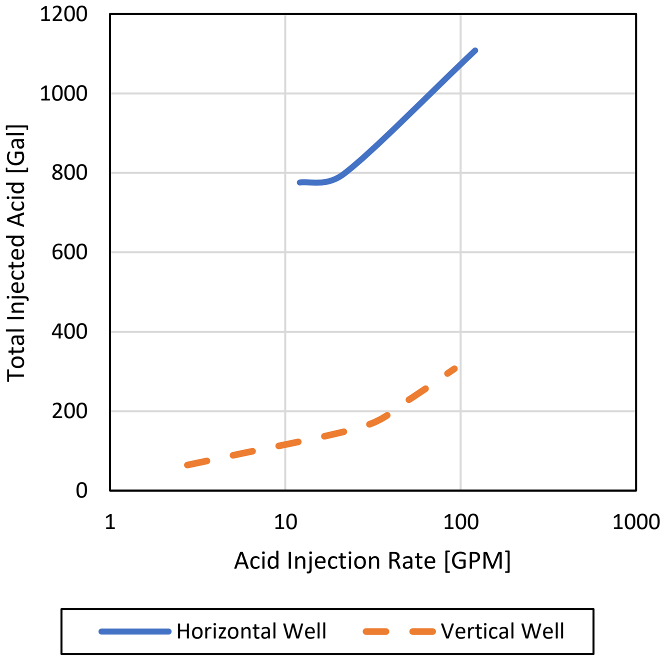

Fig. 5.22 – Total acid volume injected to breakthrough in vertical well model and HPD horizontal well model for 28 wt% HCl injected at different rates. Reprinted with permission from SPE-191440-18IHFT-MS.

5.5. LPD Horizontal Well Performance

In the previous sections, high-permeability dolomite was discussed in detail for both vertical well model and horizontal well model. In this section, low-permeability dolomite is discussed for horizontal well model, then a comparison will be made for the performance of low-permeability dolomite (LPD) and high-permeability dolomite (HPD). 28 wt% HCl is utilized in this section injected at rates shown in **Table 5.2**.

At very low injection rates (2.15 GPM), **Fig. 5.23** demonstrates the dissolution of the fracture and the flow of the acid as it is mainly prioritizing the fracture during injection since flow is easier in the highly conductive fracture than the tight formation; hence no wormholes have been initiated.

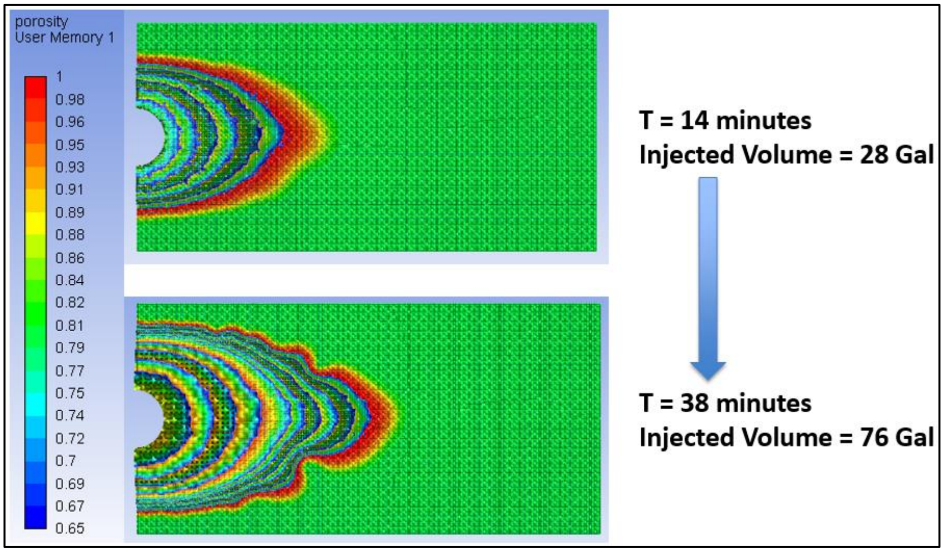

Fig. 5.23 – Dissolution of the acid-fracture at 2.15 GPM acid injection rate of 28 wt% HCl in the LPD model.

Fig. 5.24 shows the pressure profiles of the LPD model illustrating different injection rates of 28 wt% HCl demonstrating the wormholes initiation in the model and the state of breakthrough for each acid injection rate.

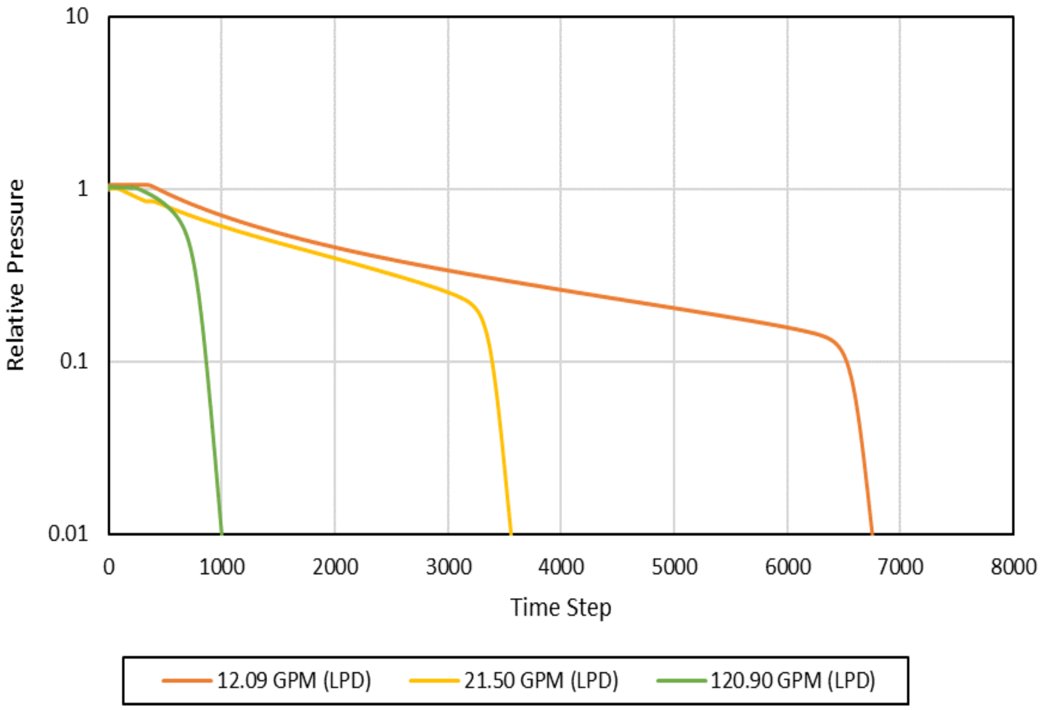

Fig. 5.24 – Pressure profiles of 28 wt% HCl injected at different rates in the LPD model.

For 12.09 GPM injection rate, the wormholes initiation occurs after injecting 60.4 gallons as shown in **Fig. 5.25**. Before reaching breakthrough state, the wormholes initiated at the injection inlet of the fracture are the only wormholes that will grow as the acid travels certain distance in the fracture as shown in **Fig. 5.26**. At the state of breakthrough, the acid volume required to breakthrough is 679.93 gallons and it can be noticed that the acid developed large and wide wormholes at the injection inlet of the fracture indicating significant growth of the wormholes that were initiated previously and that there are no new wormholes formed at the state of breakthrough as shown in **Fig. 5.27**. This wormholing phenomena indicates that the injection rate did not provide the acid with the flow momentum required to propagate through the tight dolomite formation.

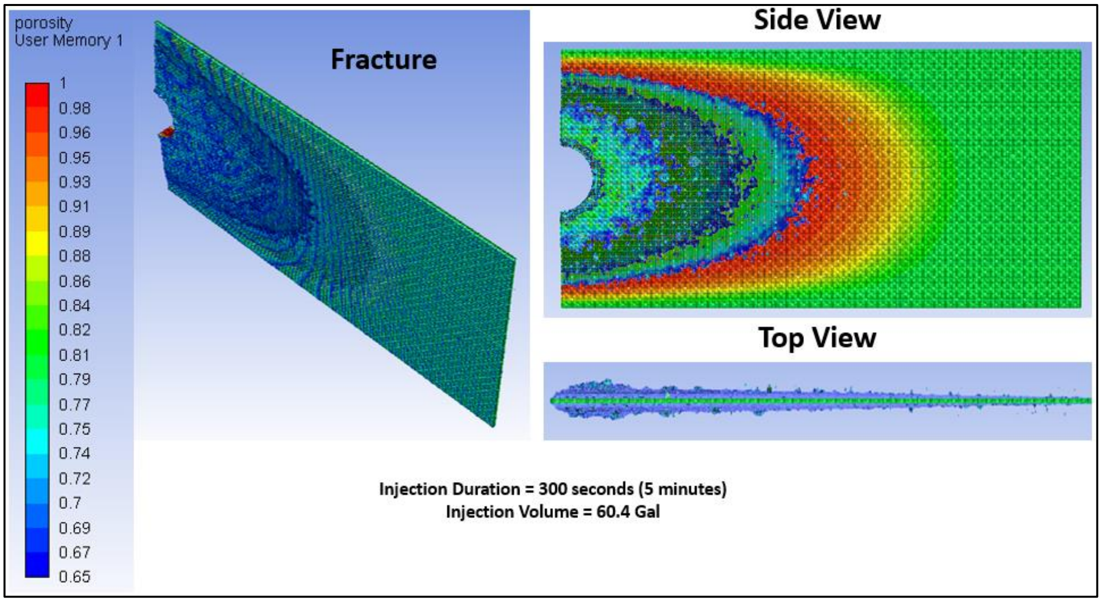

Fig. 5.25 – Wormholes initiation for 28 wt% HCl injected at rate of 12.09 GPM in LPD model.

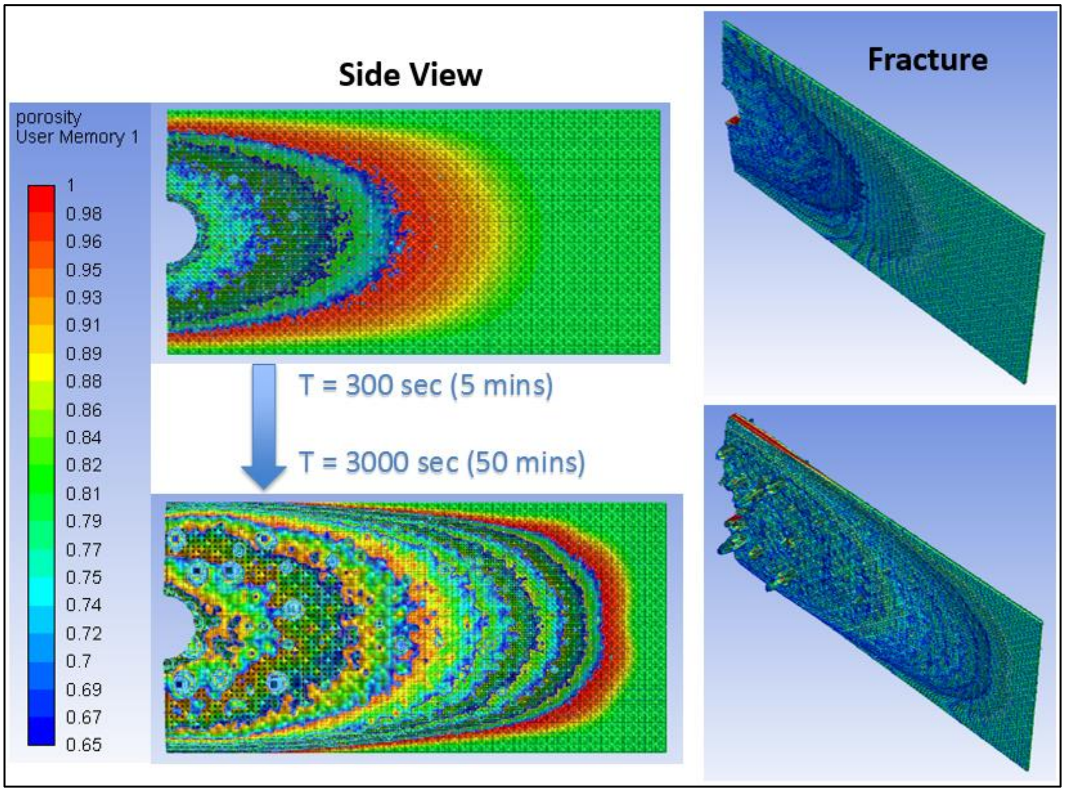

Fig. 5.26 – Acid flow in the fracture and wormholes growth before reaching the state of breakthrough for 12.09 GPM injection rate in the LPD model.

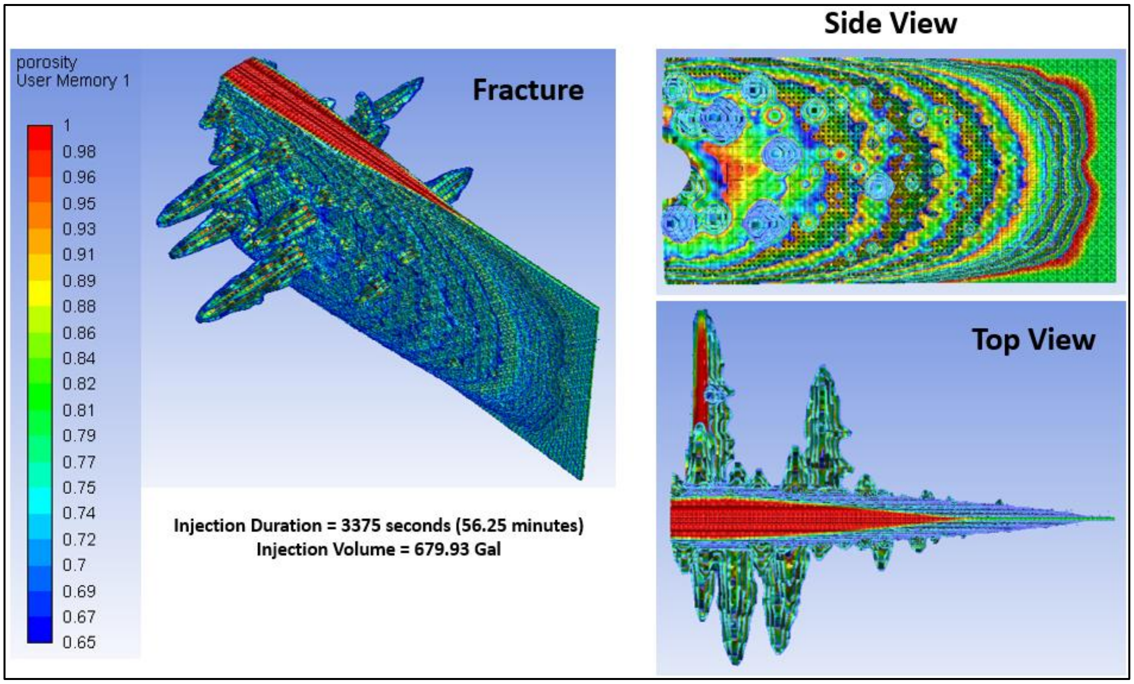

Fig. 5.27 – Breakthrough state of 28 wt% HCl injected at 12.09 GPM in the LPD model. Reprinted with permission from SPE-191440-18IHFT-MS.

For 21.50 GPM injection rate, the wormholes initiation occurs after injecting 62.6 gallons as shown in **Fig. 5.28**. Before reaching breakthrough state, the acid was able to propagate through tight formation as it flows in the fracture and generates small wormholes along the fracture area as shown in **Fig. 5.29**. At the state of breakthrough, the acid volume required to breakthrough is 635.72 gallons, and it can be noticed that wormholes are distributed along the fracture area in which larger wormholes were generated at the injection inlet and were getting smaller as the acid flows in the fracture as shown in **Fig. 5.30**. This womholing phenomena indicates that the acid injection rate has provided the acid with the required flow momentum that enables the acid to propagate through the tight dolomite.

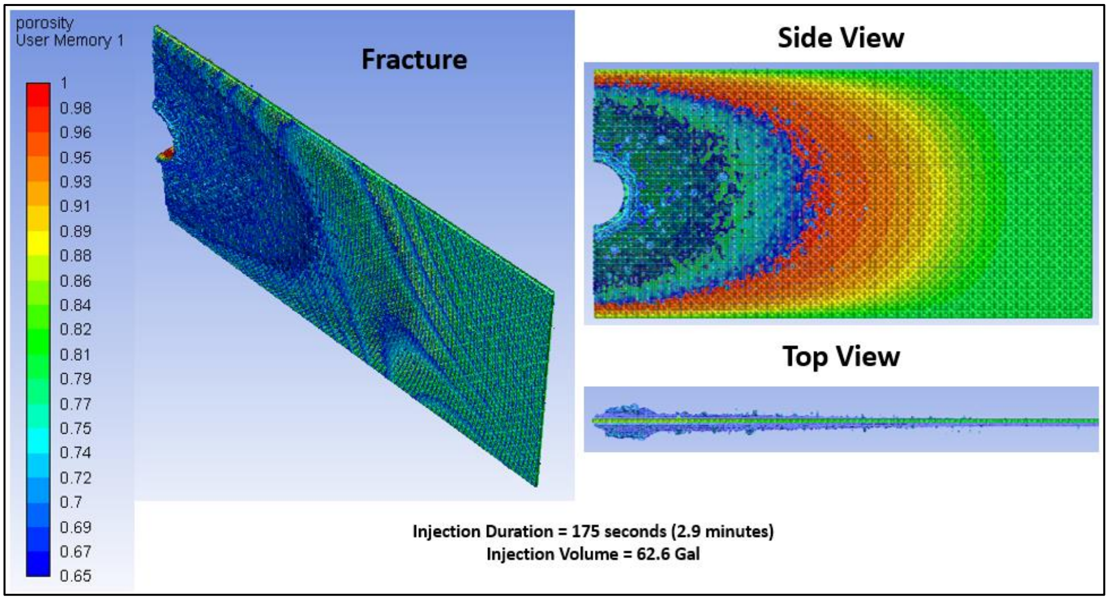

Fig. 5.28 – Wormholes initiation for 28 wt% HCl injected at rate of 21.50 GPM in LPD model.

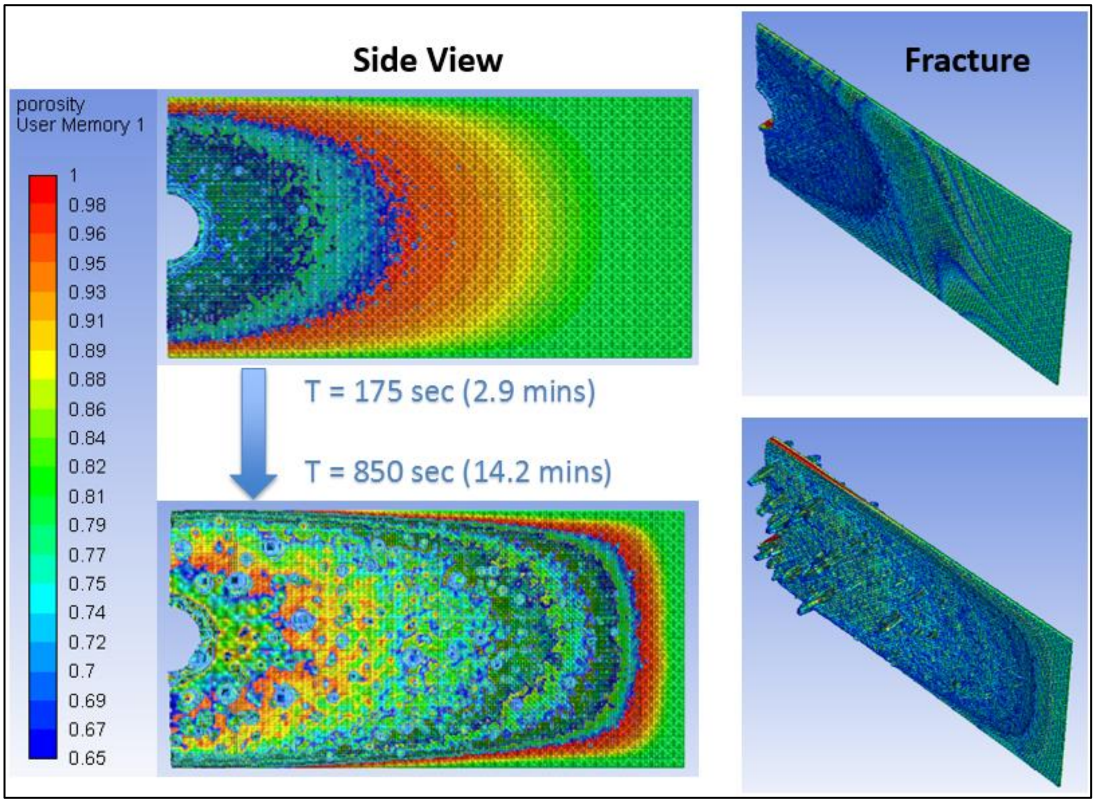

Fig. 5.29 – Acid flow in the fracture and wormholes growth before reaching the state of breakthrough for 21.50 GPM injection rate in the LPD model.

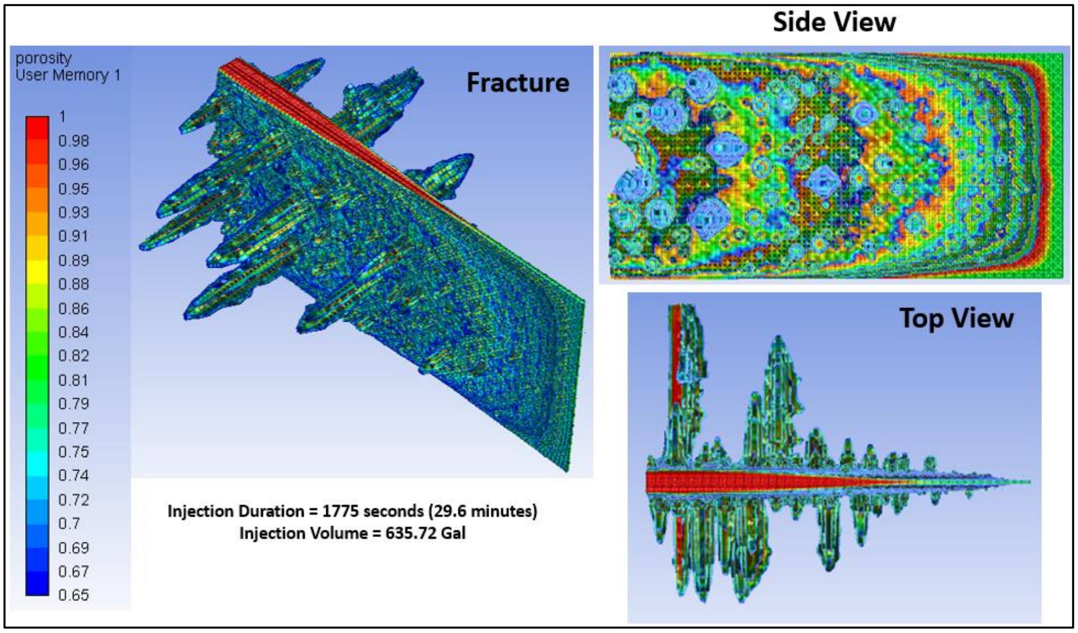

Fig. 5.30 – Breakthrough state of 28 wt% HCl injected at 21.50 GPM in the LPD model. Reprinted with permission from SPE-191440-18IHFT-MS.

For 120.90 GPM injection rate, the wormholes initiation occurs after injecting 302.2 gallons as shown in **Fig. 5.31**, it can be noticed that significant acid leak-off occurs at the beginning of injection and significant dissolution occurs around the vicinity of injection inlet. At the state of breakthrough, the acid volume required to breakthrough is 1007.3 gallons and relatively large wormhole has been generated at the injection inlet compared to the smaller ones that were generated in the fracture as shown in **Fig. 5.32**. This dissolution behavior indicates that the injection rate was relatively high which provided the acid with the required flow momentum for the acid to flow evenly in the fracture and formation regardless the tightness of the dolomite formation. It can also be observed that there is a dominant and deep wormhole that propagate from the fracture around the area of the inject inlet.

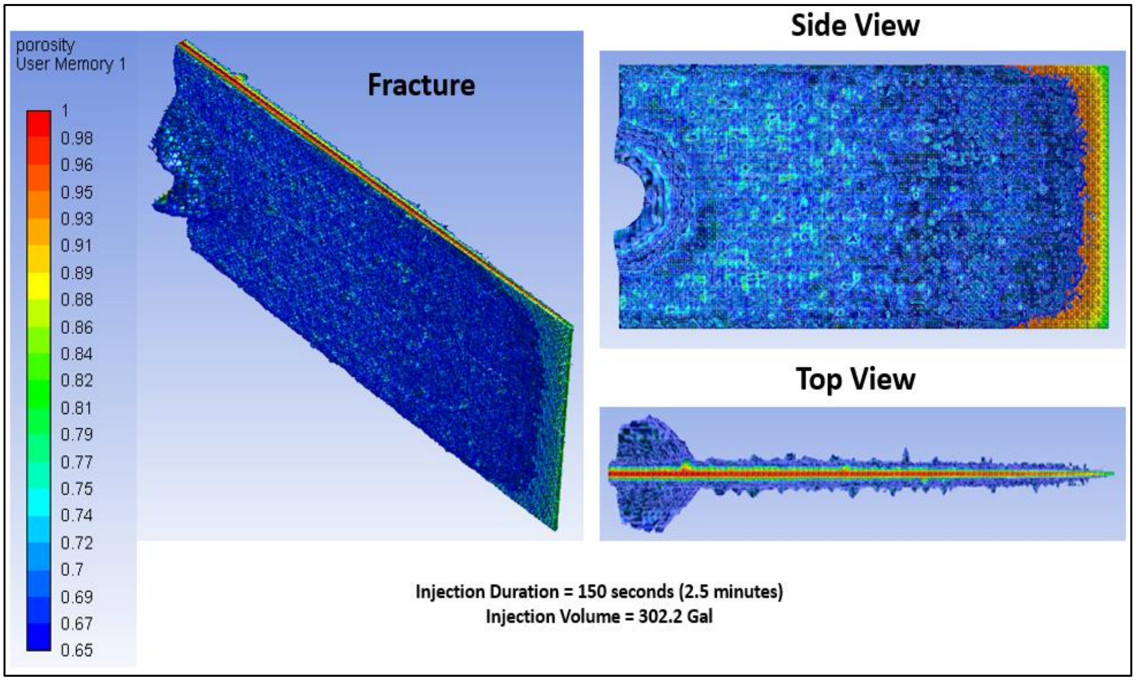

Injection Duration = 150 seconds (2.5 minutes)
Injection Volume = 302.2 Gal

Fig. 5.31 – Wormholes initiation for 28 wt% HCl injected at rate of 120.90 GPM in LPD model.

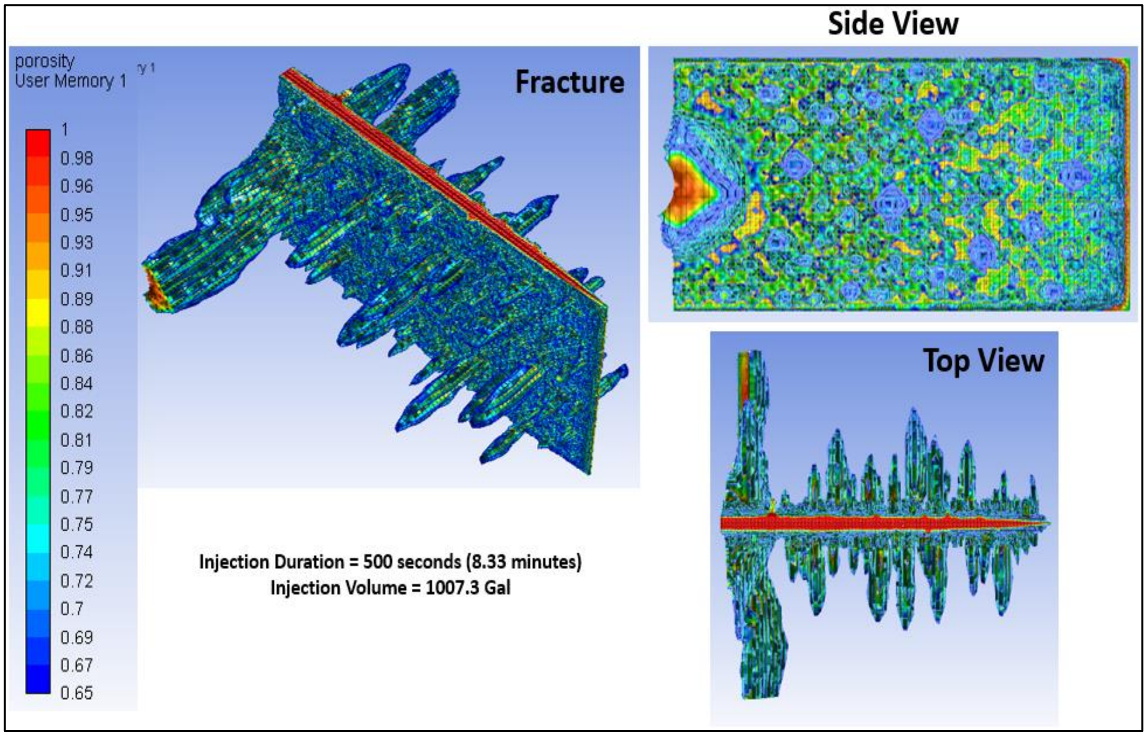

Injection Duration = 500 seconds (8.33 minutes)
Injection Volume = 1007.3 Gal

Fig. 5.32 – Breakthrough state of 28 wt% HCl injected at 120.90 GPM in the LPD model. Reprinted with permission from SPE-191440-18IHFT-MS.

5.6. Effect of Formation Permeability

In the previous sections, HPD and LPD models were discussed separately considering that the acid-fracture is highly conductive in both cases. **Fig. 5.33** shows the pressure profile of both models for 28 wt% HCl demonstrating the onset of wormholes initiation and total injected volume required to breakthrough that can be deduced from the pressure profiles to generate **Fig. 5.35** and **Fig. 5.36**.

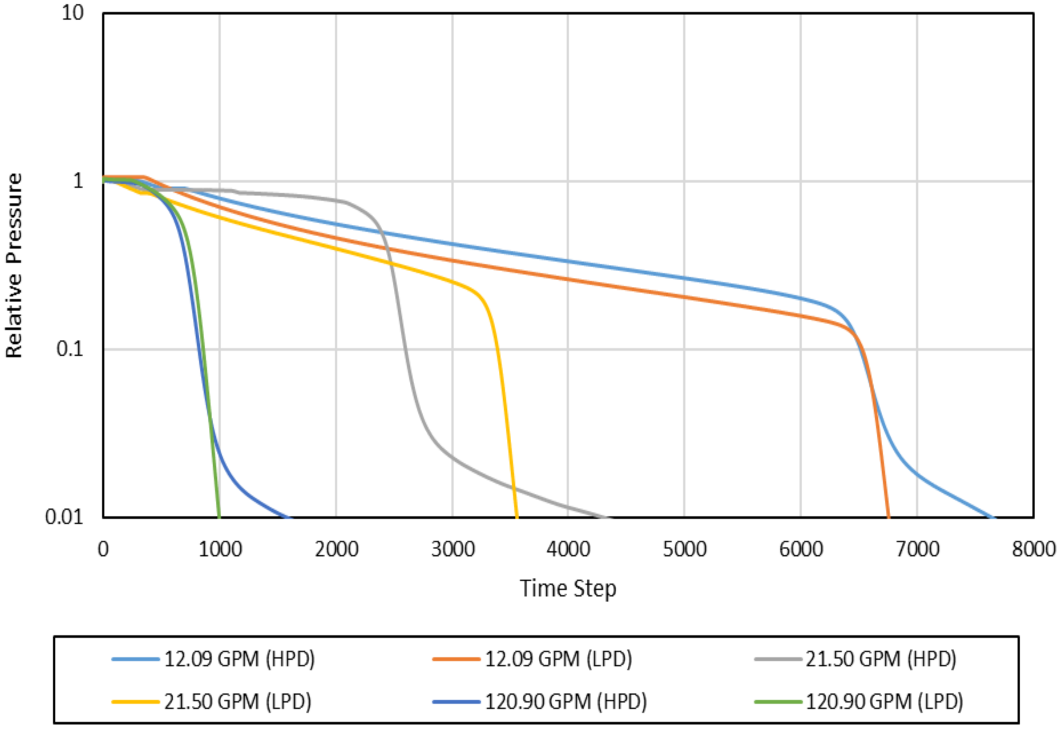

Fig. 5.33 – Pressure Profiles of both High-Permeability Dolomite (HPD) model and Low-Permeability Dolomite (LPD) model for 28 wt% HCl injected at different rates.

Fig. 5.34 demonstrates the performance of HPD model and LPD model using 28 wt% HCl injected at very low rate (2.15 GPM) during CFA operation. The simulation results show the flowing pattern of acid in both cases as the acid is favoring the flow in the fracture in LPD case and it is not propagating and reacting with formation since there is no enough flow momentum to allow the acid to penetrate and react with formation. Unlike the HPD case, the acid is flowing in the fracture while propagating in the formation and reacting with it.

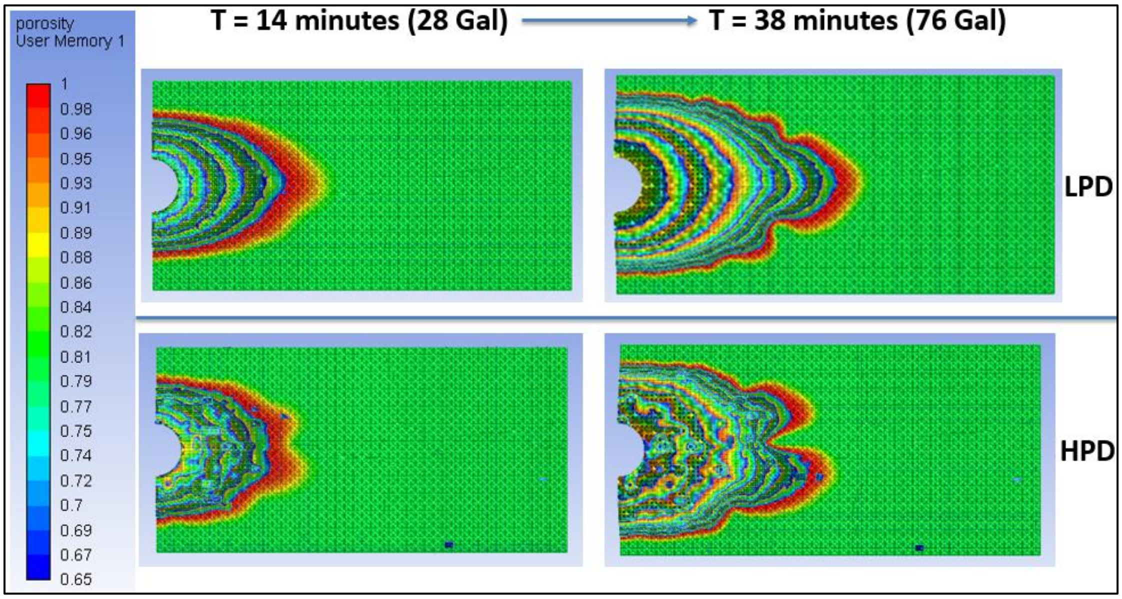

Fig. 5.34 – Comparison between HPD model and LPD model for 28 wt% HCl injected at rate of 2.15 GPM.

Fig. 5.35 shows the total acid volume required to initiate wormholes in both models. It can be noticed that at low to intermediate injection rates, there are no significant difference in the required volume to initiate wormholes, as in these injection rates range, the acid will favor the fracture in the flow since the fracture has high conductivity. However, as the acid injection rate increases, the volume required to initiate wormholes in LPD model is larger than the HPD model because the flow of acid in the formation competes the flow in the fracture in HPD case while it is hard for the acid to flow in tight formation in LPD case and thus, it needs larger volume to initiate wormholes.

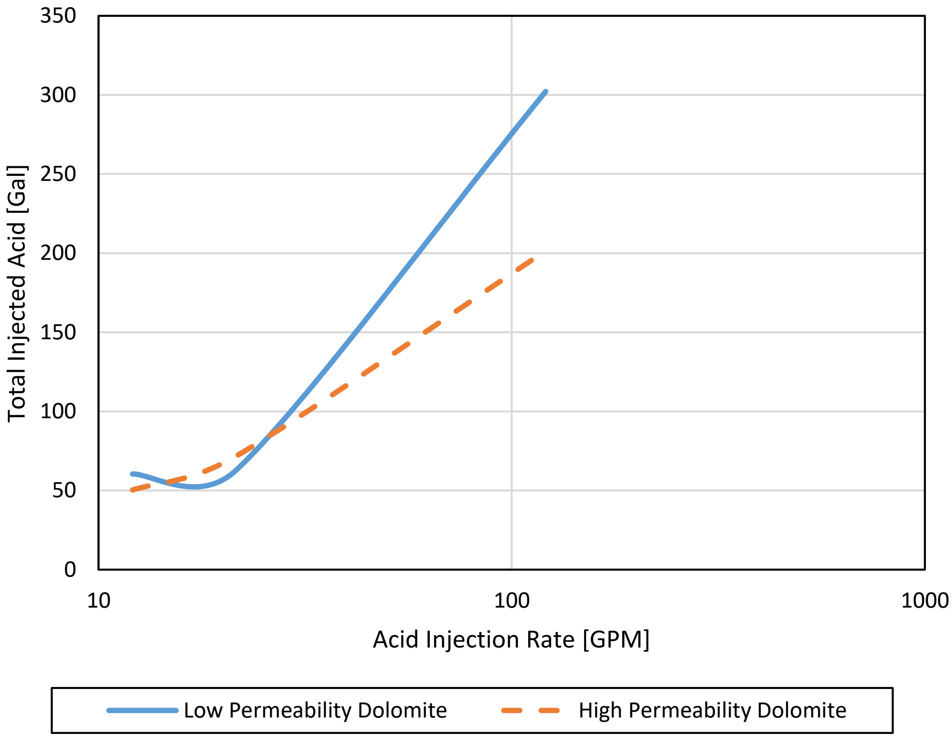

Fig. 5.35 – Wormholes initiation in HPD model and LPD model for 28 wt% HCl injected at different rates.

Fig. 5.36 shows the total volume of injected acid required to breakthrough and it always requires larger volume to breakthrough in HPD case than the volume required to breakthrough in LPD case. Because in HPD case, the acid will generate multiple wormholes along the fracture area and will contribute to grow these wormholes as the flowing proceed which will require large acid volume to grow all these wormholes at the same time until it reaches the breakthrough state. However in the LPD case, the acid will contribute only in the growth of wormholes generated around the injection inlet since the acid flow in the tight dolomite formation is hard and it will only react with the dolomite matrix around the vicinity of injection inlet and will grow these wormholes until it reaches breakthrough state without creating or generating wormholes along the fracture area.

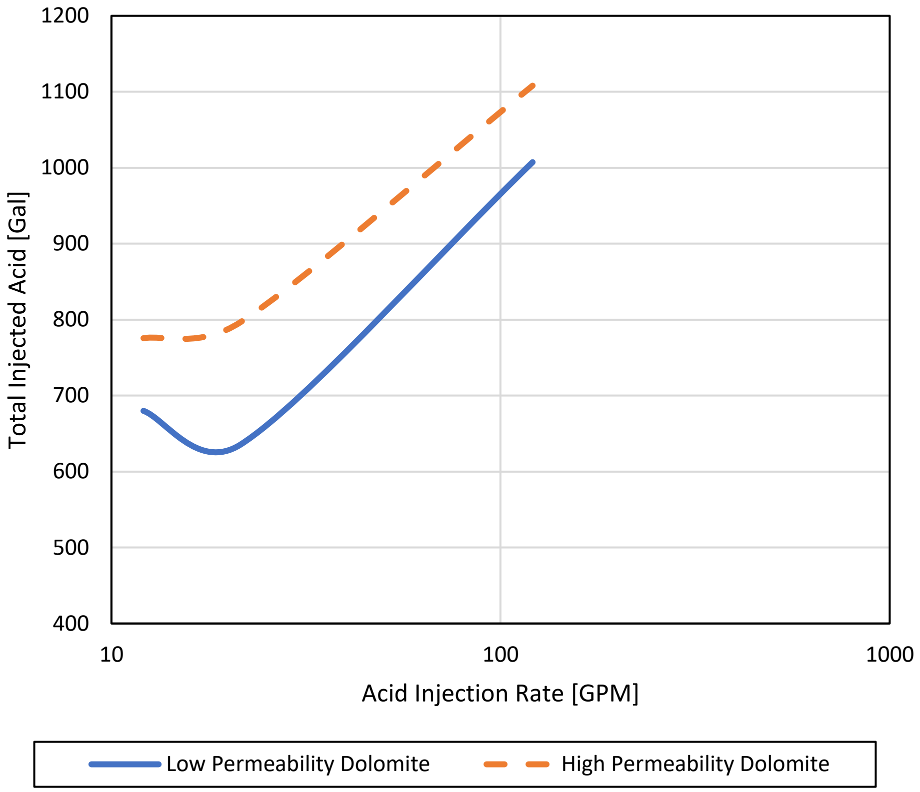

Fig. 5.36 – Total acid volume injected to breakthrough in HPD model and LPD model for 28 wt% HCl injected at different rates. Reprinted with permission from SPE-191440-18IHFT-MS.

5.7. Fracture Conductivity Analysis

In the previous sections, a highly conductive fracture was investigated for all cases which is equal to 2100 md-ft. In this section, three different fracture conductivities are investigated for the LPD model at three acid injection rates which are 12.09 GPM, 21.50 GPM and 120.90 GPM using 28 wt% HCl. The three fracture conductivities are 2100 md-ft, 365 md-ft and 80 md-ft.

Fig. 5.37 shows the pressure profiles of the LPD model illustrating the effect of different fracture conductivities using different injection rates of 28 wt% HCl. It can be noticed from the pressure profiles that the onset of wormholes initiation occurs at the same time for all cases regardless of fracture conductivities. It can also be noticed from the pressure profile that fracture conductivity affects the total acid volume injected to breakthrough for low and intermediate injection rates, but it has no effect on the total acid volume injected to breakthrough for high injection rate.

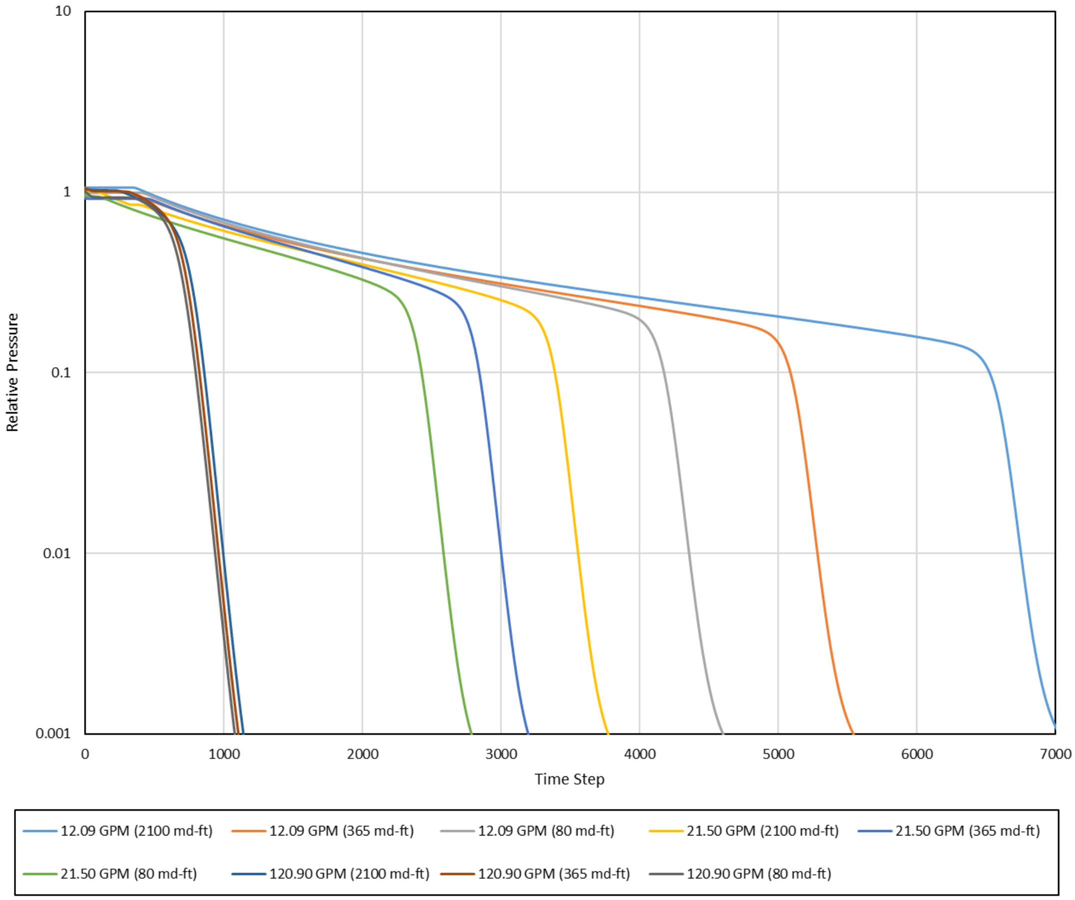

Fig. 5.37 – Pressure profiles of the LPD model illustrating different fracture conductivities and different injection rates of 28 wt% HCl.

For 12.09 GPM injection rate, the wormholes initiation occurs after injecting 60.4 gallons for all fracture conductivities as shown in **Fig. 5.38**. It can be noticed from the figure that acid penetration distance in the fracture decreases with the decrease in fracture conductivity as more acid volumes invade and propagate through formation in low conductivity fracture since the flow in formation competes the flow in the fracture in the case of low conductivity. This behavior promotes significant dissolution and acid-rock reaction around the vicinity of injection inlet which generates extensive wormholes in the area of injection inlet.

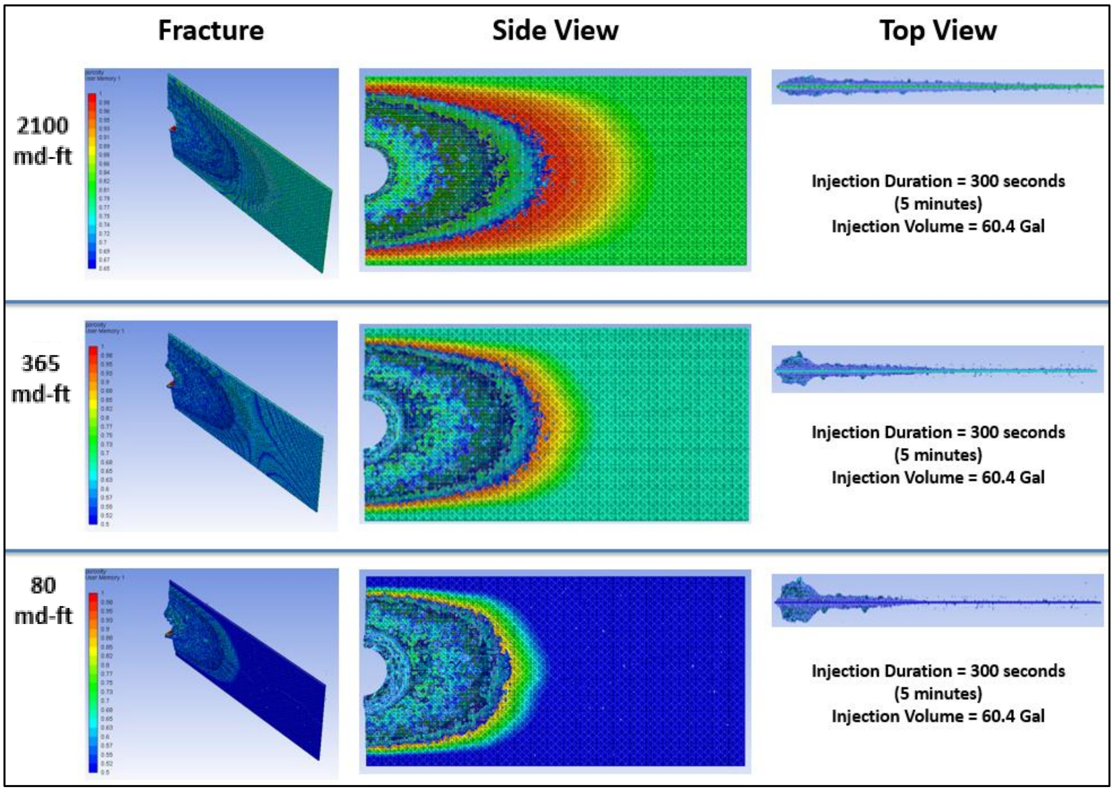

Fig. 5.38 – Wormholes initiation in CFA for 28 wt% HCl injected at rate of 12.09 GPM in LPD model illustrating the effect of different fracture conductivities.

Fig. 5.39 demonstrates the wormholing pattern as the acid is flowing in the fracture before reaching the breakthrough state. It can be noticed that the growth of wormholes is significant in the case of low conductivity fracture in which acid is extending the wormholes that were initiated previously and not stimulating the fracture leaving some areas untouched. However, the acid flows in the fracture and generates smaller wormholes along the fracture area in case of high conductivity fracture.

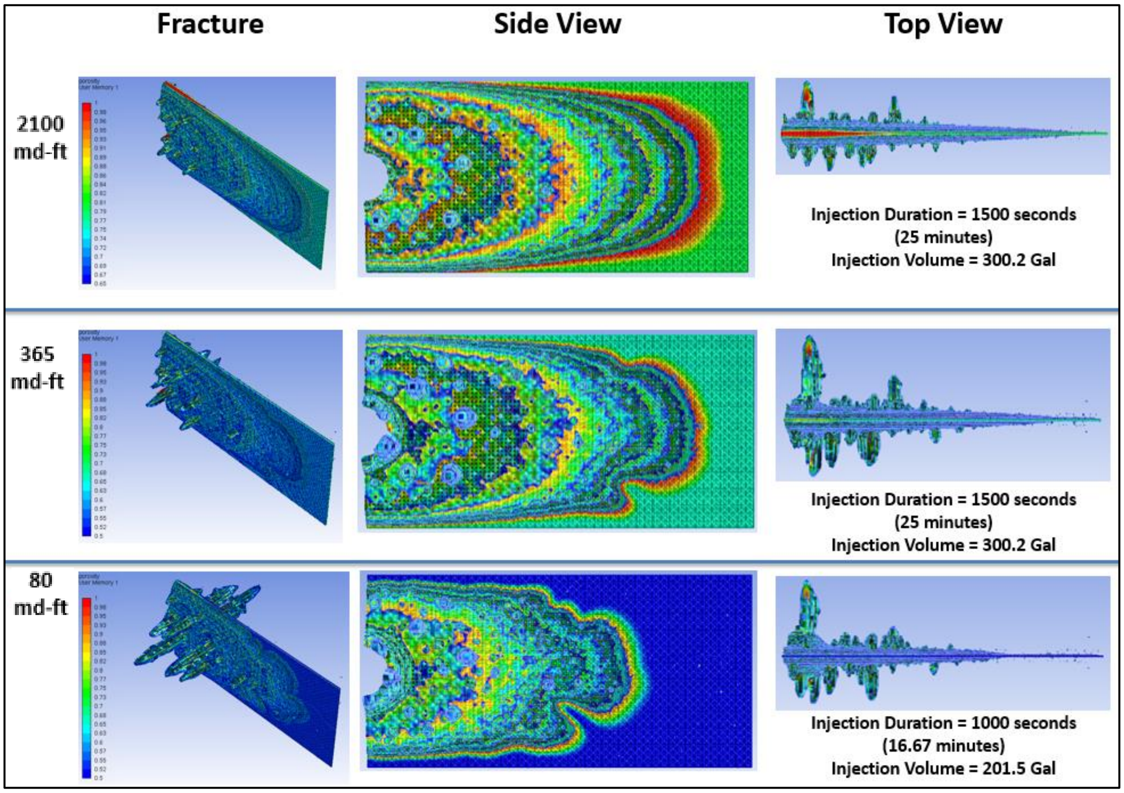

Fig. 5.39 – Acid flow in the fracture and wormholes growth before reaching the state of breakthrough for 12.09 GPM injection rate of 28 wt% HCl in the LPD model illustrating the effect of different fracture conductivities.

At the state of breakthrough, the acid volumes required to breakthrough are 679.9 gallons for 2100 md-ft fracture conductivity, 513.7 gallons for 365 md-ft fracture conductivity and 413 gallons for 80 md-ft fracture conductivity in which the total volume required to breakthrough is decreasing with decrease fracture conductivity as shown in **Fig. 5.40**. It can also be noticed the wormholing density in the case of low conductivity fracture is less than the case of higher conductivities and the acid did not stimulate large portion of the fracture in the case of low conductivity.

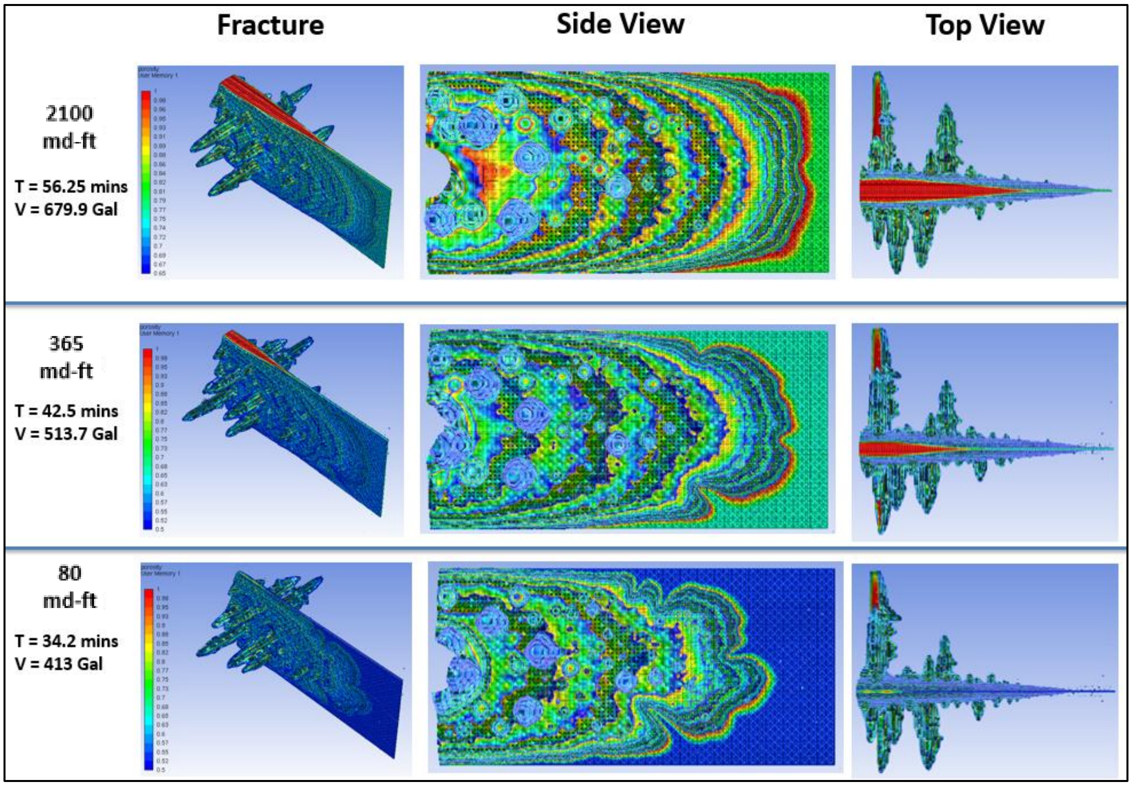

Fig. 5.40 – Breakthrough state of 28 wt% HCl injected at rate of 12.09 GPM in the LPD model illustrating the effect of different fracture conductivities. Reprinted with permission from SPE-191440-18IHFT-MS.

For 21.50 GPM injection rate, the wormholes initiation occurs after injecting 71.63 gallons for all fracture conductivities as shown in **Fig. 5.41**. Acid penetration distance in the fracture is decreasing with decrease fracture conductivity. **Fig. 5.42** demonstrates the wormholing pattern as the acid is flowing in the fracture before reaching the breakthrough state. It can be noticed that acid is greatly contributing to wormholes growth in the case of low conductivity. The direction of wormholes growth is always parallel to the direction of the horizontal well which is perpendicular to the direction of acid flow in the fracture. Extensive dissolution is observed at the injection inlet in the case of 80 md-ft fracture conductivity.

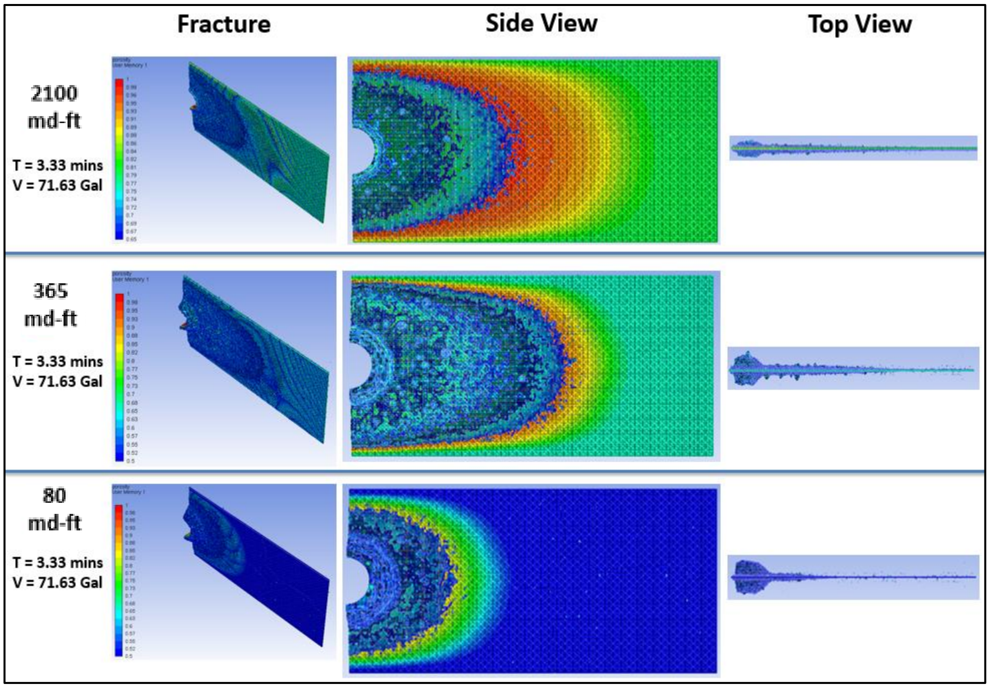

Fig. 5.41 – Wormholes initiation in CFA for 28 wt% HCl injected at rate of 21.50 GPM in LPD model illustrating the effect of different fracture conductivities.

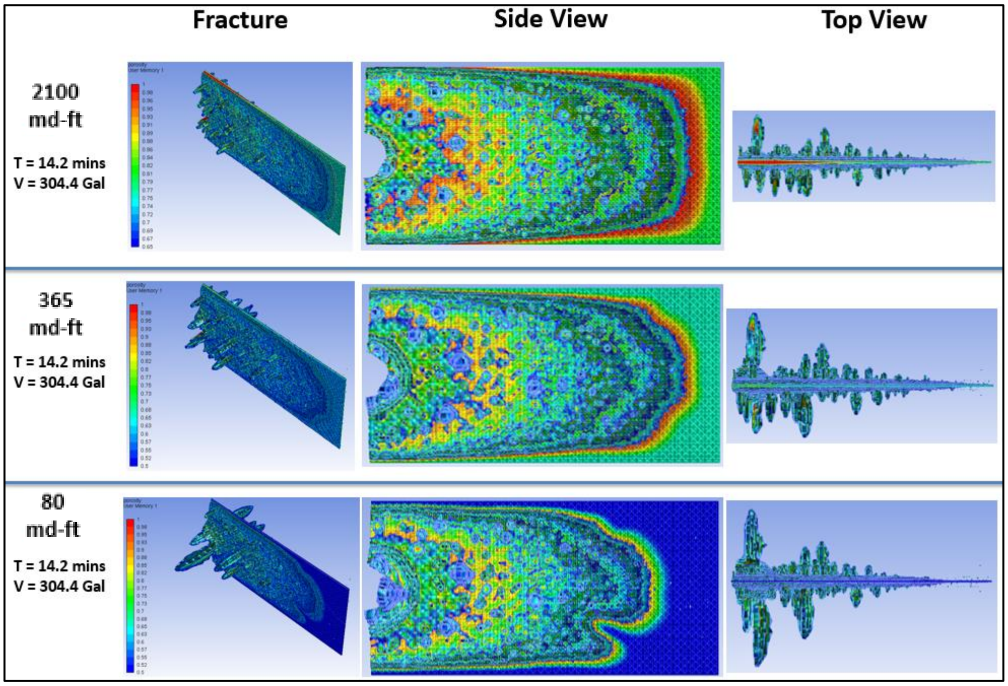

Fig. 5.42 – Acid flow in the fracture and wormholes growth before reaching the state of breakthrough for 21.50 GPM injection rate of 28 wt% HCl in the LPD model illustrating the effect of different fracture conductivities.

At the state of breakthrough, the acid volumes required to breakthrough are 635.7 gallons for 2100 md-ft fracture conductivity, 501.4 gallons for 365 md-ft fracture conductivity and 465.6 gallons for 80 md-ft fracture conductivity in which the total volume required to breakthrough is decreasing with decrease fracture conductivity as shown in **Fig. 5.43**. It can also be noticed in the case of low conductivity fracture that there is large and wide wormhole exist at the injection inlet indicating significant amount of acid has flowed in this wormhole leaving portion of fracture unstimulated.

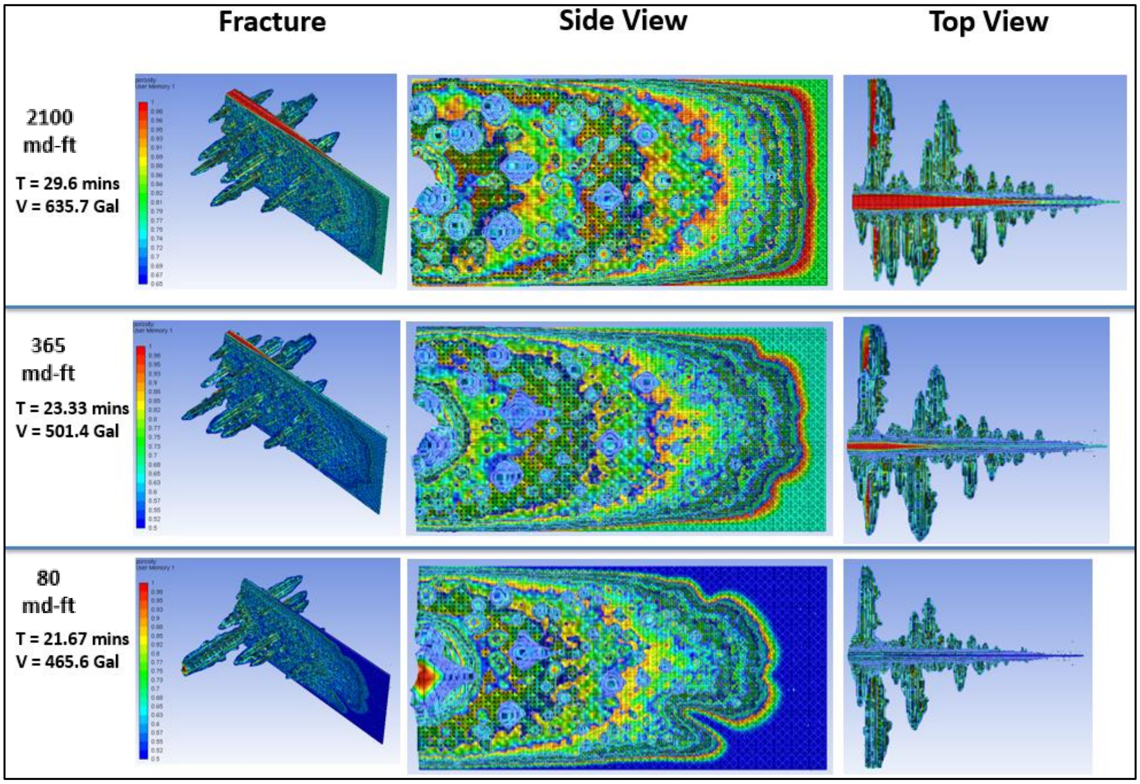

Fig. 5.43 – Breakthrough state of 28 wt% HCl injected at rate of 21.50 GPM in the LPD model illustrating the effect of different fracture conductivities. Reprinted with permission from SPE-191440-18IHFT-MS.

For 120.90 GPM injection rate, the wormholes initiation occurs after injecting 302.2 gallons for all fracture conductivities as shown in **Fig. 5.44**. It can be noticed in all cases that significant dissolution occurs at the injection inlet regardless of fracture conductivities with low conductivity fracture being the largest dissolution.

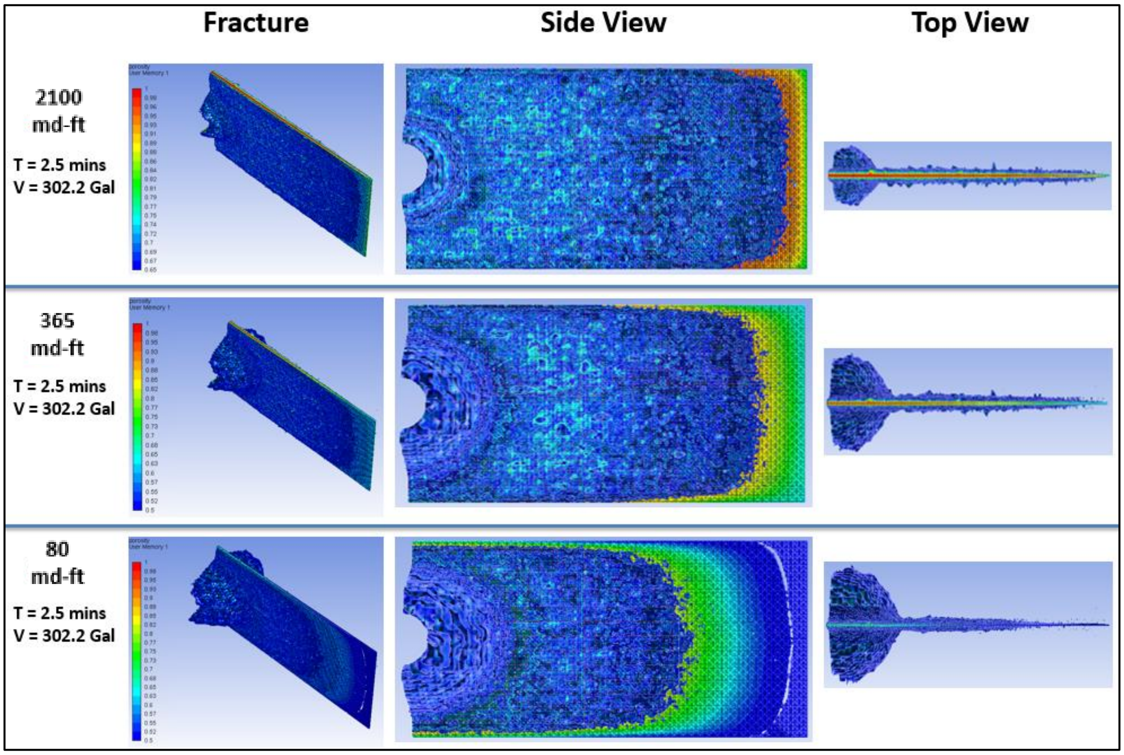

Fig. 5.44 – Wormholes initiation in CFA for 28 wt% HCl injected at rate of 120.90 GPM in LPD model illustrating the effect of different fracture conductivities.

At the state of breakthrough, the acid volume required to breakthrough is 1007.3 gallons for all fracture conductivities since the high flow rate is dominating the dissolution process in which fracture conductivity has minimum effect as shown in **Fig. 5.45**. It can also be noticed in that the wormholing density in the low conductivity fracture is lower that the higher conductivity fracture which indicates significant flow in the formation compared to acid flow in the fracture. There is significant difference between the total injected acid volumes between the cases of 12.09 GPM and 21.50 GPM acid injection rates. However, the total injected acid volumes for the cases of 120.90 GPM acid injection rates have not changed regardless of different fracture conductivities.

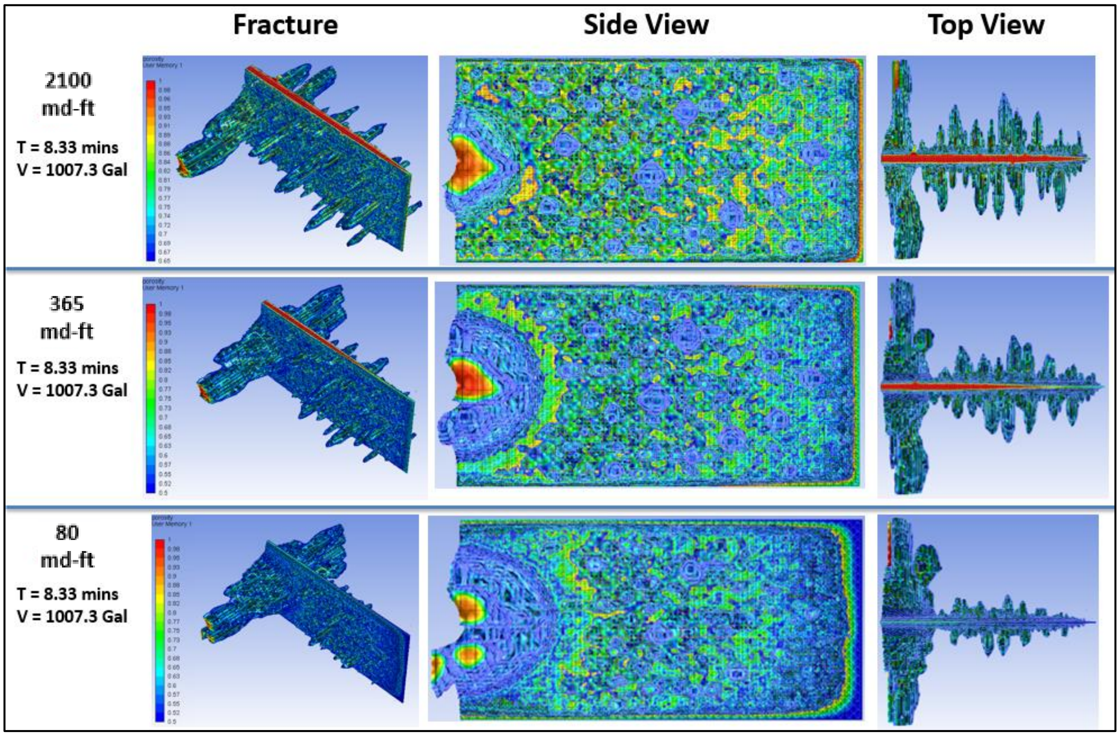

Fig. 5.45 – Breakthrough state of 28 wt% HCl injected at rate of 120.90 GPM in the LPD model illustrating the effect of different fracture conductivities. Reprinted with permission from SPE-191440-18IHFT-MS.

As a conclusion for the effect of fracture conductivity on wormholing during CFA, **Fig. 5.46** demonstrates the effect of fracture conductivity on wormholes initiation for LPD model. It can be noticed that fracture conductivity has no effect on wormholing during CFA as this phenomenon depends solely on the reaction kinetics and diffusion coefficient between the acid system and the formation. It also depends on the formation permeability as shown in **Fig. 5.35** and **Fig. 5.36** since the permeability of formation controls the leakoff of acid in the formation; and hence the wormholing. And since dolomite formation exhibit the reaction-controlled regime due to its extremely low surface reaction rate of HCl-dolomite system, the onset of wormholes initiation requires certain duration of time for the acid to react with the formation and induce the leakoff wormholes.

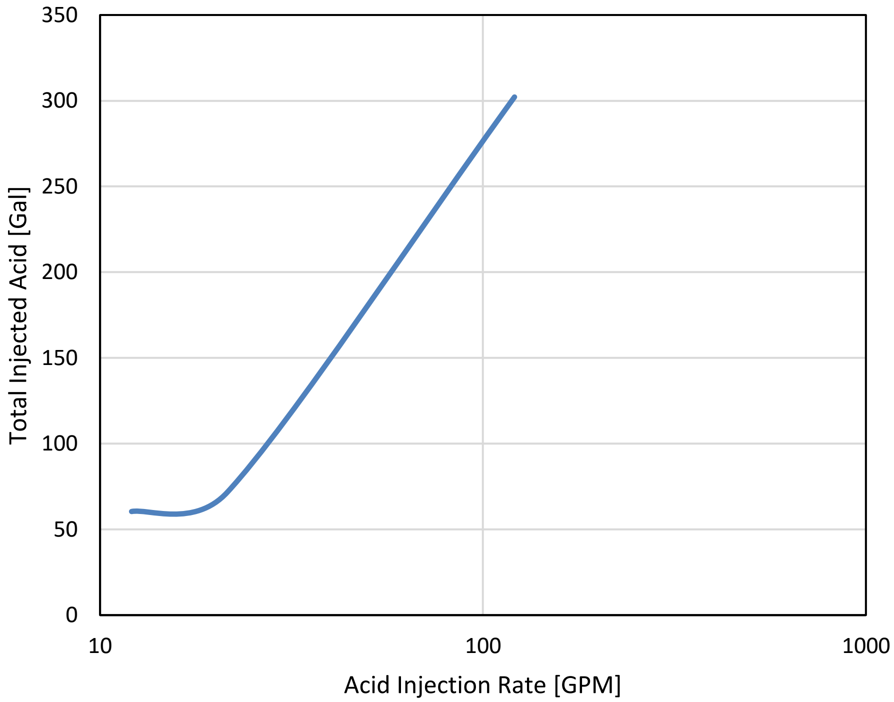

Fig. 5.46 – Wormholes initiation in LPD model for 28 wt% HCl injected at different rates and for all fracture conductivities.

Fig. 5.47 demonstrates the effect of different fracture conductivities on the acid volume injected to breakthrough in LPD model. At low injection rates, low fracture conductivity (80 md-ft) promotes extensive flow of acid in the formation which generates a single dominant wormhole with large diameter around the injection inlet, and that wormhole extends in the formation until the acid reaches the breakthrough state leaving significant portion of the fracture unstimulated. However, high conductivity fracture (2100 md-ft) allows the acid to prioritize the fracture in the flow which generates smaller wormholes along the fracture area and that required larger volumes of acid to be injected in order for the acid to grow the small wormholes and propagate through formation to reach the breakthrough state. At high acid injection rates, the flow force is too high for the acid to flow in the fracture and formation equally without prioritizing the fracture or formation even in low conductivity fracture which gives the same required acid volume injected to breakthrough. It is important to highlight that fracture conductivity has significant effect on wormholing density. For low conductivity fracture, only single dominant wormhole was generated that grows to reach the boundaries of model. But for high conductivities, wormholes are generated and distributed along the fracture area indicating significant flow of acid in the fracture.

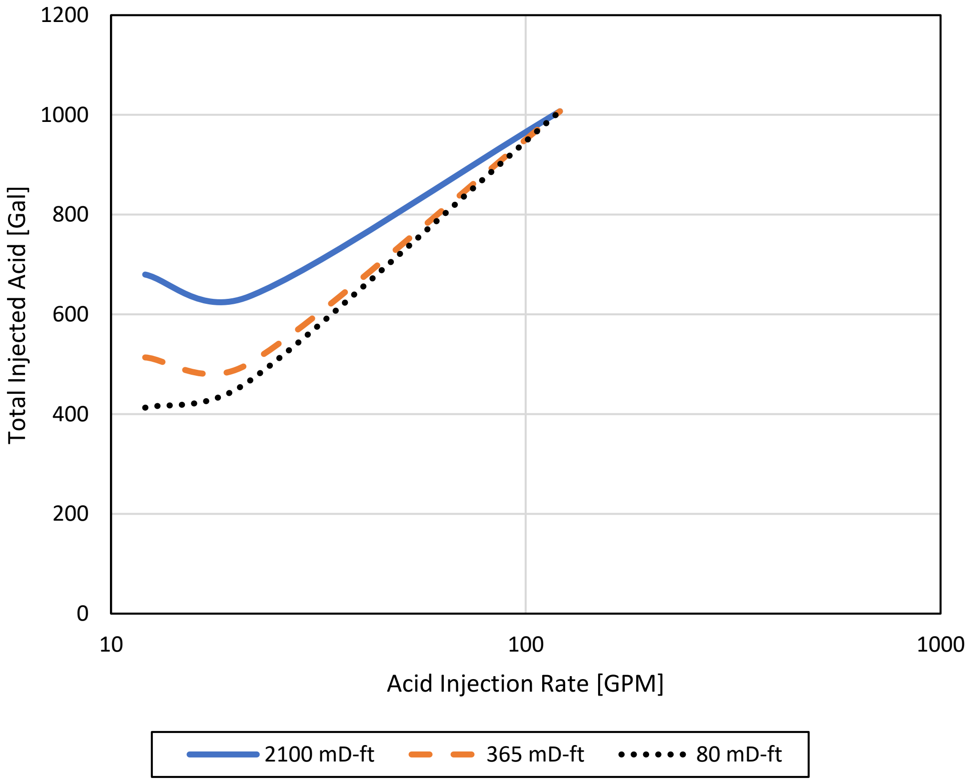

Fig. 5.47 – Total acid volume injected to breakthrough in LPD model for 28 wt% HCl injected at different rates illustrating the effect of different fracture conductivities. Reprinted with permission from SPE-191440-18IHFT-MS.

5.8. Effect of Natural Fractures

A total of six natural fractures were imposed in the model with same aperture and very high conductivity (1,576,258 md-ft). Two models were developed to study the effect of different natural fractures orientations with respect to the acid-fracture as shown in **Fig. 5.48**.

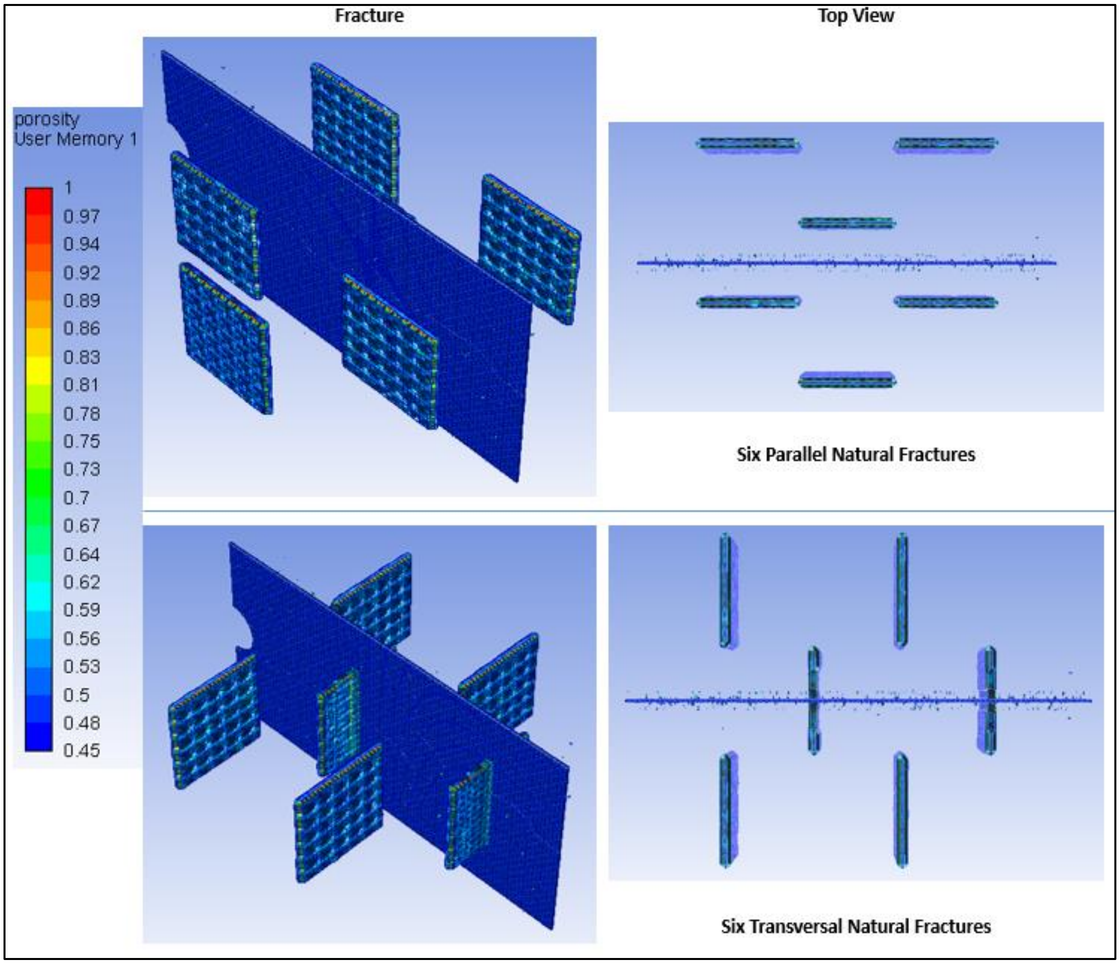

Fig. 5.48 – Two LPD models with 80 md-ft acid-fracture conductivity illustrating six parallel natural fracture (upper) and six transversal natural fractures (lower). Reprinted with permission from SPE-191440-18IHFT-MS.

Three different acid injection rates were used in these two models and the generated pressure profile in **Fig. 5.49** shows the results of the simulation runs by the two natural fractures models in addition to the base case that was studied in the previous section. The base model is the horizontal well LPD model with 80 md-ft acid-fracture conductivity with no natural fractures existing in the model. The pressure profile indicates that natural fractures have no effect on wormholes initiation in the model as the pressure profile trend of the two natural fractures models follows the same trend as the one in the base case. However, natural fractures affect the total acid volumes required to breakthrough and to penetrate certain distance in the model as shown in the intersection of pressure profile with 0.01 relative pressure.

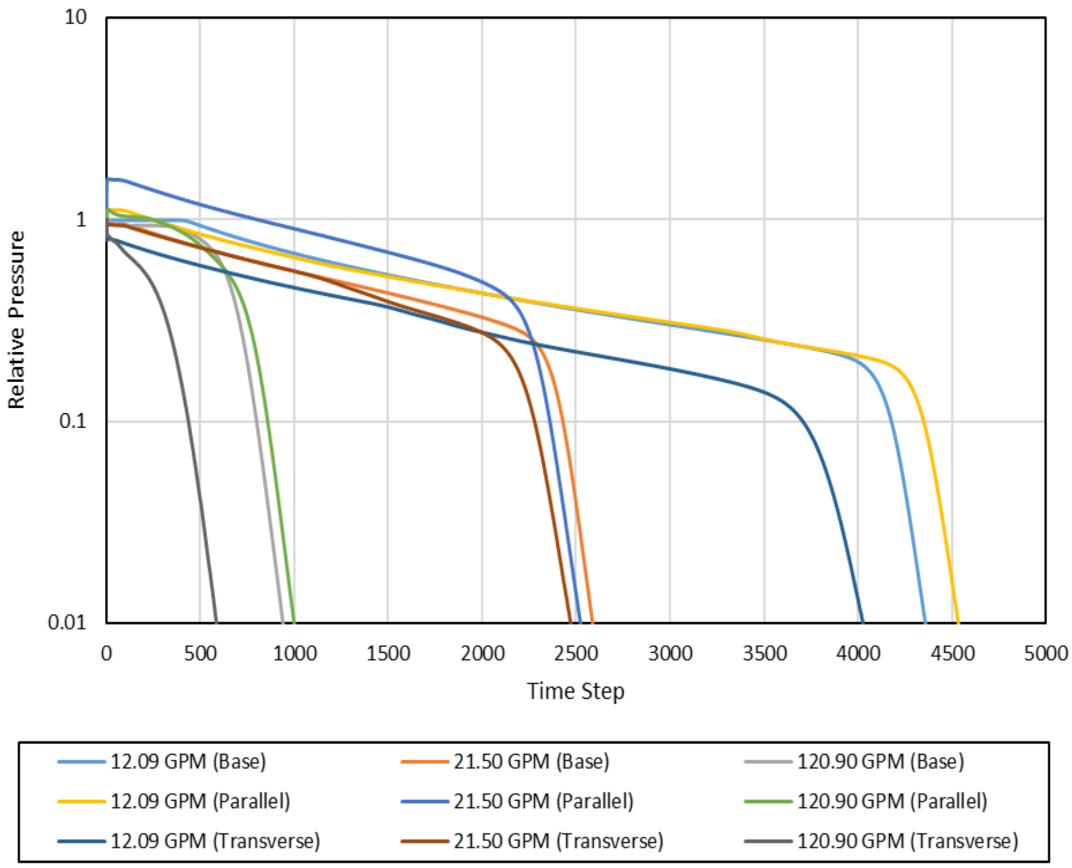

Fig. 5.49 – Pressure profiles of the two natural fractures models and the base model.

At 12.09 GPM injection rate, **Fig. 5.50** demonstrates the acid flow pattern in the acid-fracture and in the presence of natural fractures with different orientations after an injection time of 16.67 minutes. Acid leakoff takes place around the vicinity of injection inlet regardless on the existence of natural fractures, and whether they are parallel or intersecting with the acid-fracture.

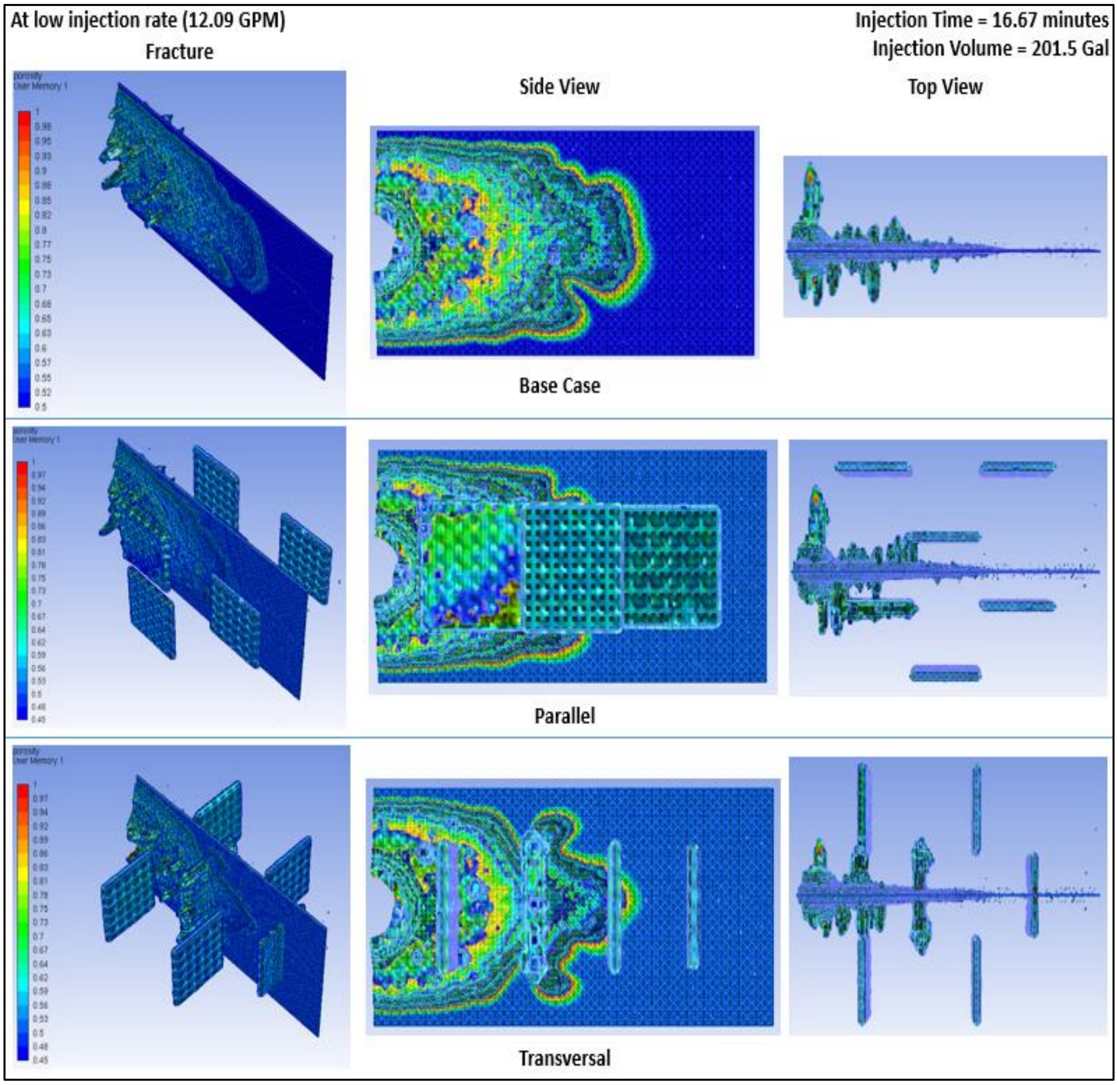

Fig. 5.50 – Acid flow in the two natural fractures models before reaching breakthrough state for 28 wt% HCl injected at 12.09 GPM acid injection rate.

Fig. 5.51 demonstrates the state of breakthrough for the two models (parallel and transversal natural fractures) as the total acid volumes required to breakthrough are 413.1 gallons for the base case, 453.4 gallons for parallel natural fractures and 388 gallons for transversal natural fractures. It can be observed that natural fractures which are parallel with the acid-fracture interfered with the flow and spending of acid as it required more injected volume to breakthrough than the base case. Because once the wormholes establish connection between the acid-fracture and natural fracture, acid will start to flow directly to the natural fracture and start to be consumed in stimulating the natural fractures leaving a considerable portion of acid-fracture unstimulated. However, it required fewer acid volumes in the case of transversal natural fractures as they assisted the acid flow to reach the model boundaries in a faster manner. It can be noticed in the case of transversal natural fractures that the intersected natural fracture did not control leak-off and does not prevent acid leak-off in the formation as the acid was able to establish connection with the two natural fractures that were located near the injection inlet which also happened to be the reason for not creating dominant and large wormholes around the injection inlet as in the base case shown in **Fig. 5.51**. In both natural fractures models, wormholing density has reduced significantly in the case of transversal natural fractures than the case of parallel natural fractures indicating that natural fractures have dominant effect and control in the flow of acid in the formation. Also, the far distant natural fractures from the injection inlet were left untouched by the acid as the close natural fractures took most of acid volumes creating flow networks between the acid-fracture and natural fractures from the acid spending in these natural fractures.

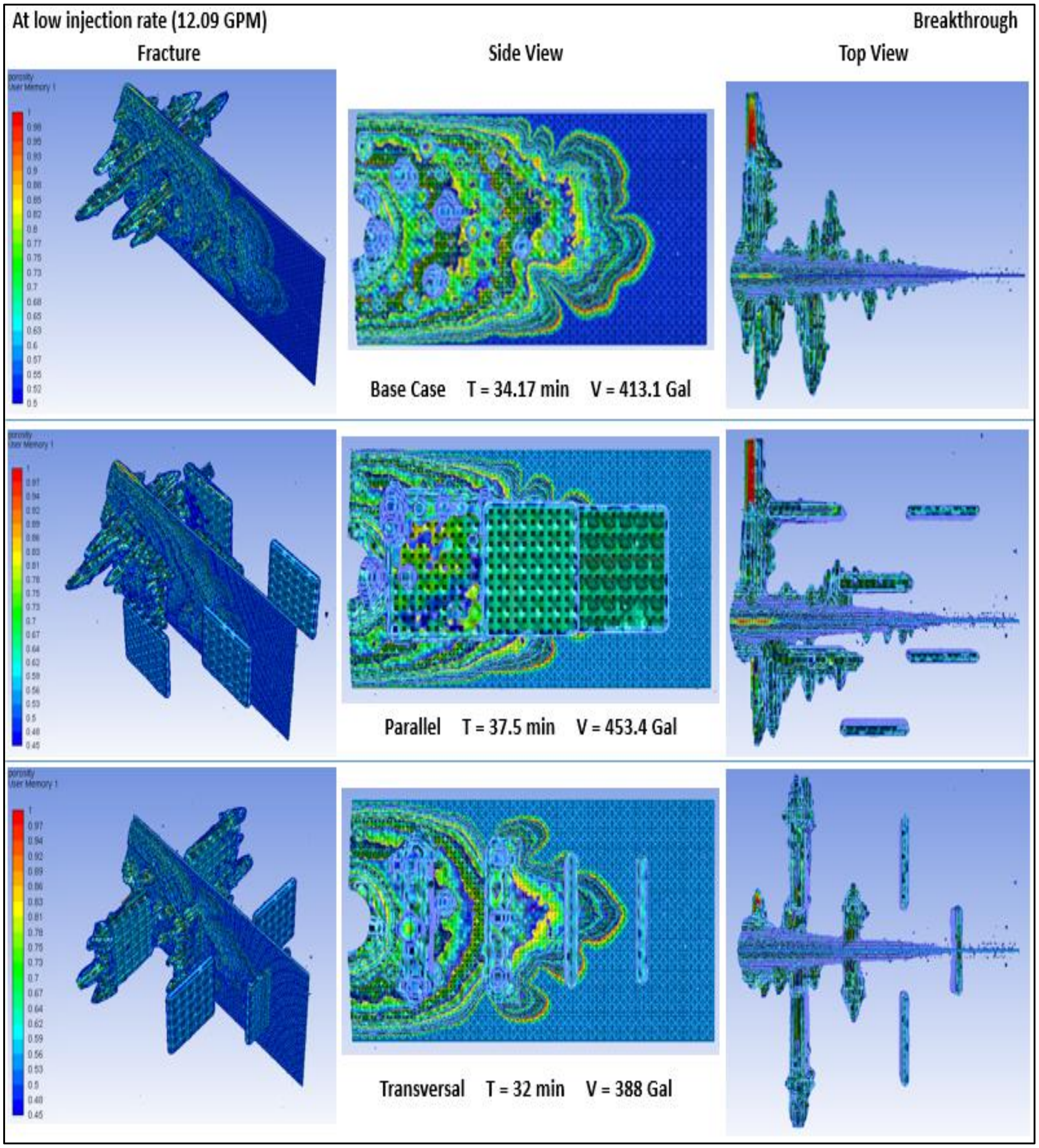

Fig. 5.51 – The state of breakthrough for the parallel and transversal natural fractures models after injecting 28 wt% HCl at 12.09 GPM injection rate. Reprinted with permission from SPE-191440-18IHFT-MS.

For 21.50 GPM injection rate, **Fig. 5.52** demonstrates the acid flow pattern in the acid-fracture and in the presence of natural fractures with different orientations after an injection time of 14.17 minutes. The same observation can be drawn regarding the acid leakoff around the vicinity of injection inlet that took place in the case of 12.09 GPM acid injection rate. In this case, the acid injection rate was relatively higher than the acid injection rate used in the previous case, and so establishing flow network between the acid-fracture and natural fractures was faster and more efficient than the previous case.

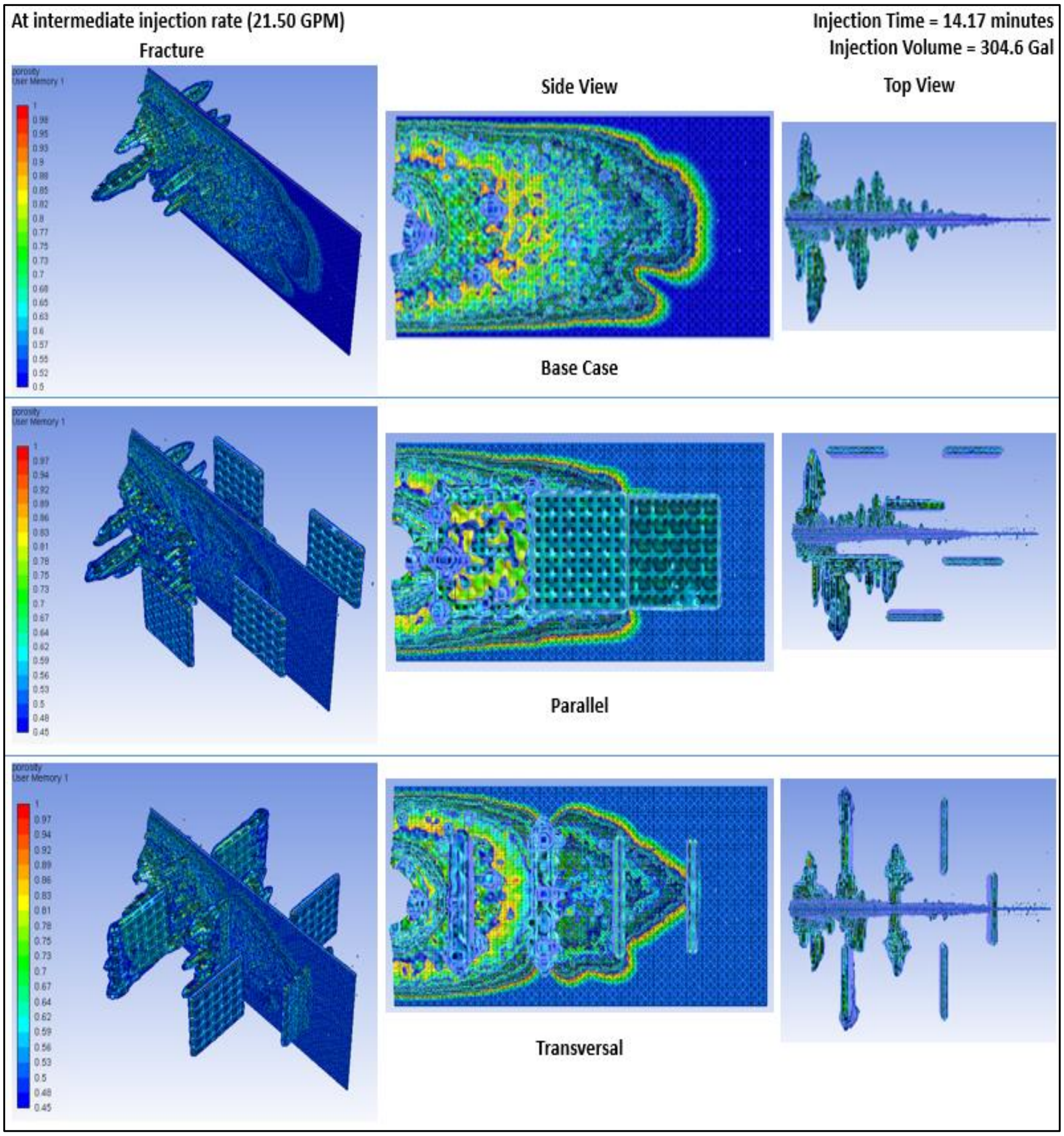

Fig. 5.52 – Acid flow in the two natural fractures models before reaching breakthrough state for 28 wt% HCl injected at 21.50 GPM acid injection rate.

Fig. 5.53 demonstrates the state of breakthrough for the two natural fractures models as the total acid volume required to breakthrough is 465.8 gallons for the base case, 430 gallons for parallel natural fractures and 394.2 gallons for transversal natural fractures. In the case of parallel natural fractures, higher injection rate promotes faster connection between the acid-fracture and the nearest natural fracture located around the injection inlet which created a dominant flow network for the acid to flow through it and propagate in the formation to reach the boundaries of the model with minimum flowing distance which yielded lower volume required to breakthrough than the base case as a result of this flowing and dissolution pattern. In the case of transversal natural fractures, the phenomenon here is similar to what took place in the case of 12.09 GPM injection rate as the acid established permeable connection between the acid-fracture and the nearest natural fractures located around the injection inlet in which their transversal direction assisted the acid to flow toward the breakthrough boundaries which yields the lowest required volume to breakthrough. Wormholing density has decreased in the natural fractures cases with the transversal one being the minimum density. Although the injection rate has increased from the previous case, the intersected natural fractures in the transversal case did not prevent acid leak-off from the acid-fracture and the acid was able to induce wormholes that established connection between the acid-fracture and the natural fractures which created dominant flow networks as a result.

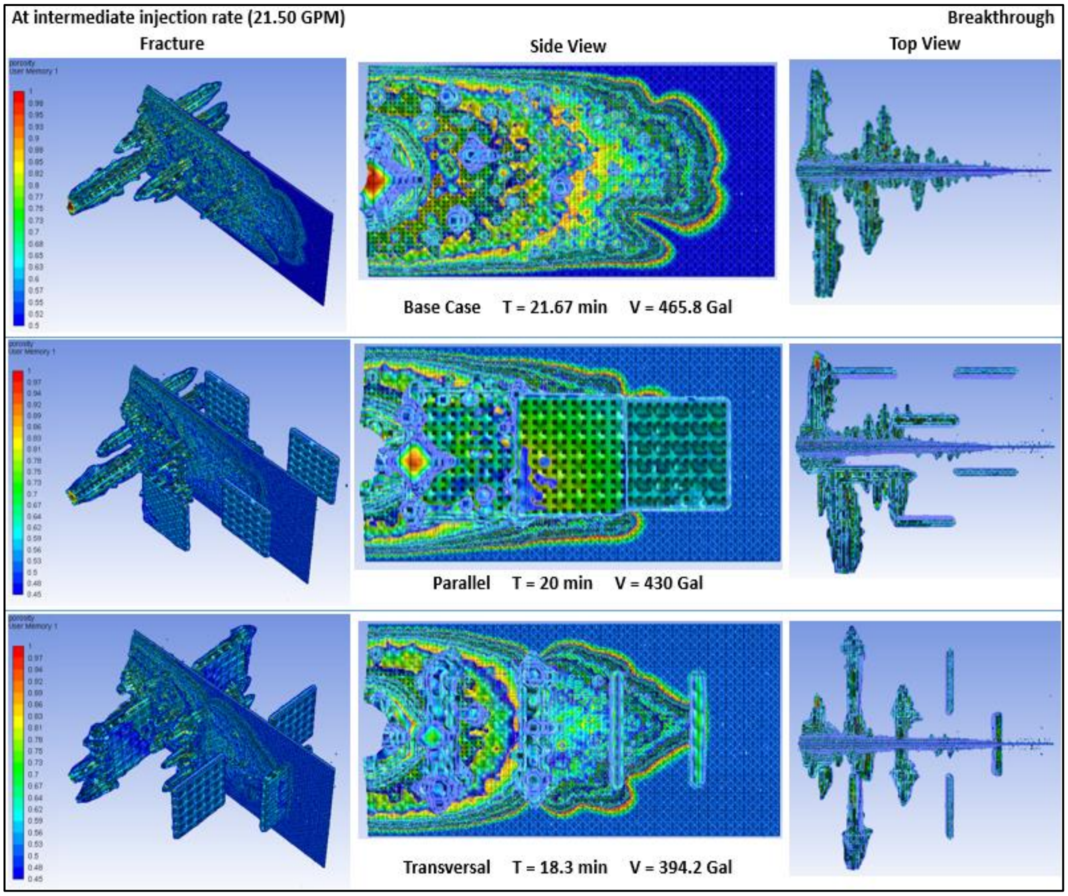

Fig. 5.53 – The state of breakthrough for the parallel and transversal natural fractures models after injecting 28 wt% HCl at 21.50 GPM injection rate. Reprinted with permission from SPE-191440-18IHFT-MS.

At 120.90 GPM injection rate, **Fig. 5.54** demonstrates the state of breakthrough for the two natural fractures models as the acid volumes required to breakthrough are 1007.5 gallons for the base case, 1007.5 gallons for parallel natural fractures and 554 gallons for transversal natural fractures. In the case of parallel natural fractures, the high flow rate promotes significant acid leakoff in which the acid was able to establish connection between the acid-fracture and the nearest four natural fractures around the injection inlet, this acid flow pattern and dissolution phenomena creates a large flow network which required relatively larger acid volume to reach the model boundaries and that is the reason of the same volume of acid required to breakthrough in the base case and parallel natural fractures case. The configuration of natural fractures in this case have a significant role in controlling the flow of acid in the formation. However, unlike the parallel case in which the acid-fracture is connected with four natural fractures, the acid established connection with only two natural fractures in the transversal case as the very high rate allows the acid to flow to the nearest two natural fracturing in which their direction assisted the acid to reach the boundaries faster than the base case and the parallel case. And again, the same observation can be drawn for both acid leakoff and wormholing phenomena.

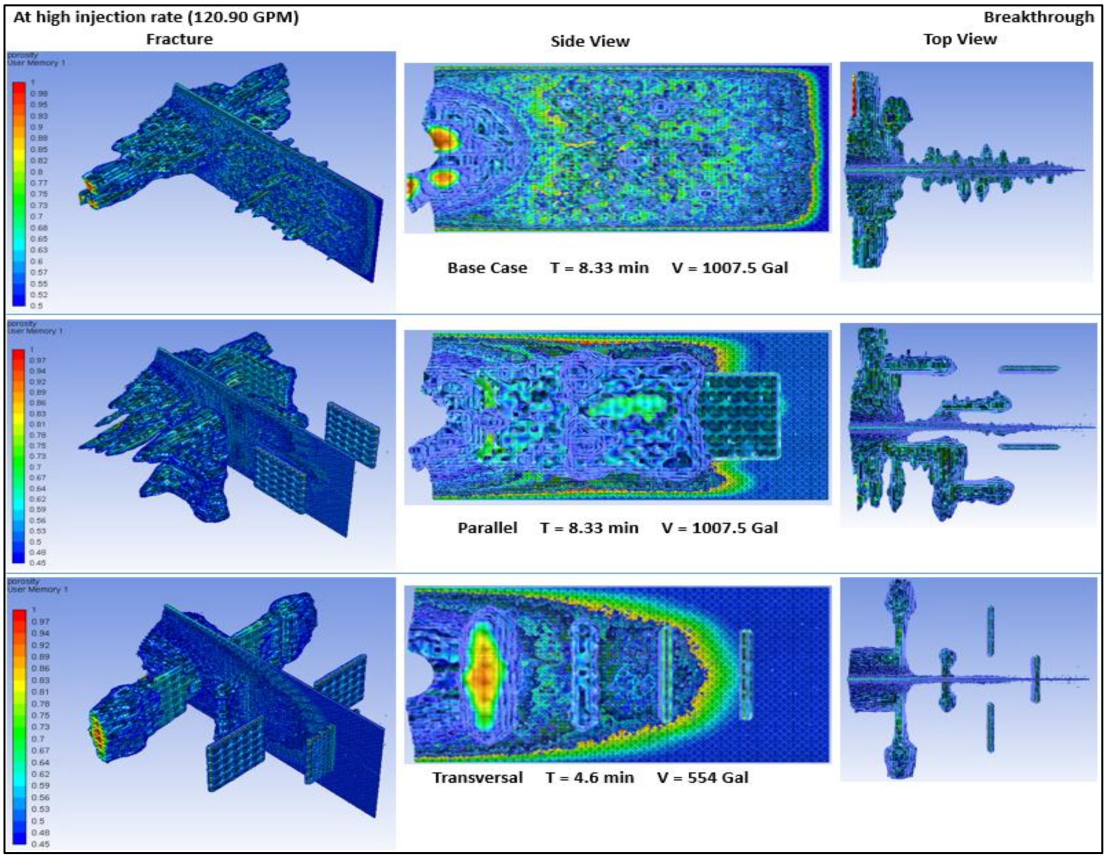

Fig. 5.54 – The state of breakthrough for the parallel and transversal natural fractures models after injecting 28 wt% HCl at 120.90 GPM injection rate. Reprinted with permission from SPE-191440-18IHFT-MS.

Fig. 5.55 summarizes the effect of natural fractures presence and orientation on the total volume of acid required to breakthrough. At low injection rate, natural fractures that are parallel to the hydraulic fracture will control the flow of acid significantly as the direction of acid flow in the formation is perpendicular to this flow of acid in the natural fractures and this will require more acid volume to reach the breakthrough state, but in the transversal natural fractures, the natural fractures will assist the acid to flow in the same direction in the formation and will reach the model boundaries faster than the base case and parallel natural fractures case which will require less acid volume as a result. At the intermediate injection rate, the flow forces will allow the acid to propagate through tight dolomite and establish a connection with the nearest natural fracture in which the direction of the flow in natural fractures will not affect the acid flow in the formation as a result of the high momentum which will allow the acid to breakthrough with less volume required than the base case. However, the flow forces are not highly dominant in the intermediate injection rates as in the case of very high injection rate in which the acid establishes a connection with greater number of natural fractures that yields larger volume required to breakthrough in the case of high injection rates and parallel natural fractures. In the case of intermediate injection rate and parallel natural fractures, acid was able to establish connection with one natural fracture and that network became the dominant one in the flow. In the transversal natural fractures, it is always required less acid volume to breakthrough is the direction of these natural fracture align with the original direction of acid flow in the formation. It can also be concluded that the presence of natural fractures has reduced the wormholing density at the state of breakthrough, this effect coupled with the orientation of natural fractures as it is always minimum wormholing density in the case of transversal natural fractures. Lastly, natural fractures that intersect the acid-fracture does not control acid leakoff or prevent acid flow in the formation since the most important factor that plays a key role in this phenomenon is the location of natural fractures with respect to the acid-fracture and its injection inlet. Natural fractures that are located near the injection inlet assist the acid in the flow which allow the acid to create dominant flow networks between the acid-fracture and natural fractures as the acid dissolution proceeds.

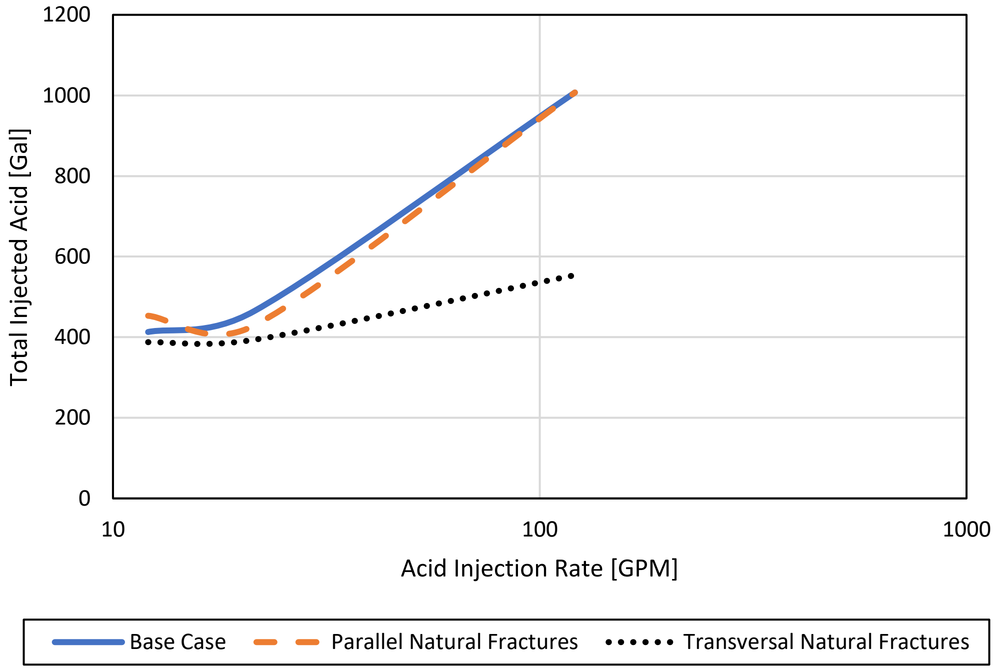

Fig. 5.55 – Total acid volume injected to breakthrough in parallel and transversal natural fractures models for 28 wt% HCl injected at different rates. Reprinted with permission from SPE-191440-18IHFT-MS.

5.9. Effect of Model Upscaling

Upscaling the computational fluid dynamics model highlights the effect of acid womholing in an actual field scale during CFA operation. The model is upscaled by a factor 10 and the new dimensions of the model are 2 meters length, 2 meters width and 1 meter height. Acid injection rates in the upscaled model are 12.09 GPM, 21.50 GPM and 120.90 GPM which are similar to the base case. The base model is the horizontal well LPD model with 80 md-ft acid-fracture conductivity. **Fig. 5.56** demonstrates the state of breakthrough for the upscaled model after injecting 28 wt% HCl at 12.09 GPM injection rate. The total acid volume required to breakthrough for the low injection rate case is 413.1 gallons for the base model and 1798 gallons for the upscaled model. The upscaling factor for the total injected volume is 4.35. It can be noticed that the acid generated only three dominant wormholes in the upscaled model that propagated and extended toward the model boundaries unlike the base model where there are several wormholes appeared on the fracture walls. Also, significant fracture area left unstimulated at the breakthrough state indicating extensive acid leakoff in the formation.

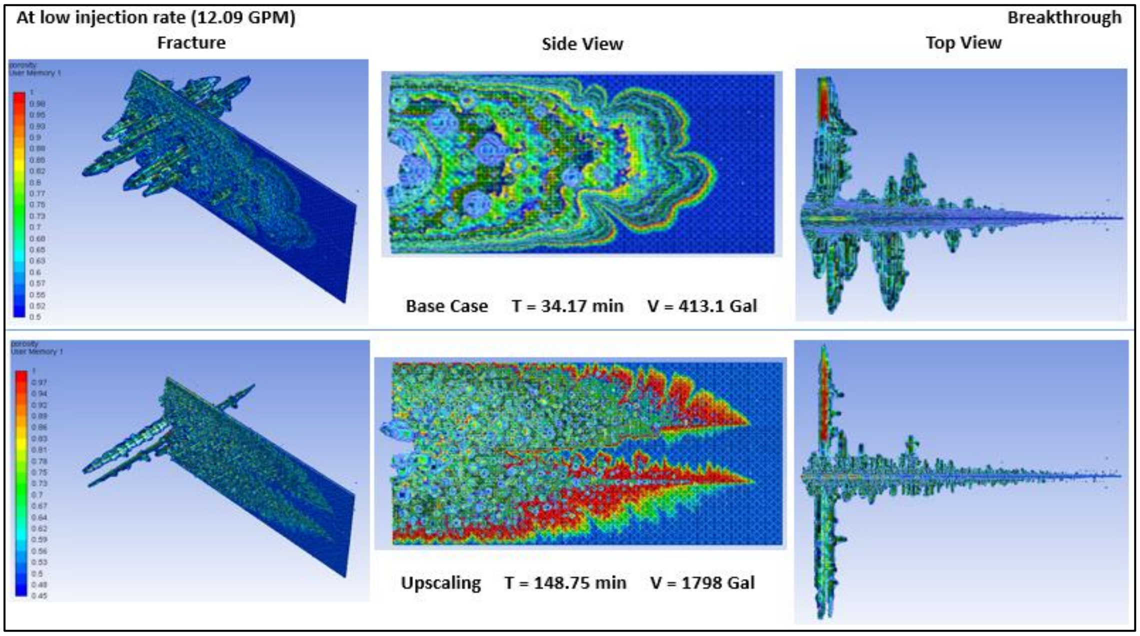

Fig. 5.56 – The state of breakthrough for the upscaled model after injecting 28 wt% HCl at 12.09 GPM injection rate. Reprinted with permission from SPE-191440-18IHFT-MS.

Fig. 5.57 demonstrates the state of breakthrough for the upscaled model after injecting 28 wt% HCl at 21.50 GPM injection rate. The total acid volume required to breakthrough for the intermediate injection rate case is 465.8 gallons for the base model and 2166.8 gallons for the upscaled model. The upscaling factor for the total injected volume is 4.65. The dissolution pattern and the wormholing phenomena in the upscaled model is approximately similar to the pattern existed in the base model, in which a single dominant wormhole is propagating from the fracture and extending toward the boundaries of model. Also, wormholing density and acid penetration distance in the fracture are approximately equal in both cases.

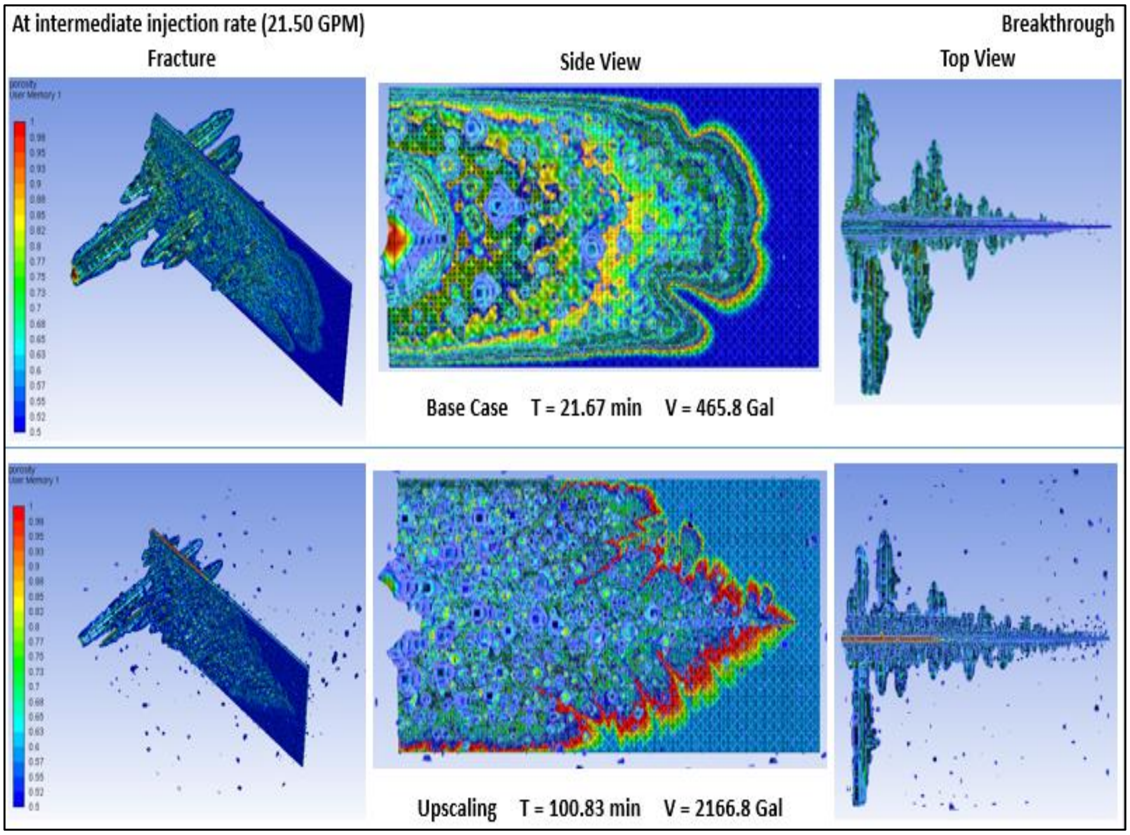

Fig. 5.57 – The state of breakthrough for the upscaled model after injecting 28 wt% HCl at 21.50 GPM injection rate. Reprinted with permission from SPE-191440-18IHFT-MS.

Fig. 5.58 demonstrates the state of breakthrough for the upscaled model after injecting 28 wt% HCl at 120.90 GPM injection rate. The total acid volume required to breakthrough for the high injection rate case is 1007.5 gallons for the base model and 3021.9 gallons for the upscaled model. The upscaling factor for the total injected volume is 3. The dissolution pattern and womholing phenomenon in the upscaled model is different from the one in the base model in which several dominant wormholes are evenly distributed across the fracture area in the upscaled model, while only one single and large wormhole is propagating from the fracture in the base model. Wormholing density is larger in this case and the acid was able to travel long distance in the fracture which generates several wormholes along its flow path.

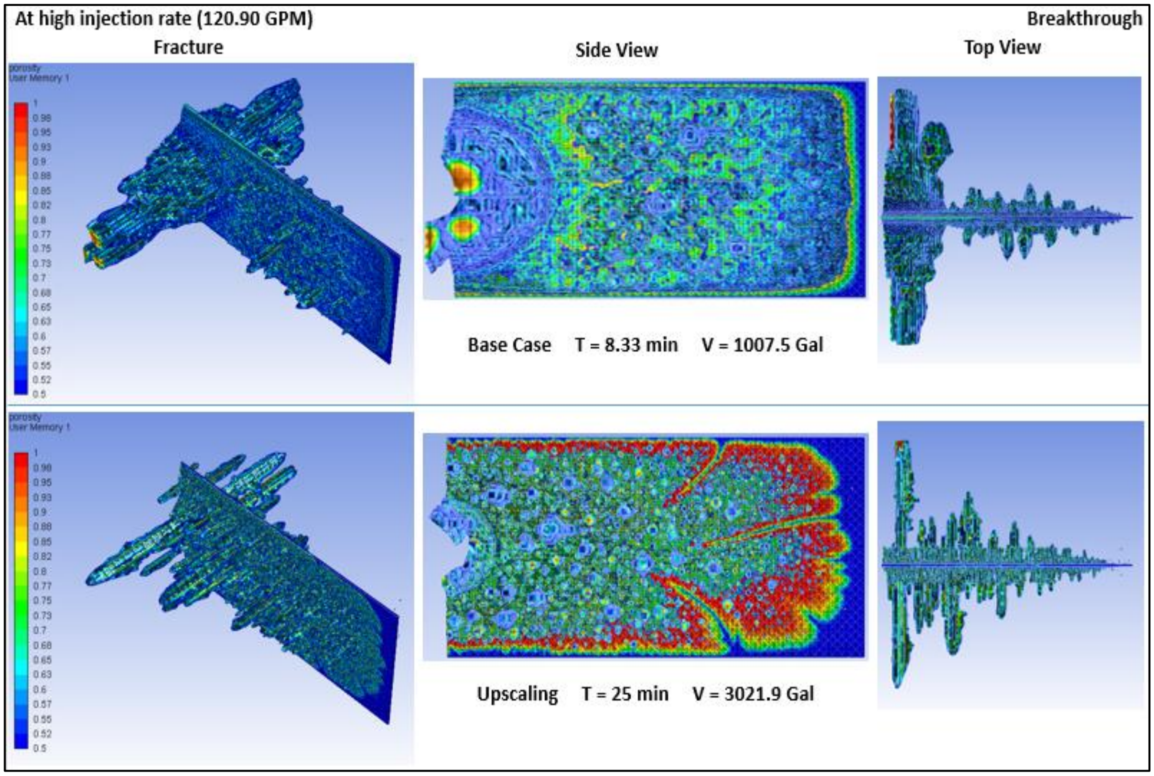

Fig. 5.58 – The state of breakthrough for the upscaled model after injecting 28 wt% HCl at 120.90 GPM injection rate. Reprinted with permission from SPE-191440-18IHFT-MS.

Fig. 5.59 shows the total inject acid volumes to breakthrough in the upscaled model and the base model. Even though the upscaling factor for the model is 10, the acid volumes required to breakthrough for low, intermediate and high injection rates are amplified by factors of 4.35, 4.65 and 3 respectively. This sheds light on the significance of model upscaling on the acid wormholing phenomenon in CFA, and a general trend can be concluded from the demonstrated results. For example, if the base model is upscaled by factor 100, the model dimensions will be 20 meters length, 20 meters width and 10 meter height which will represent an actual field case. In that case, if the intermediate acid injection rate has been used, the anticipated volume will be up-scaled by a factor of 21.62 according to the model. As a result, the volume required to breakthrough and to reach a distance of 10 meters from the acid-fracture in that case is 10071.76 gal which is equal to 239.8 bbls. So in the case of multistage acid fracturing and the desired volume of injected acid during CFA is around 240 bbls, the spacing of acid fracturing stages should be higher than 10 meters (32.8 ft) to avoid the connection of these stages and the interference of their drainage area which will reduce the overall performance of the multistage acid fracturing completion. As a conclusion, model upscaling provides a qualitative relationship of acid injection rates and the total volumes of acid required to reach a specific distance from the fracture during CFA operation. This qualitative relationship contributes significantly in designing an optimum multistage acid fracturing treatment in determining the optimum spacing between the stages of acid fracturing and maximize the productivity of this treatment. Multiple factors need to be considered in this design such as the length of the horizontal section in the well and the presence of natural fractures in the target zone.

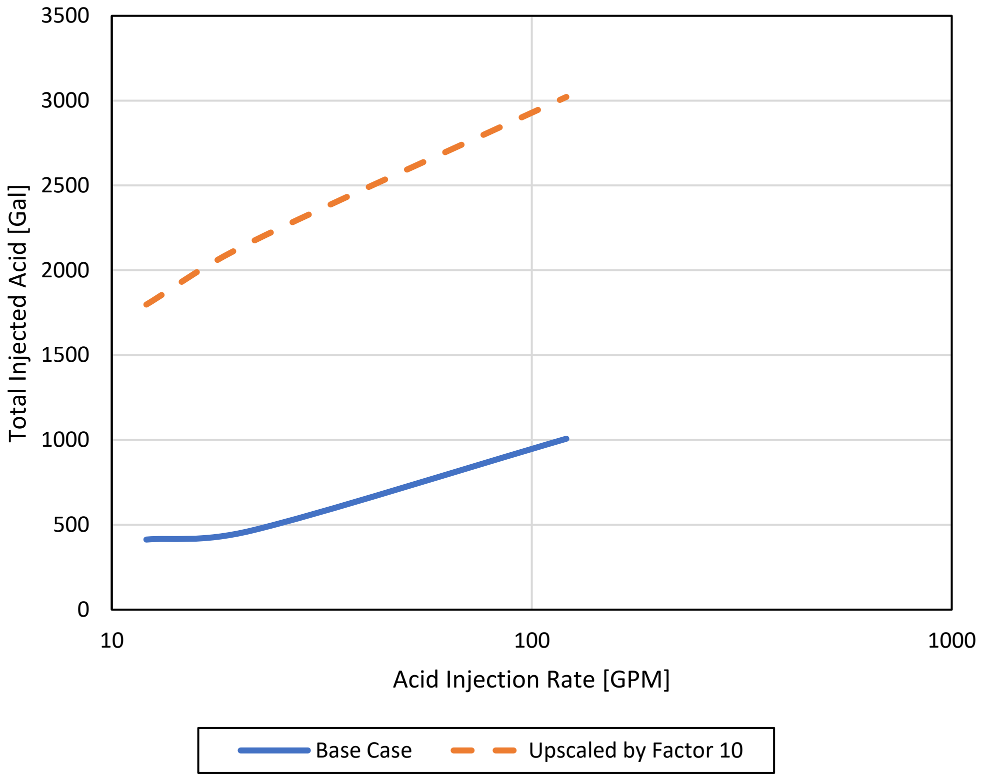

Fig. 5.59 – Total acid volume injected to breakthrough in the up-scaled model for 28 wt% HCl injected at different rates. Reprinted with permission from SPE-191440-18IHFT-MS.

6. CONCLUSIONS AND RECOMMENDATIONS[4]

6.1. Conclusions

A closed-fracture acidizing model was developed in this work using computational fluid dynamics techniques coupled with the two-scale continuum approach with Navier-Stokes formulation that accurately describes the reactive mechanisms of the acid flow in the closed-fracture. Several CFA models were constructed and populated with different porosity distribution profiles of both calcite and dolomite formation to depict the actual porosity distribution and heterogeneity that exists in the target zone. The developed model was validated qualitatively with the experimental work done on the API fracture-conductivity apparatus. A detailed sensitivity analysis has been made for several parameters that affect the performance of CFA on acid-fractured wells. Based on the work done on the simulation models, several points can be concluded:

- The developed CFA model has matched qualitatively the results of the experimental work done on the API fracture-conductivity apparatus using the two-scale continuum approach which successfully captured the dissolution process that is associated with fracture surface etching and wormholing phenomenon during the fracture acidizing process.

---

[4] Partially reprinted with permission from “Acid Wormholing in Multistage Acid Fractured Wells Completed in Tight Naturally Fractured Dolomite Formation: Benefits and Impacts on Acid Fracturing Stimulation Design” by K. Aldhayee, M. Ali, and H. Nasr-El-Din, 2019. SPE-191440-18IHFT-MS, Copyright 2019 by Society of Petroleum Engineers.

- A qualitative relationship was developed between the straight HCl and gelled HCl that can predict the average etched width across the fracture surface with the straight HCl yields larger etched fracture width.
- The dissolution process and wormholing phenomenon in CFA that alters the fracture morphology is similar to matrix acidizing dissolution process that occurs in the carbonate cores during coreflooding.
- Calcite formation is more sensitive to acid injection rate and acid concentration used to conduct CFA operation than the dolomite formation in terms of dissolution patterns and wormholing phenomenon occurs to the fracture due to high surface reaction rate of HCl-calcite system compared to the HCl-dolomite system.
- Since calcite formation exhibits the diffusion-controlled reaction regime with the HCl acid, acid leakoff into the formation occurs in a fast manner at the start of acid injection into the closed-fracture. This phenomenon can be observed by the sharp gradient of the acid concentration profile in the fracture.
- Temperature has a significant effect on the CFA performance in calcite formation. High formation temperatures tend to increase acid diffusivity and surface reaction rate of HCl-calcite system, and that promotes an extensive acid leakoff into the formation leading to an inefficient acid stimulation to the closed-fracture. Low formation temperatures reduce the acid diffusivity and surface reaction rate significantly. And thus, acid flows predominantly in the fracture which leads to an efficient stimulation job, and this can be observed by the smooth gradient of the acid concentration profile in the fracture.

- Through the dimensionless analysis of CFA process in calcite formation, it was proved from investigating Damköhler number that the low injection rate might not be the wisest choice to go for in treating calcite formation that exhibits the mass transfer limited reaction regime. This is due to the formation of dominant wormholes which propagate from the fracture that lead to significant acid leakoff into the formation at the start of CFA operation. It can also be concluded from Damköhler number investigation that low temperature has altered the reaction regime of HCl-calcite system from diffusion-controlled regime to reaction-controlled regime that is insensitive to acid injection rate.
- For dolomite formation, higher acid concentration accelerates the dissolution process and provides the same dissolution pattern as low concentrations with lower required acid volumes. The treatment of dolomite formation, in contrast with calcite formation, requires high acid concentrations and high soaking time with the acid because of its slow nature in the reaction with HCl.
- Vertical wells require fewer acid volumes to initiate wormholes and to propagate through formation to reach breakthrough state than the horizontal wells because of the large injection area in vertical wells compared to the horizontal wells.
- For tight formations, it requires fewer acid volumes to breakthrough as the acid contributes to grow the wormholes that were already initiated previously in the formation unlike the case of permeable formation.
- For highly permeable formation, it requires larger acid volumes to reach the state of breakthrough as the acid generates multiple wormholes along the fracture

surface during the flow of acid in the fracture, since it is easier for the acid to propagate through the high-permeable formation which requires larger acid volumes to grow all these wormholes and to reach the boundaries of the model.

- Fracture conductivity has no effect on wormholes initiation in the formation since the initiation process is a function of injection rate, formation permeability and acid reactivity strength with the formation. However, fracture conductivity has significant effect on wormholing density and the distribution of wormholes along the fracture surface. Low fracture conductivities promote acid leakoff into the formation during CFA process.
- The presence of natural fractures in the medium plays a key role in enhancing the overall efficiency of CFA operation if the injected acid in CFA was able to establish flow networks between the acid-fracture and the surrounded natural fractures depending on their orientations and locations.
- Natural fractures orientation has significant effect at low acid injection rates which control the flow and propagation of acid into the formation. However, The effect of natural fractures orientation ceases as acid injection rate increases.
- Natural fractures minimize the wormholes associated during CFA operation with the transversal ones being the minimum wormholing density.
- Acid leakoff into the formation during CFA operation takes place in the vicinity of injection inlet regardless of the intersected natural fractures with the acid-fracture, since acid leak-off is a function of formation permeability and the reaction parameters between the acid system and formation rock matrix.

- Model upscaling provides a qualitative trend for the developed CFA model to relate the total acid volumes used in the model with the total acid volumes that can be used in actual field scale.
- Interpretation and anticipation of the desired injected volumes in CFA is important and critical in designing the multistage acid fracturing completion and estimating the optimum spacing distance between the acid fracturing stages to ensure that there is no interference or intersection between the drainage areas of these stages which will decrease the overall performance of multistage acid fracture completion.

6.2. Recommendations for Future Work

Limitations of the current work is provided in this section with the emphases that these limitations can be evolved into potential future works that can improve the efficiency of the developed models in this study.

In this study, the developed models are saturated with only one single phase which is water. A single-phase flow in the domain does not represent the actual field application that exhibits multiphase flow phenomenon. The two-scale continuum model can be extended to cover the multiphase flow phenomenon by introducing the parameters related to fluid saturations and capillary pressures. This can be extended to cover the effect of the evolving carbon dioxide that is produced as a result of the reaction between the HCl and carbonate formation when the reservoir pressure declines below 1000 psi.

Straight HCl with no additives was only included in this study. It was proved previously in the literature that the two scale-continuum model is capable in capturing the physics and the chemistry associated with acid dissolution process in the rock matrix. However, the two-scale continuum model is limited to the application of straight acid. A future work can be done to extend the application of the two-scale continuum model to cover the reactive flow mechanisms of different acid systems such as organic acids and viscosified acid by either with polymers or viscoelastic surfactants.

The developed models can be coupled with geomechanical models to include the effect of closure stresses and the stress field surrounding the fractured well. This is very important to accurately apply the fracture conductivity calculations and estimate the fracture conductivity decline with the closure stresses to show the effect of CFA on the overall acid fracturing design.

A steady-state temperature model was imposed in this study to investigate the effect of temperature on the reaction and kinetics of HCl-rock system. For better accuracy, a transient heat transfer model can be coupled with the developed model to cover the cooling effect of the injected acid into the target zone and the heat emerged from the reaction of HCl with the formation that can reach up to 60°F as demonstrated in the literature review section.

REFERENCES

Aldhayee, K., Ali, M. T., and Nasr-El-Din, H. A. 2018. Acid Wormholing in Multistage Acid Fractured Wells Completed in Tight Naturally Fractured Dolomite Formation: Benefits and Impacts on Acid Fracturing Stimulation Design. Presented at the SPE International Hydraulic Fracturing Technology Conference and Exhibition, Muscat, Oman, 16-18 October. SPE-191440-18IHFT-MS. http://dx.doi.org/10.2118/191440-18IHFT-MS.

Abass, H.H., Ortiz, I., Khan, M.R. et al. 2007. Understanding Stress Dependent Permeability of Matrix, Natural Fractures, and Hydraulic Fractures in Carbonate Formations. Presented at the SPE Saudi Arabia Section Technical Symposium, Dhahran, Saudi Arabia, 7-8 May. SPE-110973-MS. http://dx.doi.org/10.2118/110973-MS.

Akanni, O. O. and Nasr-El-Din, H. A. 2015. The Accuracy of Carbonate Matrix-Acidizing Models in Predicting Optimum Injection and Wormhole Propagation Rates. Presented at the SPE Middle East Oil & Gas Show and Conference. Manama, Bahrain, 8–11 March. SPE 172575-MS. http://dx.doi.org/10.2118/172575-MS.

Akanni, O. O., Nasr-El-Din, H. A., and Gusain, D. 2017. A Computational Navier-Stokes Fluid Dynamics Simulation Study of Wormhole Propagation in Carbonate Matrix Acidizing and Analysis of Factors Influencing the Dissolution Process. *SPE J*. **22** (6): 2049-2066. SPE-187962-PA. http://dx.doi.org/10.2118/187962-PA.

Akin, S. and Kovscek, A. 2003. Computed Tomography in Petroleum Engineering Research. Geological Society, London Special Publications **215**:23-38. http://dx.doi.org/10.1144/GSL.SP.2003.215.01.03.

Ali, M. T., and Nasr-El-Din, H. A. 2019. A Robust Model To Simulate Dolomite-Matrix Acidizing. *SPE Prod and Oper*. **34**(1): 109-129. SPE-191136-PA. http://dx.doi.org/10.2118/191136-PA.

Al-Ismail, M. I., Al-Harbi, M. M., Al-Harbi, A. K. et al. 2008. Field Trials of Fiber Assisted Stimulation in Saudi Arabia: An Innovative Non-Damaging Technique for Achieving Effective Zonal Coverage During Acid Fracturing. Presented at the SPE Saudi Arabia section Young Professionals Technical Symposium, Dharan, Saudi Arabia, 29-30 March. SPE-117061-MS. https://dx.doi.org/10.2118/117061-MS.

AlOtaibi, F. M., Al-Dahlan, M. N., Rafie, M. et al. 2017. Successful Completion of the First Ten Multistage Acid Fracturing of an Oil Producer in Saudi Arabia. Presented at the Abu Dhabi International Petroleum Exhibition & Conference, Abu Dhabi, UAE, 13-16 November. SPE-188499-MS. https://dx.doi.org/10.2118/188499-MS.

Anderson, M.S. and Fredrickson, S.E. 1989. Dynamic Etching Tests Aid Fracture-Acidizing Treatment Design. *SPE Prod Eng* **4**(4): 443-449. SPE-16452-PA. http://dx.doi.org/10.2118/16452-PA.

Arbogast, T. and Brunson, D. 2007. A Computational Method for Approximating a Darcy–Stokes System Governing a Vuggy Porous Medium. *Computational Geosciences* **11**(3): 207–218. http://dx.doi.org/10.1007/s10596-007-9043-0.

Bartko, K.M., Conway, M.W., Krawietz, T.E. et al. 1992. Field and Laboratory Experience in Closed Fracture Acidizing the Lisburne Field, Prudhoe Bay, Alaska. Presented at the SPE Annual Technical Conference and Exhibition, Washington, D.C., 4-7 October. SPE-24855-MS. http://dx.doi.org/10.2118/24855-MS.

Beletskaya, A., Ivanov, E., Stukan, M. et al. 2017. Reactive Flow Modeling at Pore Scale. Presented at the Russian Petroleum Technology Conference, Moscow, Russia, 16–18 October. SPE-187805-MS. http://dx.doi.org/10.2118/187805-MS.

Brinkman, H. C. 1949. A Calculation of the Viscous Force Exerted by a Flowing Fluid on a Dense Swarm of Particles. *Applied Scientific Research* **1**(1): 27–34. http://dx.doi.org/10.1007/BF02120313.

Broaddus, G.C., and Fredrickson, S.E. 1975. Fracture Acidizing Method. US Patent No. 3,918,524.

Buijse, M. A. 2000. Understanding Wormholing Mechanisms Can Improve Acid Treatments in Carbonate Formations. *SPE Prod & Oper* **15**(3): 168-175. SPE-38166-MS. http://dx.doi.org/10.2118/38166-MS.

Buijse, M. A. 2000. Understanding Wormholing Mechanisms Can Improve Acid Treatments in Carbonate Formations. *SPE Production & Facilities* **15**(3): 168-175. SPE-65068-PA. https://dx.doi.org/10.2118/65068-PA.

Buijse, M. A. and Glasbergen, G. 2005. A Semi-Empirical Model to Calculate Wormhole Growth in Carbonate Acidizing. Presented at the Annual Technical Conference and Exhibition, Dallas, Texas, 9–10 October. SPE 96892-MS. http://dx.doi.org/10.2118/96892-MS.

Chen, Y., Ma, G., Li, T., et al. 2018. Simulation of Wormhole Propagation in Fractured Carbonate Rocks with Unified Pipe-Network Method. *Computers and Geotechnics* **98**: 58-68. https://dx.doi.org/10.1016/j.compgeo.2017.11.009.

Conway, M. W., Asadi, M., Penny, G. S. et al. 1999. A Comparative Study of Straight/Gelled/Emulsified Hydrochloric Acid Diffusivity Coefficient Using Diaphragm Cell and Rotating Disk. Presented at the SPE Annual Technical

Conference and Exhibition, Houston, Texas, 3-6 October. SPE-56532-MS. http://dx.doi.org/10.2118/56532-MS.

Crowe, C. W., Hutchinson, B. H., and Trittipo, B. L. 1989. Fluid-Loss Control: The Key to Successful Acid Fracturing. *SPE Prod Eng* **4**(2): 215-220. SPE-16883-PA. https://dx.doi.org/10.2118/16883-PA.

Daccord, G., Lenormand, R., and Liétard, O. 1993. Chemical dissolution of a porous medium by a reactive fluid—I. Model for the "wormholing" phenomenon. *Chem Eng Sci* **48** (1): 169-178. http://dx.doi.org/10.1016/0009-2509(93)80293-Y.

De Oliveira, T., De Melo, A., Oliveira, J. et al. 2012. Numerical Simulation of the Acidizing Process and PVBT Extraction Methodology Including Porosity/Permeability and Mineralogy Heterogeneity. Presented at the International Symposium and Exhibition on Formation Damage Control. Lafayette, Louisiana. 15–17 January. SPE 151823-MS. http://dx.doi.org/10.2118/151823-MS.

Deng, J., Mou, J., Hill, A. D. et al. 2011. A New Correlation of Acid Fracture Conductivity Subject to Closure Stress. Presented at the SPE Hydraulic Fracturing Technology Conference, The Woodlands, Texas, 24-26 January. SPE-140402-MS. https://dx.doi.org/10.2118/140402-MS.

Dong, C., Hill, A. D., and Zhu, D. 1999. Acid Etching Patterns in Naturally-Fractured Formations. Presented at the SPE Annual Technical Conference and Exhibition, Houston, Texas, 3-6 October. SPE-56531-MS. http://dx.doi.org/10.2118/56531-MS.

Dong, C., Zhu, D., and Hill, A. D. 2001. Acid Penetration in Natural Fracture Networks. SPE European Formation Damage Conference, The Hague, Netherlands, 21-22 May. SPE-68927-MS. http://dx.doi.org/10.2118/68927-MS.

Economides, M.J., Nolte, K.G., 2000. *Reservoir Stimulation*, 3rd Edition. New York, USA: John Wiley & Sons Ltd.

Fredd, C. N. and Fogler, H. S. 1998. Influence of Transport and Reaction on Wormhole Formation in Porous Media. *AIChE J.* **44**(9): 1933. http://dx.doi.org/10.1002/aic.690440902.

Fredd, C. N. and Fogler, H. S. 1999. Optimum Conditions for Wormhole Formation in Carbonate Porous Media: Influence of Transport and Reaction. *SPE J.* **4**(3): 196-205. SPE-56995-PA. http://dx.doi.org/10.2118/56995-PA.

Fredrickson, S. E. 1986. Stimulating Carbonate Formations Using a Closed Fracture Acidizing Technique. Presented at the SPE East Texas Regional Meeting, Tyler, Texas, 21-22 April. SPE-14654-MS. https://dx.doi.org/10.2118/14654-MS.

Furui, K., Burton, R., Burkhead, D. et al. 2012. A Comprehensive Model of High-Rate Matrix-Acid Stimulation for Long Horizontal Wells in Carbonate Reservoirs: Part I--Scaling Up Core-Level Acid Wormholing to Field Treatments. *SPE J.* **17**(1): 271-279. http://dx.doi.org/10.2118/134265-PA.

Gangi, A. F. 1978. Variation of Whole and Fractured Porous Rock Permeability with Confining Pressure. *International Journal of Rock Mechanics and Mining Sciences & Geomechanics Abstracts* **15**(5): 249-257. https://dx.doi.org/10.1016/0148-9062(78)90957-9.

Garzon, F.O., Solares, J.R., Ramanathan, V. et al. 2008. Long Term Evaluation of an Innovative Acid System for Fracture Stimulation of Carbonate Reservoirs in Saudi Arabia. Presented at the International Petroleum Technology Conference, Kuala Lumpur, Malaysia, 3-5 December. IPTC-12668-MS. http://dx.doi.org/10.2523/IPTC-12668-MS.

Ghommem, M., Qiu, X., Brady, D. et al. 2016. Monitoring of Matrix Acidizing by Using Resistivity Measurements. Presented at the SPE Annual Technical Conference and Exhibition, Dubai, UAE, 26-28 September. SPE-181414-MS. http://dx.doi.org/10.2118/181414-MS.

Ghommem, M., Zhao, W., Dyer, S. et al. 2015. Carbonate acidizing: Modeling, analysis, and characterization of wormhole formation and propagation. *J Pet Sci Eng* **131**: 18-33. http://dx.doi.org/j.petrol.2015.04.021.

Golfier, F., Zarcone, C., Bazin, B. et al. 2002. On the Ability of a Darcy-Scale Method Model to Capture Wormhole Formation During the Dissolution of a Porous Medium. *J. Fluid Mech*. **457**: 213-254. http://dx.doi.org/10.1017/S0022112002007735.

Gong, M., Lacote, S., and Hill, A. D. 1999. New Model of Acid-Fracture Conductivity Based on Deformation of Surface Asperities. *SPE J.* **4**(3): 206-214. SPE-57017-PA. https://dx.doi.org/10.2118/57017-PA.

Gong, M., Lacote, S., and Hill, A. D. 1999. New Model of Acid-Fracture Conductivity Based on Deformation of Surface Asperities. *SPE J.* **4**(3): 206-214. SPE-57017-PA. https://dx.doi.org/10.2118/57017-PA.

Guillot, G., De Antuñano, Y., Cuadras, R. et al. 2016. Selectively Stimulating Oil Production in Mature Naturally Fractured Carbonate Reservoirs. Presented at the SPE International Conference and Exhibition on Formation Damage Control, Lafayette, Louisiana, 24-26 February. SPE-178937-MS. https://dx.doi.org/10.2118/178937-MS.

Hill, A. D., Zhu, D., and Wang, Y. 1995. The Effect of Wormholing on the Fluid Loss Coefficient in Acid Fracturing. SPE Production & Facilities 10 (4): 257-263. SPE-27403-PA. https://dx.doi.org/10.2118/27403-PA.

Hoefner, M. L. and Fogler, H. S. 1988. Pore Evolution and Channel Formation During Flow and Reaction in Porous Media. *AIChE J.* **34**(1): 45-54. http://dx.doi.org/10.1002/aic.690340107.

Hoefner, M. L. and Fogler, H. S. 1989. Fluid-Velocity and Reaction-Rate Effects During Carbonate Acidizing: Application of Network Model. *SPE Prod Eng* **4**(1): 56-65. SPE-15573-PA. https://dx.doi.org/10.2118/15573-PA.

Houchin, L. R., Dunlap, D. D., Hudson, L. M. et al. 1986. Evaluation of Oil-Soluble Resin as an Acid-Diverting Agent. Presented at the SPE Annual Technical Conference and Exhibition, New Orleans, Louisiana, 5-8 October. SPE-15574-MS. https://dx.doi.org/10.2118/15574-MS.

Huang, T., Hill, D., and Schechter, S. 1997. Reaction Rate and Fluid Loss: The Keys to Wormhole Initiation and Propagation in Carbonate Acidizing. Presented at the International Symposium on Oilfield Chemistry, Houston, Texas, 18 – 21 February. SPE 37312-MS. http://dx.doi.org/10.1016/10.2118/37312-MS.

Hung, K. M., Hill, A. D., and Sepehrnoori, K. 1989. A Mechanistic Model of Wormhole Growth in Carbonate Matrix Acidizing and Acid Fracturing. *J Pet Technol* **41**(1): 59-66. SPE-16886-PA. http://dx.doi.org/2118/16886-PA.

Inda, A., Steffani, O., Soriano, E. et al. 2009. Field Development and Productivity Improvement in Offshore Mexico - Engineering and Laboratory Synergistic Approach to Carbonate Fracture Acidizing. Presented at the 8th European Formation Damage Conference, Scheveningen, The Netherlands, 27-29 May. SPE-121928-MS. http://dx.doi.org/10.2118/121928-MS.

Itoua, R., Martocchia, F., Farina, L. et al. 2015. Multistage Acid Fracturing on Carbonate Reservoir: Successful Experience From Offshore Congo. Presented at Offshore Mediterranean Conference and Exhibition, Ravenna, Italy, 25-27 March. OMC-2015-325.

Izgec, O., Zhu, D., and Hill, A. D. 2010. Numerical and Experimental Investigation of Acid Wormholing during Acidization of Vuggy Carbonate Rocks. *J Pet Sci Eng* **74**(1): 51-66. http://dx.doi.org/10.1016/j.petrol.2010.08.006.

Jahediesfanjani, H., and Civan, F. 2006. Improving Performance of the Naturally Fractured Carbonate Reservoirs by Means of the Various Stimulation and Completion Techniques. Presented at the SPE International Oil Conference and Exhibition, Cancun, Mexico, 31 August-2 September. SPE-103986-MS. http://dx.doi.org/10.2118/103986-MS.

Jauregui, J. A., Malik, A. R., Nunez Garcia, W. et al. 2011. Successful Application of Novel Fiber Laden Self-Diverting Acid System during Fracturing Operations of

Naturally Fractured Carbonates in Saudi Arabia. Presented at the SPE Middle East Oil and Gas Show and Conference, Manama, Bahrain, 25-28 September. SPE-142512-MS. https://dx.doi.org/10.2118/142512-MS.

Kalfayan, L. 2008. *Production Enhancement with Acid Stimulation*, 2nd Edition. Tulsa, Oklahoma: PennWell Corporation.

Kalia, N. and Balakotaiah, V. 2007. Modeling and Analysis of Wormhole Formation in Reactive Dissolution of Carbonate Rocks. *Chem Eng Sci* **62**(4): 919-928. http://dx.doi.org/10.1016/j.ces.2006.10.021.

Kalia, N. and Balakotaiah, V. 2009. Effect of Medium Heterogeneities on Reactive Dissolution of Carbonates. *Chem Eng Sci* **64**(2): 376-390. http://dx.doi.org/10.1016/j.ces.2008.10.026.

Knox, J.A., and Fredrickson, S.E. 1973. Method of Fracture Acidizing a Well Formation. US Patent No. 3,768,564.

Knox, J.A., and Fredrickson, S.E. 1974. Method of Fracture Acidizing a Well Formation. US Patent No. 3,842,911.

Liu, M., Zhang, S., and Mou, J. 2012. Effect of Normally Distributed Porosities on Dissolution Pattern in Carbonate Acidizing. *J Pet Sci Eng* **94–95** (0): 28-39. http://dx.doi.org/10.1016/j.petrol.2012.06.021.

Liu, P., Xue, H., Zhao, L., et al. 2016. Simulation of 3D multi-scale wormhole propagation in carbonates considering correlation spatial distribution of petrophysical properties. *J Natural Gas Sci Eng* **32**: 81-94. https://dx.doi.org/10.1016/j.jngse.

Liu, X., Ormond, A., Bartko, K. et al. 1997. A Geochemical Reaction-Transport Simulator for Matrix Acidizing Analysis and Design. *J Pet Sci Eng* **17**(1–2): 181-196. http://dx.doi.org/10.1016/S0920-4105(96)00064-2.

Lo, K. K., and Dean, R. H. 1989. Modeling of Acid Fracturing. *SPE Prod Eng* **4**(2): 194-200. SPE-17110-PA. https://dx.doi.org/10.2118/17110-PA.

Ma, G., Chen, Y., Jin, Y., et al. 2018. Modelling Temperature-Influenced Acidizing Process in Fractured Carbonate Rocks. *International Journal of Rock Mechanics and Mining Sciences* **105**: 73-84. https://dx.doi.org/10.1016/j.ijrmms.2018.03.019.

Maheshwari, P. and Balakotaiah, V. 2013. Comparison of Carbonate HCl Acidizing Experiments with 3D Simulations. *SPE Prod & Oper* **28**(4): 402-413. SPE-164517-PA http://dx.doi.org/10.2118/164517-PA.

Maheshwari, P., Gharbi, O., Thirion, A. et al. 2016. Development of a Reactive Transport Simulator for Carbonates Acid Stimulation. Presented at the SPE Annual Technical Conference and Exhibition, Dubai, UAE, 26-28 September. SPE-181603-MS. http://dx.doi.org/10.2118/181603-MS.

Maheshwari, P., Ratnakar, R. R., Kalia, N. et al. 2012. 3-D Simulation and Analysis of Reactive Dissolution and Wormhole Formation in Carbonate Rocks. *Chem Eng Sci* **90**(0): 258-274. http://dx.doi.org/10.1016/j.ces.2012.12.032.

Mahrous, M., Sultan, A. and Sonnenthal, E. 2017. Towards Geochemically Accurate Modeling of Carbonate Acidizing with HCl Acid. Presented at the Annual Technical Conference and Exhibition, San Antonio, Texas, 9–11 October. SPE-187183-MS. http://dx.doi.org/10.2118/187183-MS.

McDuff, D., Claiborne, E., Zielinski, M. et al. 2016. An Engineered Approach to Acid Stimulation Strategies for Wells in the Kurdistan Region of Iraq. Presented at the Abu Dhabi International Petroleum Exhibition & Conference, Abu Dhabi, UAE, 7-10 November. SPE-182888-MS. https://dx.doi.org/10.2118/182888-MS.

Mofti, M., Al-Othman, M., Alboueshi, A. et al. 2018. First Fully Successful Application of a Multistage Acid Fracturing Operation to Stimulate a Carbonate Formation, Resulting in the Implementation in Other Wells in the Mature Bahrah Field, North Kuwait. Presented at the SPE/IADC Middle East Drilling Technology Conference and Exhibition, Abu Dhabi, UAE, 29-31 January. SPE-189353-MS. https://dx.doi.org/10.2118/189353-MS.

Mou, J., Yu, X., Wang, L. et al. 2019. Effect of Natural Fractures on Wormhole-Propagation Behavior. *SPE Prod and Oper*. **34**(1): 145-158. SPE-191148-PA. https://dx.doi.org/10.2118/191148-PA.

Mou, J., Zhang, S., 2015. Modeling acid leakoff during multistage alternate injection of pad and acid in acid fracturing. *J Natural Gas Sci Eng* **26**: 1161-1173. https://dx.doi.org/10.1016/j.jngse.2015.08.007.

Mou, J., Zhu, D., and Hill, A. D. 2010. A New Acid-Fracture Conductivity Model Based on the Spatial Distributions of Formation Properties. Presented at the SPE International Symposium and Exhibition on Formation Damage Control, Lafayette, Louisiana, 10-12 February. SPE-127935-MS. https://dx.doi.org/10.2118/127935-MS.

Nasr-El-Din, H. A., Driweesh, S. M., and Muntasheri, G. A. 2003. Field Application of HCl-Formic Acid System to Acid Fracture Deep Gas Wells Completed with Super Cr-13 Tubing in Saudi Arabia. Presented at the SPE International Improved Oil Recovery Conference in Asia Pacific, Kuala Lumpur, Malaysia, 20-21 October. SPE-84925-MS. http://dx.doi.org/10.2118/84925-MS.

Nasr-El-Din, H. A., Solares, J. R., Al-Zahrani, A. A. et al. 2009. Acid Fracturing of Gas Wells Using Solid Acid: Lessons Learned From First Field Application. *SPE Prod & Oper* **24** (2): 320-335. SPE-110895-PA. http://dx.doi.org/10.2118/110895-PA.

Nierode, D. E., and Kruk, K. F. 1973. An Evaluation of Acid Fluid Loss Additives Retarded Acids, and Acidized Fracture Conductivity. Presented at the Fall Meeting of the Society of Petroleum Engineers of AIME, Las Vegas, Nevada, 30 September – 3 October. SPE-4549-MS. SPE-17110-PA. https://dx.doi.org/10.2118/4549-MS.

Nierode, D. E., and Kruk, K. F. 1973. An Evaluation of Acid Fluid Loss Additives Retarded Acids, and Acidized Fracture Conductivity. Presented at the Fall Meeting of the Society of Petroleum Engineers of AIME, Las Vegas, Nevada, 30 September–3 October. SPE-4549-MS. https://dx.doi.org/10.2118/4549-MS.

Nieto, C. M., Pournik, M., and Hill, A. D. 2008. The Texture of Acidized Fracture Surfaces: Implications for Acid Fracture Conductivity. *SPE Prod and Oper*. **23**(3): 343-352. SPE-102167-PA. http://dx.doi.org/10.2118/102167-PA.

Nnanna, E. J., and Ajienka, J. A. 2005. Critical Success Factors for Well Stimulation. Presented at the SPE Nigeria Annual International Conference and Exhibition, Abuja, Nigeria, 1-3 August. SPE-98823-MS. http://dx.doi.org/10.2118/98823-MS.

Oeth, C., Hill, A. D., Zhu, D. et al. 2011. Characterization of Small Scale Heterogeneity to Predict Acid Fracture Performance. Presented at the SPE Hydraulic Fracturing Technology Conference, The Woodlands, Texas, 24-26 January. SPE-140336-MS. https://dx.doi.org/10.2118/140336-MS.

Panga, M. K. R., Balakotaiah, V., and Ziauddin, M. 2002. Modeling, Simulation and Comparison of Models for Wormhole Formation during Matrix Stimulation of Carbonates. Presented at the SPE Annual Technical Conference and Exhibition. San Antonio, Texas. 29 September – 2 October. SPE 77369-MS http://dx.doi.org/10.2118/77369-MS.

Panga, M. K. R., Ziauddin, M., and Balakotaiah, V. 2005. Two-Scale Continuum Model for Simulation of Wormholes in Carbonate Acidization. *AIChE J.* **51**(12): 3231-3248. http://dx.doi.org/10.1002/aic.10574.

Perex, D., Huidobro, E., and Avendano, J. 1998. Applications of Acid Fracturing Technique to improve Gas Production in Naturally Fractured Carbonate Formations, Veracruz Field, Mexico. Presented at the IADC/SPE Asia Pacific Drilling Technology, Jakarta, Indonesia, 7-9 September. SPE-47820-MS. https://dx.doi.org/10.2118/47820-MS.

Popov, P., Qin, G., Bi, L. et al. 2007. Multiscale Methods for Modeling Fluid Flow through Naturally Fractured Carbonate Karst Reservoirs. Presented at the SPE Annual

Technical Conference and Exhibition, Anaheim, California, 11-14 November. SPE-110778-MS. http://dx.doi.org/10.2118/110778-MS.

Pournik, M., Li, L., Smith, B. T. et al. 2013. Effect of Acid Spending on Etching and Acid-Fracture Conductivity. *SPE Prod and Oper*. **28**(1): 46-54. SPE-136217-PA. http://dx.doi.org/10.2118/136217-PA.

Pournik, M., Nasr-El-Din, H.A., and Mahmoud, M.A. 2011. A Novel Application of Closed-Fracture Acidizing. *SPE Prod & Oper* **26**(1): 18-29. SPE-124874-PA. http://dx.doi.org/10.2118/124874-PA.

Pournik, M., Zhu, D., and Hill, A. D. 2009. Acid-Fracture Conductivity Correlation Development Based on Acid-Etched Fracture Characterization. Presented at the European Formation Damage Conference, Scheveningen, Netherlands, 27-29 May. SPE-122333-MS. https://dx.doi.org/10.2118/122333-MS.

Sarma, D. K., Pal, T., Kumar, D. et al. 2017. Application of Closed Fracture Acidizing for Stimulation of Tight Carbonate Reservoir in Mumbai Offshore. Presented at the SPE Oil and Gas India Conference and Exhibition, Mumbai, India, 4–6 April. SPE-185344-MS. https://dx.doi.org/10.2118/185344-MS.

Schwalbert, P., Zhu, D., and Hill, A. D. 2017. Extension of an Empirical Wormhole Model for Carbonate Matrix Acidizing Through Two-Scale Continuum 3D Simulations. Presented at the SPE Europec featured at 79th EAGE Conference and Exhibition, Paris, France, 12-15 June. SPE-185788-MS. http://dx.doi.org/10.2118/185788-MS.

Settari, A. 1993. Modeling of Acid-Fracturing Treatments. *SPE Production & Facilities* **8** (1): 30-38. SPE-21870-PA. https://dx.doi.org/10.2118/21870-PA.

Sizer, J.P., Moullem, A.S., and Abou-Sayed, I.S. 1991. Evaluation of Closed Fracture Acidizing Performed in a Tight Limestone Formation. Presented at the Middle East Oil Show, Bahrain, 16-19 November. SPE-21440-MS. http://dx.doi.org/10.2118/21440-MS.

Sollman, M. Y., Hunt, J. L., and Daneshi, T. 1990. Well-Test Analysis Following a Closed-Fracture Acidizing Treatment. *SPE Formation Evaluation* **5**(4): 369-374. SPE-17972-PA. https://dx.doi.org/10.2118/17972-PA.

Tansey, J. 2014. Pore-Network Modeling of Carbonate Acidization. Presented at the SPE Annual Technical Conference and Exhibition, Amsterdam, The Netherlands, 27-29 October. SPE-173472-STU. http://dx.doi.org/10.2118/173472-STU.

Ueda, K., Zhang, W., Zhu, D. et al. 2016. Evaluation of Acid Fracturing by Integrated Pressure Analysis and 3D Simulation: A Field Application for Multi-Stage Stimulation in Horizontal Wells. Presented at the SPE Hydraulic Fracturing

Technology Conference, The Woodlands, Texas, 9-11 February. SPE-179123-MS. https://dx.doi.org/10.2118/179123-MS.

Ugursal, A., Zhu, D., and Hill, A. D. 2018. Development of Acid Fracturing Model for Naturally Fractured Reservoirs. Presented at the SPE Hydraulic Fracturing Technology Conference and Exhibition, The Woodlands, Texas, 23-25 January. SPE-189834-MS. https://dx.doi.org/10.2118/189834-MS.

Valko, P. P., and Economides, M. J. 1998. Heavy Crude Production from Shallow Formations: Long Horizontal Wells Versus Horizontal Fractures. Presented at the SPE International Conference on Horizontal Well Technology, Calgary, Alberta, 1-4 November. SPE-50421-MS. https://dx.doi.org/10.2118/50421-MS.

Walsh, J.B. 1981. Effect of Pore Pressure and Confining Pressure on Fracture Permeability. *International Journal of Rock Mechanics and Mining Sciences & Geomechanics Abstracts* **18**(5): 429-435. https://dx.doi.org/10.1016/0148-9062(81)90006-1.

Wang, X., Zou, H., Zheng, X. et al. 2003. Optimization of Acid Fracturing to Improve Heavy Oil Production in Naturally Fractured Carbonates. Presented at the SPE Production and Operations Symposium, Oklahoma, 23-26 March. SPE-80897-MS. http://dx.doi.org/10.2118/80897-MS.

Wang, X., Zou, H., Zheng, X. et al. 2003. Optimization of Acid Fracturing to Improve Heavy Oil Production in Naturally Fractured Carbonates. Presented at the SPE Production and Operations Symposium, Oklahoma City, Oklahoma, 23-26 March. SPE-80897-MS. https://dx.doi.org/10.2118/80897-MS.

Wang, Y., Hill, D., and Schechter, S. 1993. The Optimum Injection Rate for Matrix Acidizing of Carbonate Formations. Presented at the SPE Annual Technical Conference and Exhibition, Houston, Texas, 3–6 October. SPE 26578-MS. http://dx.doi.org/10.2118/26578-MS.

Wheeler, J. A. 1969. Analytical Calculations for Heat Transfer from Fractures. Presented at the Improved Oil Recovery Symposium, Tulsa, Oklahoma, 13-15 April. SPE-2494-MS. https://dx.doi.org/10.2118/2494-MS.

Whitsitt, N. F. and Dysart, G. R. 1970. The Effect of Temperature On Stimulation Design. *SPE JPT* **22**(4): 493-502. SPE-2497-PA. http://dx.doi.org/10.2118/2497-PA.

Williams, B. B. and Nierode, D. E. 1972. Design of Acid Fracturing Treatments. *SPE JPT* **24**(7): 849-859. SPE-3720-PA. https://dx.doi.org/10.2118/3720-PA.

Wu, Y., Salama, A., and Sun, S. 2015. Parallel simulation of wormhole propagation with the Darcy–Brinkman–Forchheimer framework. *Computers and Geotechnics* **69**: 564-577. https://doi.org/10.1016/j.compgeo.

Xu, Y., Zou, H., Lei, Q. et al. 2007. Optimized Deep-Penetration Acid Fracturing Technology in Low-Permeability, Naturally Fractured, Complex Lithology Reservoirs. Presented at the SPE Production and Operations Symposium, Oklahoma City, Oklahoma, 31 March – 3 April. SPE-106710-MS. https://dx.doi.org/10.2118/106710-MS.

Yao, J., Huang, Z., Li, Y., et al. 2010. Discrete Fracture-Vug Network Model for Modeling Fluid Flow in Fractured Vuggy Porous Media. Presented at the International Oil and Gas Conference and Exhibition, Beijing, China, 8-10 June. SPE-130287-MS. http://dx.doi.org/10.2118/130287-MS.

Zhang, Y., Yang, S., Zhang, S. et al. 2014. Wormhole Propagation Behavior and Its Effect on Acid Leakoff under In Situ Conditions in Acid Fracturing. *Transp Porous Med* **101** (1): 99-114. https://dx.doi.org/10.1007/s11242-013-0233-z.

Zhu, D., Oeth, C. V., and Hill, A. D. 2013. Acid Fracturing: Fully 3D Simulation and Performance Prediction. Presented at the SPE Hydraulic Fracturing Technology Conference, The Woodlands, Texas, 4-6 February. SPE-163840-MS. https://dx.doi.org/10.2118/163840-MS.